Forschungszentrum Karlsruhe
Technik und Umwelt
Wissenschaftliche Berichte
FZKA 6357

Closure Models for the Computation of Dilute Bubbly Flows

Sorin M. Mitran
Institut für Reaktorsicherheit
Projekt Nukleare Sicherheitsforschung

Forschungszentrum Karlsruhe GmbH, Karlsruhe
2000

Abstract

In the large scale computation of turbulent bubbly flow limited computer resources imply that not all phase interfaces and adjoining boundary layers may be resolved. The problem of devising appropriate closure models thus arises. Two closure problems are considered in this report. The computational procedure is assumed to be based upon the center of mass conservation equations. The first closure problem considered is the discrepancy between the center of mass momentum flux and the true momentum flux in a grid cell. This discrepancy is expressed by a momentum drift flux (MDF) term. Two models allowing computation of the MDF term are presented. The first model uses a viscid-inviscid interaction analysis of the flow around a single bubble and is suitable for laminar flow. The second model modifies the Helmholtz decomposition of the turbulent velocity field into a scalar and a vector potential. The Poisson equations giving the two potentials are solved with modified right hand side terms. The modifications reflect the influence of the unresolved boundary conditions on the bubble interfaces. The second closure problem considered is the derivation of a subgrid scale stress (SGS) model for unresolved turbulent motion. The unresolved bubbles are represented through their hydrodynamic potential. Kinetic theory is applied to derive an additional viscosity due to the unresolved bubbles. This effect is used in a renormalization group analysis to derive an SGS model. The report closes with some considerations on minimal surface energy interface reconstruction.

This report was prepared while the author was in residence at the Institut für Reaktorsicherheit, Forschungszentrum Karlsruhe as Gastwissenschaftler, 1 October, 1998 to 31 July, 1999.

Zusammenfassung

Schließungsmodelle für die numerische Berechnung von Blasenströmungen mit geringem Gasanteil

Der hohe numerische Aufwand und die begrenzte Leistung heutiger Computer erlauben es bei großskaligen numerischen Berechnungen von turbulenten Blasenströmungen nicht, die Phasengrenzflächen und die entsprechenden Grenzschichten detailliert aufzulösen. Damit ergibt sich das Problem, geeignete Schließungsmodelle zu entwickeln. In diesem Bericht werden zwei Schließungsprobleme betrachtet. Dabei wird davon ausgegangen, daß das Berechnungsverfahren auf den Erhaltungsgleichungen für die Massenschwerpunktgrößen der Zweiphasenströmung basiert. Das erste Schließungsproblem behandelt die Abweichung zwischen dem Impulsfluß des Massenschwerpunkts und dem wahren Impulsfluß in einer Gitterzelle. Diese Abweichung wird ausgedrückt durch einen Drift-Impulsfluß. Es werden zwei Modelle zur Berechnung des Drift-Impulsflusses vorgestellt. Das erste Modell verwendet eine Kombination aus reibungsfreier und reibungsbehafteter Analyse der Umströmung einer Einzelblase und ist für laminare Strömung geeignet. Das zweite Modell basiert auf der Helmholtz-Zerlegung des turbulenten Geschwindigkeitsfeldes in ein skalares Potential und ein Vektorpotential. Zur Bestimmung der beiden Potentiale werden Poisson-Gleichungen mit modifizierter rechter Seite gelöst. Die Modifikationen spiegeln dabei den Einfluß der nicht aufgelösten Grenzschichtbedingungen an der Phasengrenze der Blase wider. Das zweite Schließungsproblem behandelt die Entwicklung eines Feinstrukturmodells für räumlich nicht aufgelöste turbulente Fluktuationen. Die nicht aufgelösten Blasen werden über ihr hydrodynamisches Potential dargestellt. Mit Hilfe der kinetischen Theorie wird für die nicht aufgelösten Blasen eine zusätzliche Viskosität abgeleitet. Darauf aufbauend wird mit einer Renormalisierungsgruppen-Analyse ein Feinstrukturmodell entwickelt. Der Bericht schließt mit Überlegungen zur Rekonstruktion von Phasengrenzflächen basierend auf dem Prinzip der Minimierung der Oberflächenenergie.

Contents

Preface v

I Unresolved Boundary Layer Closures 1

1 Problem formulation 3

2 A Boundary Element Method for Axisymmetric Bubbles 7
- 2.1 Potential flow around a non-buoyant axisymmetric bubble 7
  - 2.1.1 Differential equation formulation 7
  - 2.1.2 Integral equation formulation 9
  - 2.1.3 Numerical solution of the integral equation 9
  - 2.1.4 Procedure for determining the bubble shape 14
  - 2.1.5 Geometric characteristics of the bubble 14
  - 2.1.6 Evaluation of the velocity field around a bubble of known shape 16
- 2.2 Buoyancy effects 26
- 2.3 Inviscid, axisymmetric momentum drift-flux term 31
- 2.4 Viscous Effects 33
  - 2.4.1 Effect upon bubble shape 33
  - 2.4.2 Effect upon velocity distribution 34

3 The Dynamic Momentum Drift-Flux Model 38
- 3.1 An overview 38
  - 3.1.1 Decomposition of the velocity field 38
  - 3.1.2 Modified representation due to interface effects 39
  - 3.1.3 Subgrid-scale effects given by the DMDF model 41
  - 3.1.4 Finite difference approximation of derivatives functions with discontinuities 42
- 3.2 The 2D Case 43
  - 3.2.1 The stream function problems 44
  - 3.2.2 The scalar potential problems 49
  - 3.2.3 Algorithm schematic and computational effort 51
- 3.3 The 3D Case 52
  - 3.3.1 The vorticity correction 54
  - 3.3.2 The normal velocity correction 55

3.4 Typical computational result 55
3.5 Conclusions 55

II Turbulent Subgrid Stress Closures 57

4 Problem formulation and overview of research 59

5 Statistical Thermodynamics of Ideal Bubbly Flow 62
5.1 Motivation 62
5.2 Bulk behavior estimates from pairwise interaction potential 63
    5.2.1 Some results from kinetic theory 63
5.3 Some results from statistical thermodynamics of gases 65
5.4 Analogous quantities for dilute bubbly flow 66
5.5 Predictions from the analogy 67
    5.5.1 Estimates of the additional viscosity 68
    5.5.2 Phase transition prediction 69
5.6 Current experimental evidence and suggestions for further verifications 70

6 Turbulence models for bubbly flow 72
6.1 General principles of the renormalization group 72
6.2 Derivation of an eddy-viscosity model for single phase flow by RNG 74
6.3 Derivation of an eddy-viscosity model for bubbly flow by RNG 78
    6.3.1 Using an assumed turbulent kinetic energy spectrum 78
    6.3.2 Using a bubbly mixture viscosity 79

7 Direct Numerical Simulation of a Model of Turbulent Bubbly Flow 82
7.1 A model turbulent bubbly flow problem 82
7.2 Overview of numerical techniques applied in OCTLES 84
    7.2.1 Multidimensional discretization procedures 84
    7.2.2 Residual distribution schemes 85
7.3 Initial results 88

III Local Thermodynamic Analysis of Phase Interface Formation 91

8 Considerations on interface reconstruction procedures 93
8.1 The MFEIR Algorithm 93
8.2 Comparisons with other Interface Reconstruction Algorithms 95

IV Conclusions **97**

Appendix **101**

A Partition over Cartesian grid algorithms **101**
A.1 The two-dimensional case 101
  A.1.1 Example: partition of an ellipse 105
A.2 The three-dimensional case 107
A.3 Extensions to arbitrary bodies 107

B The AxiBubble program **110**
B.1 Main program components 110
B.2 Program input, output, flowchart 111
  B.2.1 `Tetra.dat` 111
  B.2.2 `SurfTri.dat` 112
  B.2.3 `grid.dat` 112
  B.2.4 `gridvel.dat` 112
  B.2.5 `mdfterm.dat` 113
  B.2.6 Flowchart 113
B.3 Program installation 114
B.4 Ellipsoid of revolution test case 114

C Essential features of OCTLES data structures and procedures **115**
C.1 Ancestor, parent and child volumes 115
C.2 Framework for actions upon the program data 117

Bibliography **120**

Preface

This report is concerned with the theoretical analysis and numerical simulation of bubbly flow. The paradigm situation considered is that of air bubbles in water. The main focus of the report is on the dilute regime, when the volume fraction of air is small. The main objective of this investigation is to determine appropriate closures for the large-scale computation of bubbly flow. Typical procedures proposed for such computation include the level-set method or the volume-of-fluid method (VOF). The practical objective for these computations is to provide accurate assessments of heat, mass and momentum transfer in geometries representative of industrial applications such as reactor cooling. Given the large physical domain of interest in the final application, it is unlikely that a full resolution of all phase inclusions is within the capacity of current, or future, computational facilities. Moreover, it is apparent that such detailed information is not of prime engineering interest. In the analysis of the technical flow systems to be computed it is useful to consider three scales:

1. a large-scale given by the overall dimensions of the flow domain;
2. a meso-scale given by the largest observed flow structures;
3. a micro-scale given roughly by the onset of dominant viscous behavior.

Experimental observations suggest that meso-scale structures involving significant void fractions do occur in geometries similar to that of the intended final applications. Bubble columns are an example in point, in which random, large groups of bubbles, or a single large bubble formed by coalescence, are seen to arise from time to time. Such large scale structures render inoperative standard statistical treatments of physical systems with a large number of degrees of freedom, methods which have been used with efficacy in the description of the physics of gases or spin systems among other applications. The physics of the flow system of interest in bubbly flow is seen to have both a fine-scale random behavior and a medium scale partially cooperative behavior between the various bubble sizes. Purely theoretical analysis is of limited use in the description of such a system.

In the absence of a general theoretical framework in which to treat such a system, and given the great experimental difficulties in extracting detailed flow information, numerical simulation on the flow mesoscale is perceived as a useful tool to further knowledge of such flows. Akin to the large-eddy simulation (LES) method one may envisage a procedure in which the large-scale bubbles that arise from cooperative behavior of void inclusions, and which dominate the flow behavior at the mesoscale, are directly simulated by a numerical procedure. At the micro-scale there would still remain unresolved bubbles. The influence of these bubbles upon the large-scale flow is one of the closures needed for a complete numerical description of the flow. If it is admitted that small scale bubbles are not to be resolved by brute computational force, it is also the case that flow structures within any one of the phases are also unresolved. In particular, the boundary layers formed in the vicinity of meso-scale bubbles are also unlikely to be resolved. An appropriate closure is needed for this effect also. Finally, the bubbly flows of interest in applications are almost invariantly turbulent. A direct numerical simulation of turbulence in flows of industrial interest remains a far goal. A closure is needed therefore to account for the transfer of momentum and energy from the resolved meso-scales to the micro-scales, i.e. a subgrid scale (SGS) stress model. The problem of constructing a SGS model is compounded by the need to take into account small scale bubbles. The effect of the bubbles upon turbulent energy transfer has been shown to be significant by experimental investigations.

In summary, the computation by a VOF method of a complex bubbly flow of industrial interest is seen to require at least the following closures:

1. influence of unresolved boundary layers within a single phase upon the overall flow;

2. a subgrid turbulence model which takes into account the presence of unresolved bubbles;

3. hydrodynamic coupling between resolved and unresolved bubbles.

This however does not conclude the enumeration of difficulties inherent in a computational approach. A fundamental aspect which must be addressed is the attainment of thermodynamic behavior of the computed system. Essentially, when applying the mass, momentum and energy transport equations to a bubbly flow, we are using reversible mechanics in order to simulate a system for which large-scale, irreversible thermodynamic behavior is readily observed. The situation most akin to the proposed application of a VOF (or similar procedure) to bubbly flow is that of molecular dynamics computations. There also, a large number of degrees of freedom are computed and for given micro-scale interactions (e.g. the Lennard-Jones potential), overall behavior is computed. This approaches thermodynamic behavior even though the much larger number of degrees of freedom existing in a real physical system are neglected (a physical system would have a number of degrees of freedom given by the Avogadro number, while the molecular dynamics simulation would at best be able to deal with $\sim 10^8$ degrees of freedom). In the case of bubbly flow the situation is more complicated at the conceptual level. A limited number of degrees of freedom are to be computed. These are appropriately counted using the resolved wave-number range for the continuous system considered here. A much larger number of degrees of freedom, the high wave-number range, is modeled. It would seem at this level that there might be some hope that a situation similar to that found in molecular dynamics would be found. This remains an open question until large scale computations are carried out. Irrespective of the result of these computations a fundamental problem still remains. The transport equations used in the numerical simulation, i.e. the Navier-Stokes equations, are themselves the result of averaging over the scales of molecular motion. In the case of multi-phase flow there is significant activity at the molecular level which influences the overall flow, namely that associated with the formation of a phase interface. The phase interface is almost universally represented as a singularity in the Navier-Stokes equations across which appropriate boundary conditions are applied. But the formation of an interface, that is the attainment of a specific shape, is still governed by processes at a molecular level. In numerical simulations of bubbly flow it is often assumed that reconstruction of a phase interface is possible just by using the Navier-Stokes equations. Typical procedures include advection of an interface by the surrounding flow field, or reconstruction of the interface from a void fraction distribution or level set function. Theoretical, *a priori* considerations, lead to the conclusion that none of these procedures fully captures the physics of interface formation. The practical success of such procedures is still an open point; even though qualitatively similar structures have been seen to develop, detailed experimental comparison is still lacking. Even more poignantly, simulations of bubble separation and coalescence in which no considerations of the energetics of the interface are made, should be regarded with a healthy dose of skepticism. In order to provide some theoretical guidance to the problem of interface formation, a study of the local processes involved is required. Such a study may be carried out at the molecular level or by a consideration of the local thermodynamics, especially the local free energy.

From the above considerations arise the principal subjects of investigation in this report. The main thrust is, as initially stated, in providing appropriate closures for the computation of complex bubbly flow. Part I concentrates on the first of the closure problems enumerated above, that of accounting for the effect of unresolved boundary layers in the vicinity of resolved bubbles. A first estimate of this effect is carried out by application of a viscid-inviscid interaction algorithm for axisymmetric bubbles. Though useful as a first attempt in quantifying the effect of unresolved boundary layers, the model is essentially limited to laminar flow. An important distinction with respect to the flow around solid objects arises early on in the study of bubble boundary layers. In classical boundary layer theory one may extend the methods developed for laminar boundary layers to the study of turbulent boundary layers by the definition of an appropriately enhanced momentum transfer term (e.g. the eddy viscosity). This is not possible for bubbles because the *bubble shape in itself is unsteady* under the influence of turbulent velocity fluctuations. Bubble oscillations excited by turbulent fluctuations provoke more fluctuations themselves and the conceptual framework for a simple eddy viscosity type treatment is lacking. Any treatment of a bubble in a surrounding turbulent velocity field must therefore provide a description of the changes in bubble shape also. Such a description is obtainable (in part) from a VOF or level-set method. The problem that then arises is how to account for unresolved boundary layers given a complete description of the turbulent flow field and the bubble on the scale of the bubble diameter. A method based upon the Helmholtz decomposition of the surrounding velocity field is presented in Part I.

In Part II, attention is shifted to the problem of constructing an appropriate SGS turbulence model. The approach taken here is to give a description of the SGS bubbles using a statistical thermodynamics approach. This alleviates many of the conceptual difficulties brought about by averaging procedures. Given the interest in small, SGS bubbles, these may safely be assumed to be of simple shapes, spherical or ellipsoidal, constrained by strong surface tension effects. Hydrodynamics provides an interaction potential between the bubbles. The bubbles may then be regarded as point singularities interacting through the surrounding fluid medium by means of a known potential, a situation akin to the interaction of gas molecules for instance. The additional hydrodynamic interactions lead to a modification of the constitutive relationships between stress and strain for the fluid, which now depend on the local void fraction distributions. The system has been shown to exhibit a phase transition between a clustered and a dispersed bubble state. It is shown in this part how the phase transition is intimately connected to the modification of the turbulent momentum transfer observed in bubbly flow. A renormalization group technique is suitable to the analysis of the phase transition and provides a SGS eddy-viscosity type model which exhibits qualitatively different behavior as the void fraction passes through the transition point. A remarkable feature of the analysis is the role played by the turbulent fluctuations of the surrounding fluid as providing a random motion background, akin to the role of temperature in molecular systems. The SGS turbulence model is compared to available experimental results. A simple direct numerical simulation of the behavior of a periodic bubble array in a surrounding turbulent fluid is set up in order to test the model.

Finally, in Part III a local thermodynamic analysis of the processes of interface formation is carried out. The minimization of local free energy leads to a bubble reconstruction procedure which is physically based, as opposed to the purely geometric considerations applied in VOF or level-set methods. The advantages of such a procedure, especially in providing a pathway for investigating bubble coalescence and breakup are presented.

The report contains a number of appendices containing documentation of the various software developed in the course of this work or adjacent numerical procedures. Appendix A covers procedures useful for distribution of flow quantities over a Cartesian grid. Appendix B furnishes a documentation of the AxiBubble program in which the viscid-inviscid interaction algorithm presented in Part I is implemented.

Acknowledgments

The author wishes to acknowledge the support given by the staff at the Institut für Reaktorsicherheit, Forschungszentrum Karlsruhe that enabled the research presented in this report to be carried out. The research opportunities presented by Prof. D.G. Cacuci and Dr. G. Grötzbach are especially recognized. The useful discussions on some of the problems studied in this report with Dr. M. Wörner and DP W. Sabisch are also acknowledged.

Part I

Unresolved Boundary Layer Closures

Chapter 1

Problem formulation

A possible attack on the problem of numerical simulation of complex bubbly flow is to attempt to directly compute as much of the flow field as possible. This approach is akin to the direct numerical simulation of turbulence. However, it is unlikely that a full resolution of all bubbles and small scale flow structures in a complex industrial flow will be computed in the near future. This state of affairs leads to the consideration of the explicit computation of flow features down to the meso-scale, i.e. large, partially coherent turbulent structures and large bubbles, an approach close in spirit to that of large eddy simulation (LES).

It is known from analytical studies of the viscid flow around a bubble [33], [34], that the boundary condition of continuity of tangential stress across a fluid interface leads to the formation of a viscous boundary layer around a bubble immersed in a flow of moderately high Reynolds number (Re $\cong 10^1 \div 10^2$, based upon average velocity around bubble and equivalent diameter d). The boundary layer is quite thin, typically $\delta/d \sim 0.03$. A full resolution of a bubble's shape requires a mesh size Δx of at most $\Delta x = d/10$. For these bubbles, which are at the grid resolution limit, $\Delta x \cong 3.3\delta$. The conclusion is that the boundary layers around bubbles close to the grid resolution limit shall not be resolved.

Once we recognize that full resolution of bubble boundary layers is not feasible, the question that naturally arises is what influence this would have on the overall flow computation. The main physical observation that may be made is that the velocity values defined for a grid cell containing an unresolved boundary layer provide a poor estimate of the overall momentum contained in the cell. The specific means through which this fact arises in a computation is somewhat dependent on the numerical procedure adopted. The discussion here is made in terms of the volume-of-fluid (VOF) [14] approach. In this approach a spatial averaging procedure over the phase k is defined by

$$\langle \Psi_k \rangle_k \equiv \frac{1}{V_k} \int_V \Psi_k \gamma_k dV \,, \tag{1.1}$$

where Ψ_k is the quantity being averaged, γ_k is a phase indicator function, and V_k is the volume occupied by phase k. Averaging of the momentum equations for the two phases of an adiabatic bubbly flow leads to an averaged Navier-Stokes equation

$$\frac{\partial}{\partial t}\rho\mathbf{U} + \nabla\cdot(\rho\mathbf{U}\otimes\mathbf{U}) = -\nabla p + \nabla\cdot\boldsymbol{\tau} + \mathbf{f}^{ext} + \sum\mathbf{B}_k + \mathbf{m}^{\sigma}_{int} - \nabla\cdot\mathbf{D}\,. \tag{1.2}$$

The flow quantities that appear are averages computed from the component phases, i.e.

$$\rho = f\left\langle\rho_1\right\rangle_1 + (1-f)\left\langle\rho_2\right\rangle_2\,, \quad p = f\left\langle p_1\right\rangle_1 + (1-f)\left\langle p_2\right\rangle_2\,, \tag{1.3}$$

$$\mathbf{U} = \frac{1}{\rho}\left(f\left\langle\rho_1\right\rangle_1\left\langle\mathbf{U}_1\right\rangle_1 + (1-f)\left\langle\rho_2\right\rangle_2\left\langle\mathbf{U}_2\right\rangle_2\right), \quad f = V_1/(V_1+V_2)\,. \tag{1.4}$$

It is evident that in this approach the fluid's motion is described by the center-of-mass velocity of a control volume, the control volume implicitly defined by the spatial averaging procedure (1.1). Motion on scales beneath that of the control volume influence the larger scale motions through the last term in (1.2)

$$\mathbf{D} = f(1-f)\frac{\left\langle\rho_1\right\rangle_1\left\langle\rho_2\right\rangle_2}{\rho}\left(\left\langle\mathbf{U}_1\right\rangle_1 - \left\langle\mathbf{U}_2\right\rangle_2\right)\otimes\left(\left\langle\mathbf{U}_1\right\rangle_1 - \left\langle\mathbf{U}_2\right\rangle_2\right), \tag{1.5}$$

a term neglected in published works on the VOF method but noticed by Wörner [2]. This term expresses the difference between the true momentum flux and the average flux of the averaged momentum as seen from the relation

$$\mathbf{D} = \underbrace{f\left\langle\rho_1\right\rangle_1\left\langle\mathbf{U}_1\right\rangle_1\otimes\left\langle\mathbf{U}_1\right\rangle_1 + (1-f)\left\langle\rho_2\right\rangle_2\left\langle\mathbf{U}_2\right\rangle_2\otimes\left\langle\mathbf{U}_2\right\rangle_2}_{\text{True momentum flux}} - \underbrace{\rho\mathbf{U}\otimes\mathbf{U}}_{\text{Average momentum flux}} \tag{1.6}$$

and therefore shall be referred to as a *momentum drift-flux term* (MDF term) in the following. It is similar to the drift-velocity from the standard two-fluid approaches [16], [42].

Since the main focus of this investigation is on the bubbly flow of air in water it is of interest to carry out an initial order of magnitude analysis to ascertain the effect of the greatly different densities, $\rho_1 \gg \rho_2$, on the MDF term. Representative scalar velocities U_1, U_2 replace $\mathbf{U}_1, \mathbf{U}_2$ in this analysis and ρ_1, ρ_2 are assumed constant. The ratio of the MDF term to the averaged momentum flux is

$$\bar{D} \equiv \frac{D}{\rho U^2} = C\left(\frac{U_1 - U_2}{U}\right)^2 \tag{1.7}$$

with

$$C = \frac{f(1-f)\rho_1\rho_2}{\left[f\rho_1 + (1-f)\rho_2\right]^2} = \frac{x}{(1+x)^2}, \quad x \equiv \frac{1-f}{f}\frac{\rho_2}{\rho_1} = \frac{\alpha_2\rho_2}{\alpha_1\rho_1}. \tag{1.8}$$

The non-dimensional drift velocity term is

$$\overline{\Delta U} \equiv \frac{U_1 - U_2}{U} = \frac{U_1 - U_2}{a_1 U_1 + a_2 U_2} \tag{1.9}$$

with

$$a_1 = \frac{1}{1+x}, \quad a_2 = \frac{x}{1+x}. \tag{1.10}$$

From the above it is apparent that the controlling parameter is x, the product of the density and volume fraction ratios. The limiting cases of interest are:

1. $x \rightarrow 0$, in which case $a_1 \rightarrow 1$, $a_2 \rightarrow 0$,

   $$C \sim x, \quad \overline{\Delta U} = \frac{U_1 - U_2}{U_1} \tag{1.11}$$

   so the MDF term is small

   $$\bar{D} \sim x. \tag{1.12}$$

   For interface cells in air water flow this situation will be the most common except for cells in which the water fraction is very low, on the order of

   $$f \sim \frac{\rho_2}{\rho_1}. \tag{1.13}$$

2. $x \sim 1$, in which case $a_1 \rightarrow \frac{1}{2}$, $a_2 \rightarrow \frac{1}{2}$,

   $$C \sim \frac{1}{4}, \quad \overline{\Delta U} = 2\frac{U_1 - U_2}{U_1 + U_2} \tag{1.14}$$

   $$\bar{D} \sim \frac{1}{2}\frac{U_1 - U_2}{U_1 + U_2}. \tag{1.15}$$

3. $x \rightarrow \infty$, in which case $a_1 \rightarrow 0$, $a_2 \rightarrow 1$,

   $$C \sim \frac{1}{x}, \quad \overline{\Delta U} = \frac{U_1 - U_2}{U_2} \tag{1.16}$$

   $$\bar{D} \sim \frac{1}{x}. \tag{1.17}$$

Given that the drift velocity $\overline{\Delta U}$ cannot significantly exceed unity, we see that the MDF term is generally small for air-water bubbly flow with the significant exception of those cells in which the water fraction is on the order of the density ratio. This is another aspect of the stiffness induced by the widely different fluid densities. This observation immediately brings out the importance of an accurate interface reconstruction procedure and f advection algorithm. The MDF term acts basically as a source term for the averaged momentum equations (1.2), showing in which cells the difference between the true momentum flux of the two phases is not well approximated by the center of mass momentum flux. We see that the source distribution may be expected to be quite concentrated for air-water flows, namely in those cells in which $f \approx 10^{-3}$ (fig. 1.1).

The main objective of this part is to develop physical models capable of accurately estimating the contribution of the MDF term to the overall momentum transport in a bubbly flow.

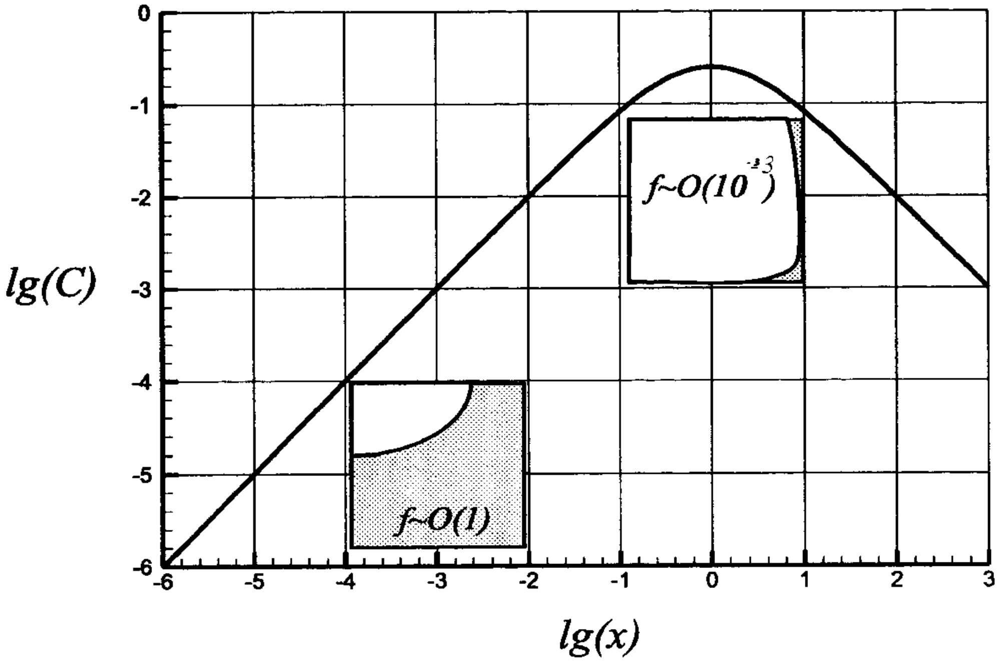

Figure 1.1: Log 10 plot of $C(x)$ with visual representation of types of interface cells associated with x values for air-water flow.

Chapter 2

A Boundary Element Method for Axisymmetric Bubbles

A first approach to the problem of determining the contribution of the MDF term is to limit one's attention to laminar flow conditions and use boundary layer theory to estimate **D**. The results thus obtained may furnish a first estimate of the MDF term. Admittedly, the application of such a model to a large scale computation of bubbly flow is limited in scope. One may confidently apply such a model only to bubbles for which *local* conditions are nearly laminar. The size of such bubbles would be at most $10 \div 100$ times the viscous cut-off length.

The method adopted in the boundary element (BEM) treatment of a bubble is that of viscid-inviscid interaction. The potential flow field around a bubble is first determined by solving an integral equation for a singularity distribution on the bubble surface. This procedure is an extension and refinement of that developed in [29]. Attention is limited to axisymmetric bubbles. The presentation of the boundary element method follows that from an earlier report [3] with some modifications that have improved the overall robustness of the method.

2.1 Potential flow around a non-buoyant axisymmetric bubble

2.1.1 Differential equation formulation

The problem to be solved is to determine the velocity potential ϕ and axisymmetric bubble shape $\Sigma = \{r = r(t),\, z = z(t)\}$ that satisfy

$$\begin{cases} \Delta\phi = 0 \\ \left.\dfrac{\partial\phi}{\partial n}\right|_{\Sigma} = 0 \\ |\nabla\phi|_{\Sigma}^{2} = U^{2} = 2\mathcal{H} - \gamma \end{cases} \tag{2.1}$$

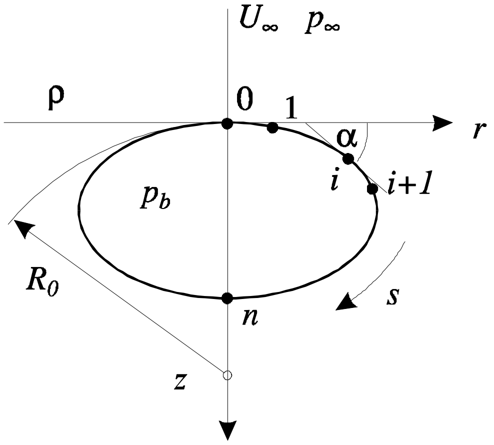

Figure 2.1: Geometric description and discretization of an axisymmetric bubble.

where γ is the shape parameter introduced in [29],

$$\gamma = \left(p_b - p_\infty - \frac{\rho U_\infty^2}{2} \right) \left(\frac{\rho U_\infty^2}{2} \right)^{-1} \tag{2.2}$$

and $\mathcal{H}$ is the mean curvature. The second boundary condition in (2.1) arises from the normal stress boundary condition for a bubble with constant internal pressure

$$p_b = p_\infty + \frac{\rho}{2}(U_\infty^2 - U^2) + 2\sigma\mathcal{H} \tag{2.3}$$

after expressing all quantities in non-dimensional terms. The reference velocity is U_∞ and the reference length is $D = 2\sigma/\rho U_\infty^2$. The bubble is assumed to be placed in a uniform flow of velocity U_∞ of a liquid with density ρ and surface tension σ. The mean curvature is given by

$$\mathcal{H} = \frac{1}{2} \left(\frac{d\alpha}{dt} + \frac{\sin \alpha}{r} \right) \tag{2.4}$$

where $\alpha(t)$ is the angle between the r axis and the tangent vector at arc length t along the bubble (fig. 2.1). The parameter t is assumed to be the arc length so we have

$$r' = \cos \alpha, \quad z' = \sin \alpha \, . \tag{2.5}$$

The Weber number is defined by

$$W = \frac{2\rho r_e U_\infty^2}{\sigma} \tag{2.6}$$

with r_e the radius of a sphere having the same volume as the bubble.

2.1.2 Integral equation formulation

The differential problem (2.1) may be reformulated as an integral equation for the function f introduced in [29] defined as $f = \phi - z$. The integral equation is

$$f(t) = \int_0^L N(s,t) f(s) ds + g(t) \tag{2.7}$$

with the kernel

$$N(s,t) = 2r(s) \left[-\sin\alpha(s) \frac{\partial \mathcal{G}}{\partial r}(s,t) + \cos\alpha(s) \frac{\partial \mathcal{G}}{\partial z}(s,t) \right] \tag{2.8}$$

and the inhomogeneous term

$$g(t) = \int_0^L 2r(s) \mathcal{G}(s,t) \cos\alpha(s)\, ds = \int_0^L G(s,t)\, ds\ . \tag{2.9}$$

The variables s, t are used to denote the arc parameter under and outside of the integral sign respectively. Coordinates outside the integral sign are denoted by $(R, Z) = (r(t), z(t))$ and those inside by $(r, z) = (r(s), z(s))$. The axisymmetric Green function $\mathcal{G}(s,t)$ is defined by

$$\mathcal{G}(s,t) = \mathcal{G}[r, z, R, Z] = -\frac{1}{\pi} \frac{K(k)}{\sqrt{(r+R)^2 + (z-Z)^2}}$$

with K the complete elliptic integral of first kind

$$K = K(k) \equiv \int_0^{\pi/2} \frac{d\theta}{\sqrt{1 - k^2 \sin^2\theta}}$$

of modulus

$$k = 2\sqrt{\frac{r\,R}{(r+R)^2 + (z-Z)^2}}\,. \tag{2.10}$$

The details of obtaining (2.7) from (2.1) are presented in [3]. Note that the function f goes to zero far away from the bubble using the reference lengths and velocities adopted here.

2.1.3 Numerical solution of the integral equation

Discrete description of the bubble geometry

A uniform discretization $\{0 = t_0, t_1, \dots, t_{n-1}, t_n = L\}$ of the bubble semi-perimeter L is introduced,

$$t_k = t_{k-1} + h,\ k = 1, 2, \dots, n\,, \tag{2.11}$$

with the step size $h = L/n$. A discrete approximation to the bubble geometry is specified by the nodal values $\alpha_k = \alpha(t_k)$. From these the cylindrical coordinates r, z may be determined by solving the differential equations

$$\left\{ \begin{array}{c} r'(t) = \cos\alpha(t) \\ r(t_0) = 0 \end{array} \right. , \quad \left\{ \begin{array}{c} z'(t) = \sin\alpha(t) \\ z(t_0) = 0 \end{array} \right. . \tag{2.12}$$

To solve these equations, for given nodal tangent directions α_k, the spline interpolations of the $\cos(\alpha_k)$ and $\sin(\alpha_k)$ are integrated.

Splitting of kernel into singular and non-singular parts

For a bubble of known shape, given in the parametrized form $r = r(t)$, $z = z(t)$, the integral equation (2.7) is solved by reduction to a linear system through the application of numerical quadrature. The kernel $N(s,t)$ is separated into a regular part $N_1(s,t)$ and a singular part $N_2(s,t)$

$$N(s,t) = N_1(s,t) + N_2(s,t) \,, \tag{2.13}$$

$$N_1(s,t) = -\frac{2r}{\pi} \left\{ \frac{e}{k^2} \frac{E - (1-k^2)K}{[(r+R)^2 + (z-Z)^2]^{1/2}} - \frac{(z-Z)Kr'}{[(r+R)^2 + (z-Z)^2]^{3/2}} \right\} , \tag{2.14}$$

$$N_2(s,t) = -\frac{2r}{\pi} \frac{(r+R)\sin\alpha}{[(r+R)^2 + (z-Z)^2]^{3/2}} K \,. \tag{2.15}$$

The complete elliptic integral of the second kind

$$E = E(k) \equiv \int_0^{\pi/2} \sqrt{1 - k^2 \sin^2\theta} \, d\theta \,, \tag{2.16}$$

and the auxiliary function

$$e = \frac{k}{1-k^2} \left(-\sin\alpha \frac{\partial k}{\partial r} + \cos\alpha \frac{\partial k}{\partial z} \right) \tag{2.17}$$

$$= \frac{(z-Z)r' - (r+R)z'}{(r+R)^2 + (z-Z)^2} + \frac{(r-R)z' - (z-Z)r'}{(r-R)^2 + (z-Z)^2} \,, \tag{2.18}$$

have been introduced. The $e(s,t)$ function is continuous along a smooth bubble

$$\lim_{s \to t} e(s,t) = \frac{1}{2} \left(\frac{d\alpha}{dt} - \frac{\sin\alpha}{R} \right) . \tag{2.19}$$

The limiting value of the regular kernel as $s \to t$ is

$$\lim_{s \to t} N_1(s,t) = \frac{1}{2\pi} \left(\frac{\sin\alpha}{R} - \frac{d\alpha}{dt} \right) . \tag{2.20}$$

The limiting behavior of the singular kernel is

$$N_2(s \to t, t) \sim -\frac{\sin\alpha}{2\pi R} K(k \to 1) \sim -\frac{\sin\alpha}{2\pi R} \ln \frac{4}{\sqrt{1-k^2}}\bigg|_{k\to 1}. \tag{2.21}$$

The leading order behavior of the modulus $k(s,t)$ as $s \to t$ is given by

$$k(s,t) \cong 1 - \frac{(s-t)^2}{8R^2} \tag{2.22}$$

so the leading order behavior of N_2 is

$$N_2(s,t) \cong -\frac{\sin\alpha}{2\pi R} \ln \frac{8R}{|s-t|}. \tag{2.23}$$

Approximation of integral equation by numeric quadrature

A linear system for the nodal values $f_k = f(t_k)$ is obtained from (2.7) by applying the integral equation at the nodes t_k

$$f_k = \int\limits_0^L N(s,t_k) f(s)\, ds + g_k \tag{2.24}$$

with, $g_k = g(t_k)$, $k = \overline{1, n-1}$. The integrals are split along subintervals containing Q nodes

$$\int\limits_0^L N(s,t_k) f(s)\, ds = \sum_{i=1}^{n_R} \int\limits_{(i-1)Rh}^{iRh} N(s,t_k) f(s) ds \tag{2.25}$$

$$g_k = \int\limits_0^L G(s,t_k)\, ds = \sum_{i=1}^{n_R} \int\limits_{(i-1)Rh}^{iRh} N(s,t_k) f(s) ds \tag{2.26}$$

with $R = Q - 1$, $n_R = n/R$. Numerical quadrature rules using Q points are applied over each subinterval.

For regular integrands we have

$$I_{1,j}^k = \int\limits_{(i-1)Rh}^{iRh} N_1(s,t_k) f(s) ds \cong h \sum_{l=0}^{R} A_l N_1(s_{j(l)}, t_k) f_{j(l)} \tag{2.27}$$

$$j(l) = (i-1)R + l \tag{2.28}$$

where A_l are the quadrature coefficients. These are determined so that the quadrature formula is exact for polynomials of degree up to R

$$\sum_{l=0}^{R} l^m A_l = \frac{R^{m+1}}{m+1}, \quad m = 0, \dots, R. \tag{2.29}$$

The same quadrature rule is applied for the integrals of $N_2(s, t_k)$, $G(s, t_k)$ when these remain regular within the integration interval, that is when $k \notin [(i-1)R, iR]$. If $k \in [(i-1)R, iR]$, $N_2(s, t_k)$, $G(s, t_k)$ are singular within the integration interval. The singularity is of the logarithmic type and therefore integrable. An appropriate numeric treatment is to factor out the singular factor and use a weighted quadrature rule

$$I_{2,j}^k = \int_{(i-1)Rh}^{iRh} N_2(s, t_k) f(s) ds = \int_{(i-1)Rh}^{iRh} \ln \frac{8r_k}{|s - t_k|} \bar{N}_2(s, t_k) f(s) ds \tag{2.30}$$

$$\cong h \sum_{l=0}^{R} B_l^k \bar{N}_2(s_{j(l)}, t_k) f_{j(l)} \tag{2.31}$$

$$J_j^k = \int_{(i-1)Rh}^{iRh} G(s, t_k) ds = \int_{(i-1)Rh}^{iRh} \ln \frac{8r_k}{|s - t_k|} \bar{G}(s, t_k) ds \tag{2.32}$$

$$\cong h \sum_{l=0}^{R} B_l^k \bar{G}(s_{j(l)}, t_k). \tag{2.33}$$

The logarithmic weight function is given by the leading order behavior of N_2 and G (2.23). It is natural therefore that the functions from which a logarithmic factor has been forced are regular

$$\lim_{s \to t} \bar{N}_2(s, t) = -\frac{\sin \alpha(t)}{2\pi R}, \quad \lim_{s \to t} \bar{G}(s, t) = -\frac{\cos \alpha(t)}{\pi}. \tag{2.34}$$

The B_l quadrature coefficients are again determined so that the quadrature formulas are exact for polynomials of degree up to R

$$\sum_{l=0}^{R} (iR - R + l - k)^m B_l^k = L_m^k, \quad m = 0, \dots, R, \tag{2.35}$$

with the analytical evaluation of the intervening integrals

$$L_m^k = \begin{cases} A_i & (i-1)R = k \\ A_i - A_{i-1} & (i-1)R < k < iR \\ -A_{i-1} & iR = k \end{cases} \tag{2.36}$$

$$A_i = \frac{(iR - k)^{m+1}}{m+1} \left[\ln \frac{(8r_k/h)}{|iR - k|} + \frac{1}{m+1} \right]. \tag{2.37}$$

The system (2.35) must be solved for each k since the local values r_k and h appear in the rhs. This is to be expected since the leading order behavior depends on the local geometry according to (2.23).

Approximating linear system

After applying the numerical quadrature rules a linear system

$$\mathbf{M} \cdot \mathbf{f} = \mathbf{p} \tag{2.38}$$

is obtained for the vector of unknowns

$$\mathbf{f} = \left[\begin{array}{cccc} f_0 & f_1 & \dots & f_n \end{array} \right]^T . \tag{2.39}$$

The matrix elements are collected from each term in the quadrature rules using the algorithm

```
$\mathbf{M} \leftarrow 0, \quad \mathbf{p} \leftarrow 0$                                   (2.40)
  $k = 1, \dots, n-1$
    $M_{k,k} \leftarrow 1$
    $i = 1, \dots, n-1$
      $l = 0, \dots, R$
        $j = (i-1)R + l$
        $M_{k,j} \leftarrow M_{k,j} + hA_l N_1(s_j, t_k)$
      $if \quad (i-1)R \le k \le iR$
        $Compute \quad B_l$
        $l = 0, \dots, R$                                                 (2.41)
          $j = (i-1)R + l$
          $M_{k,j} \leftarrow M_{k,j} + hB_l \bar{N}_2(s_j, t_k)$
          $p_k \leftarrow p_k - hB_l \bar{G}(s_j, t_k)$
      $else$
        $l = 0, \dots, R$
          $j = (i-1)R + l$
          $M_{k,j} \leftarrow M_{k,j} + hA_l N_2(s_j, t_k)$
          $p_k \leftarrow p_k - hA_l G(s_j, t_k)$
```

The system is closed by imposing

$$f_0' = 0, \quad f_n' = 0 \, . \tag{2.42}$$

Accuracy of discretization

The above numerical procedure was tested for accuracy by comparison to the known analytical solution around an ellipsoidal bubble (see B.4). The relative errors in the potential and the surface velocity

$$\varepsilon_1^\phi = \frac{\|\phi_n - \phi_{exact}\|_1}{\|\phi_{exact}\|_1}, \quad \varepsilon_\infty^\phi = \frac{\|\phi_n - \phi_{exact}\|_\infty}{\|\phi_{exact}\|_\infty} \tag{2.43}$$

$$\varepsilon_1^u = \frac{\|u_n - u_{exact}\|_1}{\|u_{exact}\|_1}, \quad \varepsilon_\infty^u = \frac{\|u_n - u_{exact}\|_\infty}{\|u_{exact}\|_\infty} \tag{2.44}$$

are represented in fig. 2.2 in logarithmic coordinates. The results show improved accuracy as Q increases. The overall procedure does not attain the theoretically predicted Q order of convergence. Analysis of the results shows that this is due mainly to implementation of the end conditions. The differences in the convergence analysis in the ∞-norm and the 1-norm bring this out. However, for $Q \geq 4$ at least third order accuracy is achieved which is sufficient for practical computations.

2.1.4 Procedure for determining the bubble shape

For a given bubble shape the procedure presented in 2.1.3 allows the computation of potential at the nodal points. An iterative procedure is now set up to compute the bubble shape so that the second boundary condition in (2.1) is also satisfied. The bubble shape is described by the vector of geometric quantities $X = \left[\begin{array}{cccccc} R_0 & \alpha_1 & \cdots & \alpha_{n-1} & R_n & L \end{array} \right]^T$ with $R_{0,} R_n$ the radii of curvature at the fore and aft stagnation points. We must impose $n+2$ conditions to determine X. The normal stress boundary condition is applied at nodes $k = 0, \ldots, n$

$$F_k(X) = U_k^2 + \gamma - \left(\frac{d\alpha}{dt} \right)_k - \frac{\sin \alpha_k}{r_k} \tag{2.45}$$

and the condition of closed bubble shape is imposed

$$F_{n+1}(X) = r_n \tag{2.46}$$

to obtain the final equation needed.

A nonlinear system of equations has thus been obtained

$$\mathbf{F}(\mathbf{X}) = 0 \tag{2.47}$$

with $\mathbf{F} = \{F_0(X), \ldots, F_{n+1}(X)\}^T$. This system may be solved using standard algorithms. The Broyden secant update available in the IMSL routine DNEQBF is used here.

2.1.5 Geometric characteristics of the bubble

After the solution to (2.47) is found the volume V, surface area A and aspect ratio χ of the bubble may be computed

$$V = \frac{2\pi}{3} \int_0^L (r'z - z'r) r \, dt = \frac{4\pi}{3} r_e^3 \tag{2.48}$$

$$A = 2\pi \int_0^L r(t) \, dt \tag{2.49}$$

$$\chi = \frac{r_{\max}}{z_n - z_0}. \tag{2.50}$$

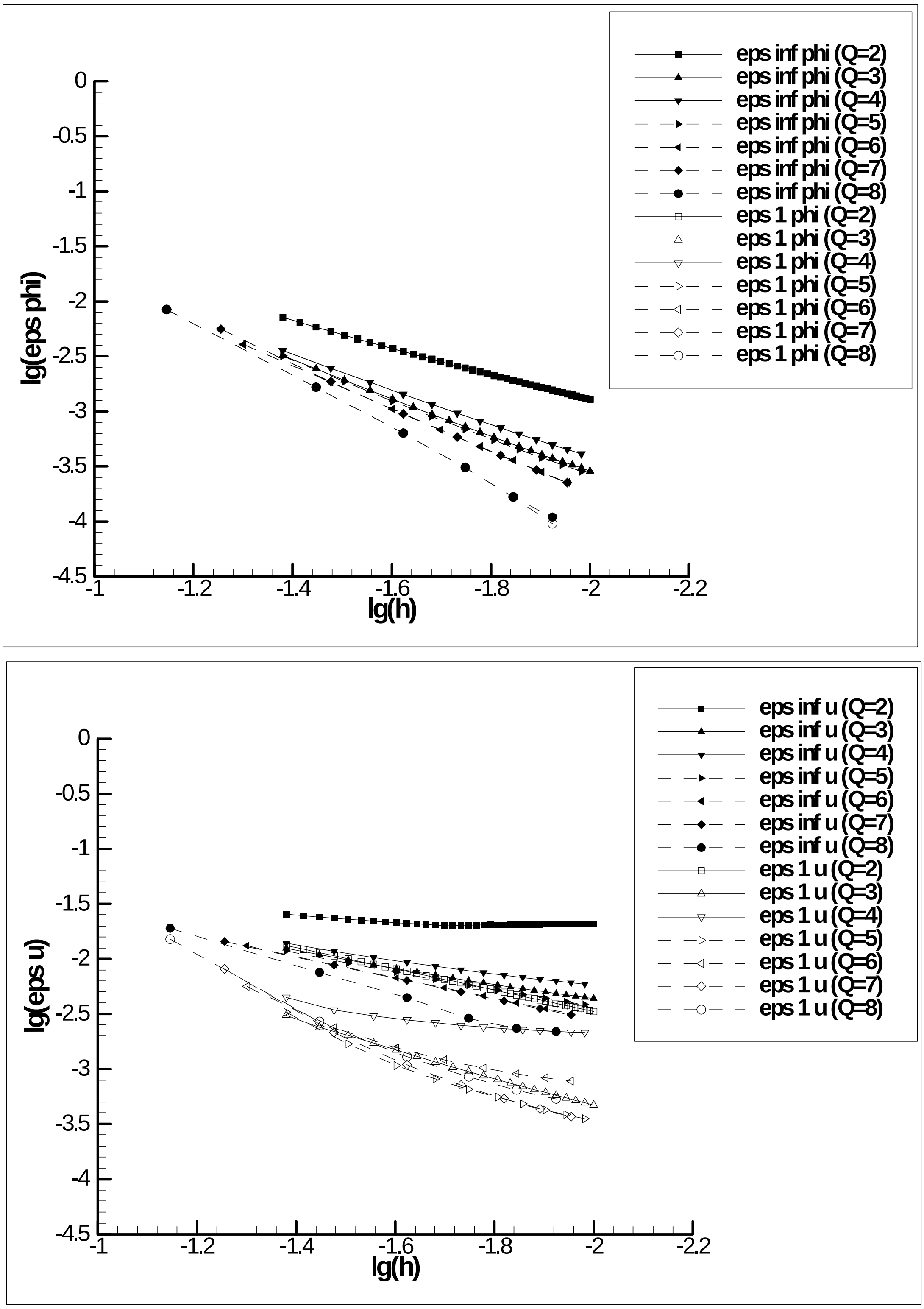

Figure 2.2: Convergence of the integral equation solver.

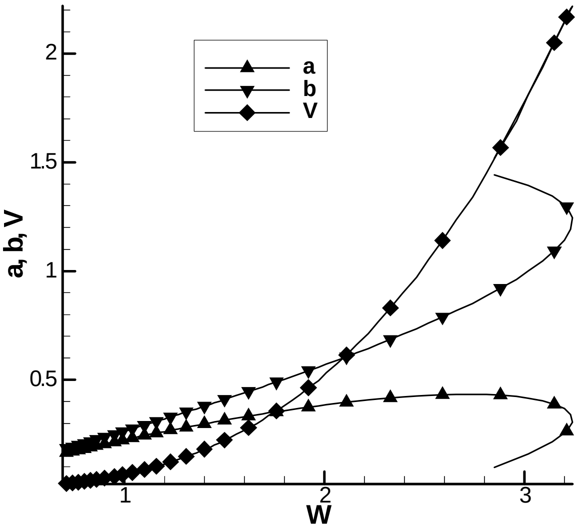

Figure 2.3: Dependence of bubble semiaxes a, b and volume V on Weber number W for $\beta = 0$.

When expressing r_e in units of $D = 2\sigma/\rho U_\infty^2$ the Weber number is simply

$$W = 4r_e. \tag{2.51}$$

The dependence of the above quantities on the Weber number W is given in fig. 2.3-2.4. The evolution of bubble shapes as γ increases is given in fig. 2.5-2.6

2.1.6 Evaluation of the velocity field around a bubble of known shape

Computation of velocity by convolution

Once a bubble shape has been determined by the secant procedure presented above one may compute the velocity potential and the velocity at any point (R, Z) in the flow field outside of the bubble. The integral equation (2.7) may be written as

$$f(R, Z) = \int_0^L N^{ext}(s; R, Z)\, f(s) ds + g^{ext}(R, Z) \tag{2.52}$$

with

$$N^{ext}(R, Z) = r(s) \left[-\sin\alpha(s) \frac{\partial \mathcal{G}}{\partial r}(s; R, Z) + \cos\alpha(s) \frac{\partial \mathcal{G}}{\partial z}(s; R, Z) \right] \tag{2.53}$$

$$g^{ext}(t) = \int\limits_0^L r(s) \mathcal{G}(s; R, Z) \cos\alpha(s)\, ds. \tag{2.54}$$

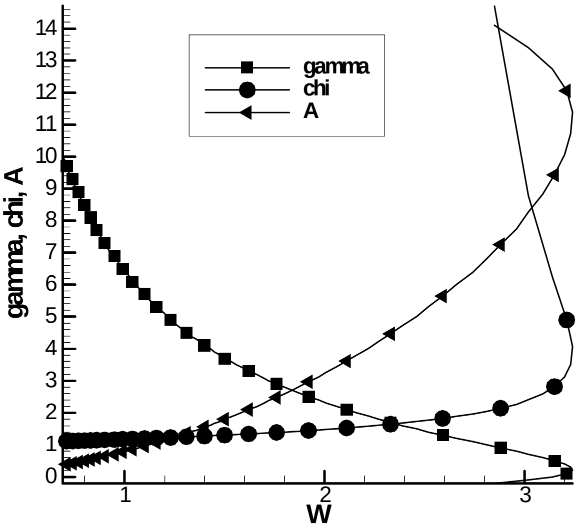

Figure 2.4: Dependence of bubble aspect ratio χ and area A on Weber number W for $\beta = 0$. Also relationship between γ parameter and W.

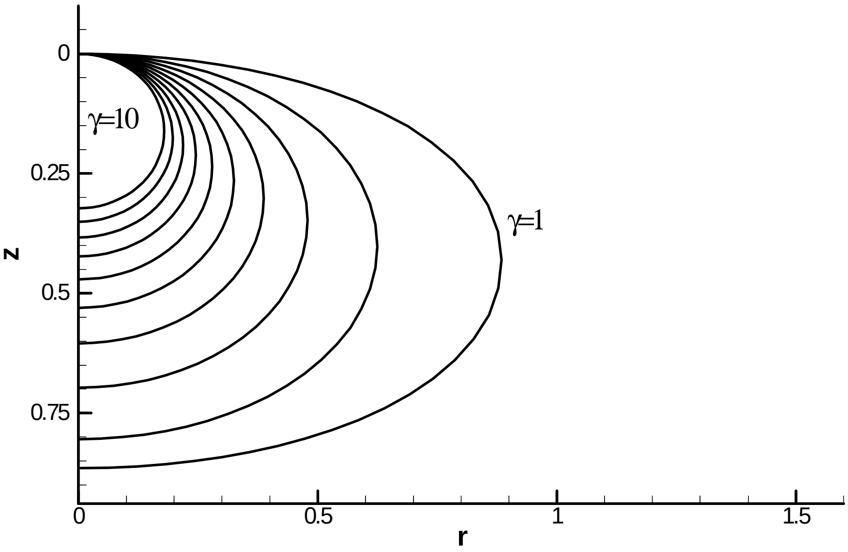

Figure 2.5: Sequence of bubble shapes at $\beta = 0$ for $\gamma = 1, 2, \ldots, 10$.

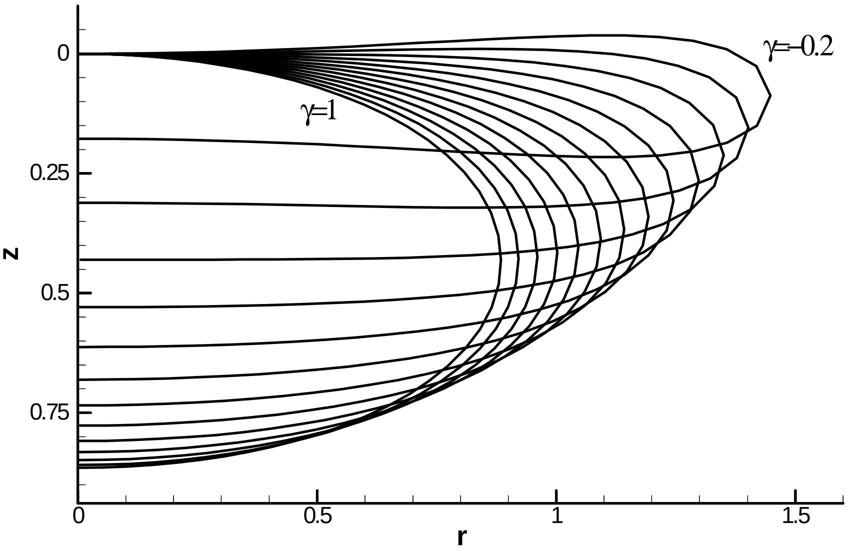

Figure 2.6: Sequence of bubble shapes at $\beta = 0$ for $\gamma = -0.2, -0.1, \ldots, 1.0$.

The change in numeric factors with respect to (2.7) is a result of not evaluating f on the bubble surface. Since

$$\vec{V} = \nabla \Phi = \nabla f + \vec{e}_z \tag{2.55}$$

we have

$$\vec{V} = \int_0^L \nabla_{(R,Z)} N^{ext}(s; R, Z)\, f(s) ds + \nabla_{(R,Z)} g^{ext}(R, Z) + \vec{e}_z\,. \tag{2.56}$$

The above formula may be evaluated analytically but the computations are excessively lengthy. A quicker evaluation is given by numeric approximation,

$$\vec{V}(R, Z) = \frac{\Phi(R + h, Z) - \Phi(R - h, Z)}{2h} \vec{e}_r + \frac{\Phi(R, Z + h) - \Phi(R, Z - h)}{2h} \vec{e}_z\,. \tag{2.57}$$

Formula (2.57) works well for points which are not very close to the bubble surface. The evaluation of the potential is however error-prone very close to the bubble surface (within one tenth of the bubble diameter, fig. 2.7) due to the large variations in the N^{ext} kernel. This may be remedied by evaluating the integral using a much finer discretization of the bubble boundary than that needed for finding $f(s)$, typically using $10N$ integration nodes. The resulting algorithm is, however, inefficient because it requires $O(40N\,M^3)$ operations to evaluate the velocities on a 3D grid with M nodes in one direction.

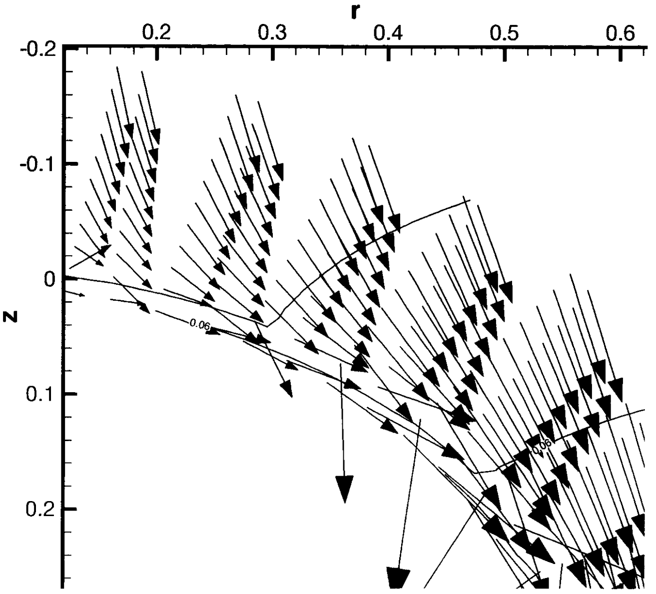

Figure 2.7: Evaluation of velocity field close to the bubble surface using (2.57). Large numerical errors are observed.

Computation of velocity by applying a fast Poisson solver

A more computationally effective procedure is to compute Φ on a rectangular mesh enclosing the bubble by solving the Neumann problem from the first two equations in (2.1), the bubble shape being known. Since the values of f on the bubble surface have already been computed to a high order of precision by the integral equation solver, it is possible to apply a fast Poisson solver to compute Φ on the mesh by adapting the procedures pioneered in [26]. The cost in this case is $O(5M^3 \log_2^2 M)$, typically leading to a reduction in the computation time by a factor of $4 \div 8$ by comparison to (2.57). Moreover, the fast Poisson solver approach is better suited to evaluation of the momentum drift-flux term $\mathbf{D}$ from (1.5) and to extensions of the viscid-inviscid model to three dimensions.

The representation of f by single and double layers. The integral equation (2.7) was obtained from an application of Green's second identity giving

$$f(\vec{p}) = \frac{1}{4\pi} \int_S \left[f(\vec{q}) \frac{\partial}{\partial n} \left(\frac{1}{|\vec{p} - \vec{q}|} \right) - \frac{\partial f}{\partial n}(\vec{q}) \frac{1}{|\vec{p} - \vec{q}|} \right] dS \,, \tag{2.58}$$

with $\vec{p}$, $\vec{q}$ position vectors pointing to points not on the bubble, and on the bubble, respectively. One may interpret (2.58) as giving a representation of f through a single layer potential of intensity

$$\mu = \frac{1}{4\pi} \frac{\partial f}{\partial n} \tag{2.59}$$

and a double layer potential of intensity

$$\sigma = -\frac{1}{4\pi} f \, . \tag{2.60}$$

One knows from general potential theory [18] that the values of the single layer potential on a point on S specify the jump in the normal derivative of the represented function when crossing the point

$$\left[\frac{\partial f}{\partial n} \right] = \frac{\partial f}{\partial n}^{+} - \frac{\partial f}{\partial n}^{-} = 4\pi\mu = \frac{\partial f}{\partial n} \tag{2.61}$$

where the rhs term is evaluated on S. Similarly, the double layer potential specifies the jump in the function itself

$$f^{+} - f^{-} = f \tag{2.62}$$

from which tangential derivatives may also be computed

$$\frac{\partial^k f}{\partial t^k}^{+} - \frac{\partial^k f}{\partial t^k}^{-} = \frac{\partial^k f}{\partial t^k} = f^{(k)} \tag{2.63}$$

to whatever order k needed.

From (2.61) and (2.63) jumps in the higher derivatives may also be computed. Derivatives up to the third order shall be required later and are evaluated here. Consider that a local, curvilinear coordinate system (t, n) is defined. On the bubble we would have $n = 0$, with t corresponding to the arc length along the bubble perimeter. We suppose that, in general, changes in (t, n) give the arc length traversed so that the Lamé parameters are $L_t = L_n = 1$. Explicit construction of the (t, n) coordinate system would seem to be necessary in order to evaluate the normal derivatives. This is difficult generally, but fortunately not actually required since we can use the bubble boundary conditions and the Laplace equation to conveniently transform normal derivatives to tangential derivatives. Let us now compute the jumps in Φ and its derivatives up to third order. Recall that $f = \Phi - z$, with z and its derivatives continuous so that jumps in f are equal to jumps in Φ

$$\left[\frac{\partial^k \Phi}{\partial t^k} \right] = \left[\frac{\partial^k f}{\partial t^k} \right] = f^{(k)}, \quad k = 0, 1, \ldots \quad . \tag{2.64}$$

Turning now to the normal derivatives we have

$$\left[\frac{\partial \Phi}{\partial n} \right] = \frac{\partial \Phi}{\partial n} - \frac{\partial z}{\partial n} = -\cos\alpha \tag{2.65}$$

because of the no through-flow boundary condition ($\partial\Phi/\partial n_0 = 0$) and the definition of α. Differentiation of (2.65) along n leads to

$$\left[\frac{\partial^2 \Phi}{\partial n^2} \right] = \frac{\partial^2 \Phi}{\partial n^2} - \frac{\partial^2 z}{\partial n^2} \, . \tag{2.66}$$

Both Φ and z are harmonic and the values of these functions and their derivatives are so defined that

$$\frac{\partial^2\Phi}{\partial t^2}+\frac{\partial^2\Phi}{\partial n^2}=0, \quad \frac{\partial^2 z}{\partial t^2}+\frac{\partial^2 z}{\partial n^2}=0 \tag{2.67}$$

on the bubble surface S also (the Laplace operator has the standard form in the (t,n) coordinate system since the coordinates are orthonormal). Therefore we have

$$\left[\frac{\partial^2\Phi}{\partial n^2}\right]=-\left(\frac{\partial^2\Phi}{\partial t^2}-\frac{\partial^2 z}{\partial t^2}\right)=-f''. \tag{2.68}$$

Another differentiation leads to

$$\left[\frac{\partial^3\Phi}{\partial n^3}\right]=\frac{\partial^3\Phi}{\partial n^3}-\frac{\partial^3 z}{\partial n^3}=-\frac{\partial}{\partial n}\left(\frac{\partial^2\Phi}{\partial t^2}-\frac{\partial^2 z}{\partial t^2}\right)=-\frac{\partial^2}{\partial t^2}\left(\frac{\partial\Phi}{\partial n}-\frac{\partial z}{\partial n}\right) \tag{2.69}$$

or, taking the no-through flow boundary condition into account,

$$\left[\frac{\partial^3\Phi}{\partial n^3}\right]=-\alpha''\sin\alpha-(\alpha')^2\cos\alpha\,. \tag{2.70}$$

Finally, we have the cross derivative jumps

$$\left[\frac{\partial^2\Phi}{\partial t\partial n}\right]=\alpha'\sin\alpha, \quad \left[\frac{\partial^3\Phi}{\partial t^2\partial n}\right]=\alpha''\sin\alpha+(\alpha')^2\cos\alpha, \quad \left[\frac{\partial^3\Phi}{\partial t\partial n^2}\right]=-f'''\,. \tag{2.71}$$

The equivalent Poisson equation on a rectangular grid. One may use (2.64)-(2.71) to solve the problem

$$\triangle\Phi=J \tag{2.72}$$

$$\Phi|_R=F\,, \tag{2.73}$$

with R a rectangular domain enclosing the bubble, rather than the original problem (2.1). The boundary values of Φ on R may be computed by evaluating the convolution integral (2.52). The size of R may be made large enough to ensure that F is evaluated with good precision. The right hand side term J accounts for the jumps that occur when crossing the bubble surface. The above problem (2.72) may be solved efficiently by applying a fast Poisson solver over the *entire* domain R if a method of determining the effect of the bubble surface singularities is devised. Consider the discretization of the Laplace operator using a standard seven point stencil

$$\triangle\Phi\cong\triangle_h\Phi=\frac{1}{h^2}\left(\Phi_{i+1,j,k}+\Phi_{i-1,j,k}+\Phi_{i,j+1,k}+\Phi_{i,j-1,k}+\right. \tag{2.74}$$

$$\left.\Phi_{i,j,k+1}+\Phi_{i,j,k-1}-6\Phi_{i,j,k}\right) \tag{2.75}$$

This discretization of second order if the stencil arms do not cross the bubble surface. If a stencil arm does cross the surface the jumps in Φ and its derivatives across the surface must be accounted for. Consider that the $(i,j,k)-(i+1,j,k)$ stencil arm is cut by the bubble surface into subsegments of length h_1 and h_2. A second order approximation of the second x derivative of Φ is now

$$\begin{aligned}(\Phi_{xx})_{i,j,k} = \frac{1}{h^2}\left(\Phi_{i+1,j,k} - 2\Phi_{i,j,k} + \Phi_{i-1,j,k}\right) - \\ \frac{1}{h^2}\left([\Phi] + h_2[\Phi_x] + \frac{h_2^2}{2}[\Phi_{xx}] + \frac{h_2^3}{6}[\Phi_{xxx}]\right).\end{aligned} \tag{2.76}$$

A derivation of the above formula may be found in 3.1.4. The more convenient subscript notation for the derivatives is used from here on. This formula is obtained by patching the Taylor series up to and from $x = x_{i+1} - h_2 = x_i + h_1$. The $J_{i,j,k}$ term is in this case

$$J_{i,j,k} = [\Phi] + h_2[\Phi_x] + \frac{h_2^2}{2}[\Phi_{xx}] + \frac{h_2^3}{6}[\Phi_{xxx}]. \tag{2.77}$$

Similar formulas are derived for other intersections of the bubble surface and stencil arms. If the $(i,j,k)-(i-1,j,k)$ arm is intersected formula (2.76) with h_2 replaced by $-h_2$ is applied, $x = x_{i-1} + h_2 = x_i - h_1$. Derivatives along other directions are found by circular permutation. The relations between derivatives along the Cartesian axis and those along the bubble surface are

$$\begin{cases} \dfrac{\partial}{\partial x} = \cos\theta\left(\cos\alpha\dfrac{\partial}{\partial t} - \sin\alpha\dfrac{\partial}{\partial n}\right) \\ \dfrac{\partial}{\partial y} = \sin\theta\left(\cos\alpha\dfrac{\partial}{\partial t} - \sin\alpha\dfrac{\partial}{\partial n}\right) \\ \dfrac{\partial}{\partial z} = \left(\sin\alpha\dfrac{\partial}{\partial t} + \cos\alpha\dfrac{\partial}{\partial n}\right) \end{cases}. \tag{2.78}$$

where the circumferential coordinate θ has been introduced. Analogous relations hold for jumps

$$\begin{cases} [\Phi_x] = \cos\theta\left([\Phi_t]\cos\alpha - [\Phi_n]\sin\alpha\right) \\ [\Phi_y] = \sin\theta\left([\Phi_t]\cos\alpha - [\Phi_n]\sin\alpha\right) \\ [\Phi_z] = [\Phi_t]\sin\alpha + [\Phi_n]\cos\alpha \end{cases}. \tag{2.79}$$

Relations for the higher order derivatives may be found by repeated application of the above formulas

$$\begin{cases} \dfrac{\partial^k}{\partial x^k} = \cos^k\theta\left(\cos\alpha\dfrac{\partial}{\partial t} - \sin\alpha\dfrac{\partial}{\partial n}\right)^k \\ \dfrac{\partial^k}{\partial y^k} = \sin^k\theta\left(\cos\alpha\dfrac{\partial}{\partial t} - \sin\alpha\dfrac{\partial}{\partial n}\right)^k \\ \dfrac{\partial^k}{\partial z^k} = \left(\sin\alpha\dfrac{\partial}{\partial t} + \cos\alpha\dfrac{\partial}{\partial n}\right)^k \end{cases}. \tag{2.80}$$

This leads to the following jump relations

$$\left\{\begin{array}{l} [\Phi_{xx}] = \cos^2\theta \left([\Phi_{tt}]\cos^2\alpha - 2\,[\Phi_{tn}]\cos\alpha\sin\alpha + [\Phi_{nn}]\sin^2\alpha\right) \\ [\Phi_{yy}] = \sin^2\theta \left([\Phi_{tt}]\cos^2\alpha - 2\,[\Phi_{tn}]\cos\alpha\sin\alpha + [\Phi_{nn}]\sin^2\alpha\right) \\ [\Phi_{zz}] = [\Phi_{tt}]\sin^2\alpha + 2\,[\Phi_{tn}]\sin\alpha\cos\alpha + [\Phi_{nn}]\cos^2\alpha \end{array}\right. \tag{2.81}$$

$$\left\{\begin{array}{l} [\Phi_{xxx}] = \cos^3\theta \left([\Phi_{ttt}]\cos^3\alpha - 3\,[\Phi_{ttn}]\cos^2\alpha\sin\alpha + 3\,[\Phi_{tnn}]\cos\alpha\sin^2\alpha + [\Phi_{nnn}]\sin^3\alpha\right) \\ [\Phi_{yyy}] = \sin^3\theta \left([\Phi_{ttt}]\cos^3\alpha - 3\,[\Phi_{ttn}]\cos^2\alpha\sin\alpha + 3\,[\Phi_{tnn}]\cos\alpha\sin^2\alpha + [\Phi_{nnn}]\sin^3\alpha\right) \\ [\Phi_{zzz}] = [\Phi_{ttt}]\sin^3\alpha + 3\,[\Phi_{ttn}]\sin^2\alpha\cos\alpha + 3\,[\Phi_{tnn}]\sin\alpha\cos^2\alpha + [\Phi_{nnn}]\cos^3\alpha \end{array}\right. .$$

Replacing (2.64-2.71) in the above we obtain

$$\left\{\begin{array}{c} [\Phi_x] = (f' + \sin\alpha)\cos\alpha\cos\theta \\ [\Phi_y] = (f' + \sin\alpha)\cos\alpha\sin\theta \\ [\Phi_z] = f'\sin\alpha - \cos^2\alpha \end{array}\right. \tag{2.82}$$

$$\left\{\begin{array}{l} [\Phi_{xx}] = \left\{f''\left(\cos^2\alpha - \sin^2\alpha\right) - \alpha'\sin\alpha\sin 2\alpha\right\}\cos^2\theta \\ [\Phi_{yy}] = \left\{f''\left(\cos^2\alpha - \sin^2\alpha\right) - \alpha'\sin\alpha\sin 2\alpha\right\}\sin^2\theta \\ [\Phi_{zz}] = -\left\{f''\left(\cos^2\alpha - \sin^2\alpha\right) - \alpha'\sin\alpha\sin 2\alpha\right\}\sin\alpha \end{array}\right. \tag{2.83}$$

$$\left\{\begin{array}{c} [\Phi_{xxx}] = A\cos^3\theta, \quad [\Phi_{yyy}] = A\sin^3\theta \\ [\Phi_{zzz}] = f'''\left(\sin\alpha - 3\cos\alpha\right)\sin^2\alpha + \\ \left\{\alpha''\sin\alpha + (\alpha')^2\cos\alpha\right\}\left(3\sin\alpha - \cos\alpha\right)\cos^2\alpha \end{array}\right. \tag{2.84}$$

$$A = \left\{f'''\left(\cos^2\alpha - 3\sin^2\alpha\right)\cos\alpha + \left\{\alpha''\sin\alpha + (\alpha')^2\cos\alpha\right\}\left(-3\cos^2\alpha + \sin^2\alpha\right)\sin\alpha\right\}. \tag{2.85}$$

Note that in order to ensure second order accuracy of the Poisson solver the f function must be evaluated with fourth order precision and α with third order precision. The accuracy of the integral equation solver thus plays an essential role in the correct evaluation of the velocities through the fast Poisson solver technique presented here. When evaluating f, α and their derivatives care must be exercised that the required order of precision is obtained. The strategy adopted here is to use at least a fourth order integral equation solver and then use cubic interpolation for the *derivative* of f. This gives the minimum required $O(h^4)$ behavior for the function f itself. The following formulas give fourth order accurate approximations of f' on a uniform grid

$$f'_i = \frac{-25f_i + 48f_{i+1} - 36f_{i+2} + 16f_{i+3} - 3f_{i+4}}{12h} \tag{2.86}$$

$$f'_i = \frac{-3f_{i-1} - 10f_i + 18f_{i+1} - 6f_{i+2} + f_{i+3}}{12h} \tag{2.87}$$

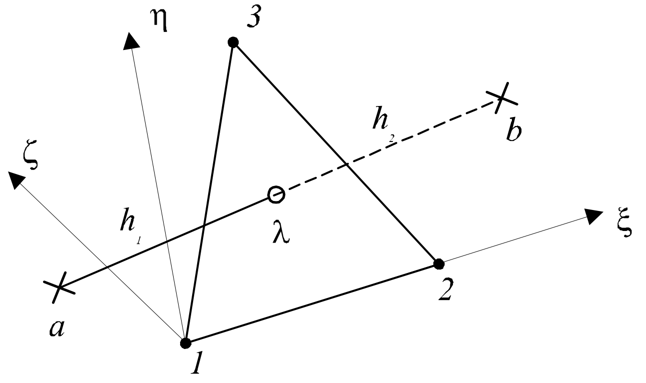

Figure 2.8: Intersection of stencil arm with a member of the bubble surface triangulation.

$$f_i' = \frac{f_{i-2} - 8f_{i-1} + 8f_{i+1} - f_{i+2}}{12h} \tag{2.88}$$

$$f_i' = \frac{-f_{i-3} + 6f_{i-2} - 18f_{i-1} + 10f_i + 3f_{i+1}}{12h} \tag{2.89}$$

$$f_i' = \frac{3f_{i-4} - 16f_{i-3} + 36f_{i-2} - 48f_{i-1} + 25f_i}{12h}\,. \tag{2.90}$$

Fourth order accurate formulas for the second derivatives are required at the end points

$$f_i'' = \frac{-10f_{i-5} + 61f_{i-4} - 156f_{i-3} + 214f_{i-2} - 154f_{i-1} + 45f_i}{24h^2} \tag{2.91}$$

$$f_i'' = \frac{45f_i - 154f_{i+1} + 214f_{i+2} - 156f_{i+3} + 61f_{i+4} - 10f_{i+5}}{24h^2}\,. \tag{2.92}$$

An alternative would be to apply the technique widely employed in integral equation analysis of using the integral equation formula (2.7) itself as an interpolation formula. This leads to a more complicated implementation though since new weight functions for the point of interest at coordinate t must be constructed.

Algorithm for intersection of bubble and discrete Laplace stencil. In order to apply the above formulas the intersections of the bubble surface with the discrete Laplace stencil must be determined. Consider the bubble surface to be given by a triangulation and let $(\vec{p}_1, \vec{p}_2, \vec{p}_3)$ be the position vectors of the vertices of one the triangles. A translation of the coordinate system so that $\vec{p}_1 = 0$ is convenient. It is assumed that the position vectors reflect this translation. An arm of the discrete Laplace stencil is given by the segment $(\vec{p}_a, \vec{p}_b)$ (fig. 2.8). A point on the stencil arm is given by

$$\vec{p}_\lambda = \vec{p}_a + \lambda(\vec{p}_b - \vec{p}_a)\,. \tag{2.93}$$

If $\vec{p}_\lambda$ lies in the plane defined by the triangle $(\vec{p}_1, \vec{p}_2, \vec{p}_3)$ then the volume of the tetrahedron $(\vec{p}_1, \vec{p}_2, \vec{p}_3, \vec{p}_\lambda)$ is zero, a condition which may be expressed as

$$\begin{vmatrix} 1 & 1 & 1 & 1 \\ 0 & x_2 & x_3 & x_a + \lambda(x_b - x_a) \\ 0 & y_2 & y_3 & y_a + \lambda(y_b - y_a) \\ 0 & z_2 & z_3 & z_a + \lambda(z_b - z_a) \end{vmatrix} = 0 \tag{2.94}$$

or, after expanding along the first column and using the determinant addition formula on the last,

$$\begin{vmatrix} x_2 & x_3 & x_a \\ y_2 & y_3 & y_a \\ z_2 & z_3 & z_a \end{vmatrix} + \lambda \begin{vmatrix} x_2 & x_3 & x_b - x_a \\ y_2 & y_3 & y_b - y_a \\ z_2 & z_3 & z_b - z_a \end{vmatrix} = 0\,. \tag{2.95}$$

Equation (2.95) has a single solution if

$$\begin{vmatrix} x_2 & x_3 & x_b - x_a \\ y_2 & y_3 & y_b - y_a \\ z_2 & z_3 & z_b - z_a \end{vmatrix} \neq 0\,. \tag{2.96}$$

If the determinant is zero, then the stencil arm is either completely in the triangle or parallel to it. If it is completely in the triangle, there are no discontinuities in the standard discrete approximation of the derivative along the stencil arm direction. If the stencil arm is parallel to the triangle, it does not cross the bubble surface within this triangle and again there are no discontinuities to be accounted for in the discrete Laplace operator. If (2.96) holds, the stencil arm crosses the plane defined by the $(\vec{p}_1, \vec{p}_2, \vec{p}_3)$. It is still necessary to verify whether the intersection point, denoted by $\vec{p}_0$, is inside the triangle. This is established in a local 2D coordinate system (ξ, η) in the plane of the triangle, centered on $\vec{p}_1$, and defined by the unit vectors

$$\vec{e}_\xi = \frac{\vec{p}_2}{||\vec{p}_2||}, \quad \vec{e}_\eta = \frac{\vec{p}_3 - (\vec{p}_3 \cdot \vec{e}_\xi)\vec{e}_\xi}{||\vec{p}_3 - (\vec{p}_3 \cdot \vec{e}_\xi)\vec{e}_\xi||}\,. \tag{2.97}$$

In the above, the fact that $\vec{p}_1 = 0$ was used. Global coordinates are transformed to local coordinates using the identity

$$\vec{p} = x\vec{i} + y\vec{j} + z\vec{k} = \xi\vec{e}_\xi + \eta\vec{e}_\eta + \zeta\vec{e}_\zeta \tag{2.98}$$

with

$$\vec{e}_\zeta = \vec{e}_\xi \times \vec{e}_\eta\,. \tag{2.99}$$

In the (ξ, η) plane one verifies that $\vec{p}_0$ is within the triangle by checking that it is one the same side of each of the triangles edges as the remaining node opposite the edge.

Assuming that in the $(\vec{p}_a, \vec{p}_b)$ segment $\vec{p}_a$ is always at the center of the discrete Laplace stencil, the lengths h_1, h_2 required in the approximation of a discontinuous derivative (2.76) are

$$h_1 = \lambda\, ||\vec{p}_b - \vec{p}_a||\,, \quad h_2 = (1 - \lambda)\, ||\vec{p}_b - \vec{p}_a||\ . \tag{2.100}$$

The algorithm for computing the J term from (2.72) is

```
Build bubble surface triangulation
Loop over $(x, y) = const$ lines
    Loop over triangulation
        If an intersection point within
        triangle is found then add effects to $J_{i,j,k}$
Loop over $(y, z) = const$ lines
    Loop over triangulation                          .        (2.101)
        If an intersection point within
        triangle is found then add effects to $J_{i,j,k}$
Loop over $(z, x) = const$ lines
    Loop over triangulation
        If an intersection point within
        triangle is found then add effects to $J_{i,j,k}$
```

2.2 Buoyancy effects

When the bubble is placed in a gravitational field g there is an additional change in the liquid pressure from this effect. The normal stress boundary condition now becomes

$$U^2 = 2\mathcal{H} - \gamma + \beta z \tag{2.102}$$

with

$$\beta = \frac{4\sigma g}{\rho U_\infty^4}. \tag{2.103}$$

The same numerical procedure is applied for the new boundary condition (2.102). The effect of gravitational forces upon the bubble geometry is presented in fig. (2.9)-(2.13). A remarkable result is the large change in fore-aft asymmetry observed as β increases (2.13). The change in bubble shape as β increases for $W = 2$ is shown in fig. 2.14.

A first comparison may be made with experimental results. Duineveld [8] studied the rise of air bubbles in highly purified water. Surfactant effects are thus minimized and the no tangential stress boundary condition is satisfied. For $W = 2.3$ the bubble shape is reasonably close to that measured (2.15) even when no viscous effects are considered. At the highest Weber number measured by Duineveld $W = 3.36$ the computed shape differs markedly from that measured (fig. 2.16). At this high Weber number the bubble's shape and rise velocity are unsteady however, with the bubble rising in a zigzag motion. The steady, axisymmetric model of the bubble used in the computation is therefore inappropriate.

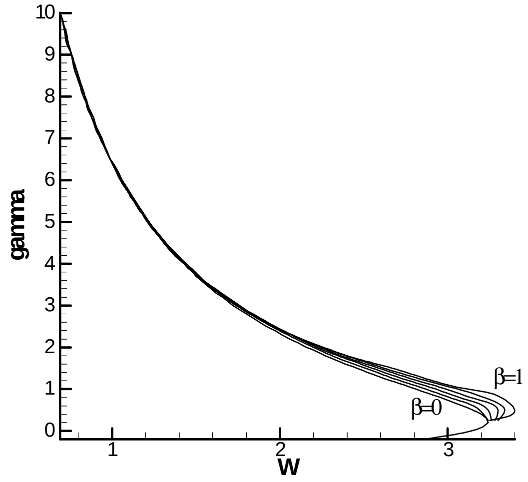

Figure 2.9: Effect of $\beta = 0, 0.2, 0.4, 0.6, 0.8, 1.0$ on (W, γ) relationship.

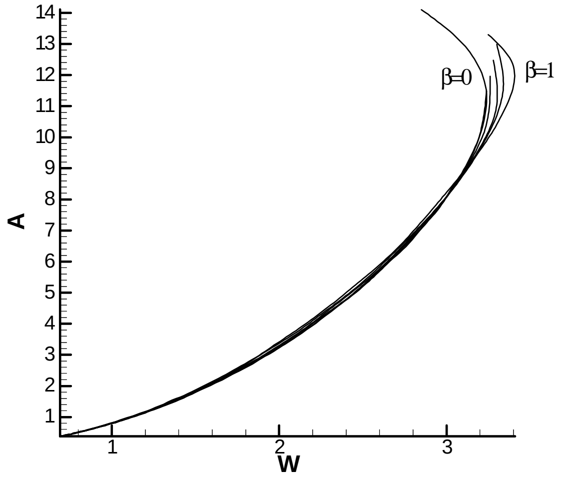

Figure 2.10: Effect of β on (W, A) relationship.

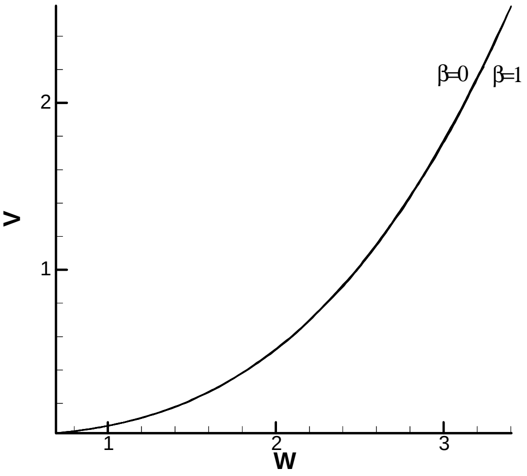

Figure 2.11: Effect of β on (W, V) relationship.

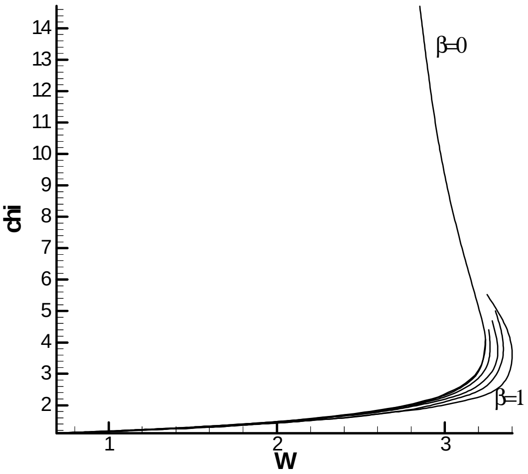

Figure 2.12: Effect of β on (W, χ) relationship.

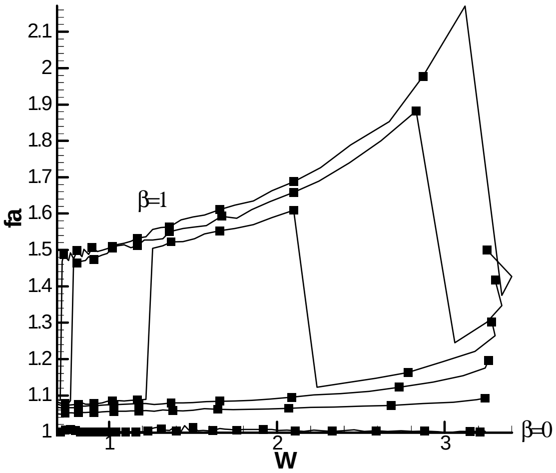

Figure 2.13: Effect of β on fore-aft asymmetry of the bubble. Some numerical noise is still apparent in the graph. The fore-aft asymmetry is the parameter most sensitive to numerical convergence effects.

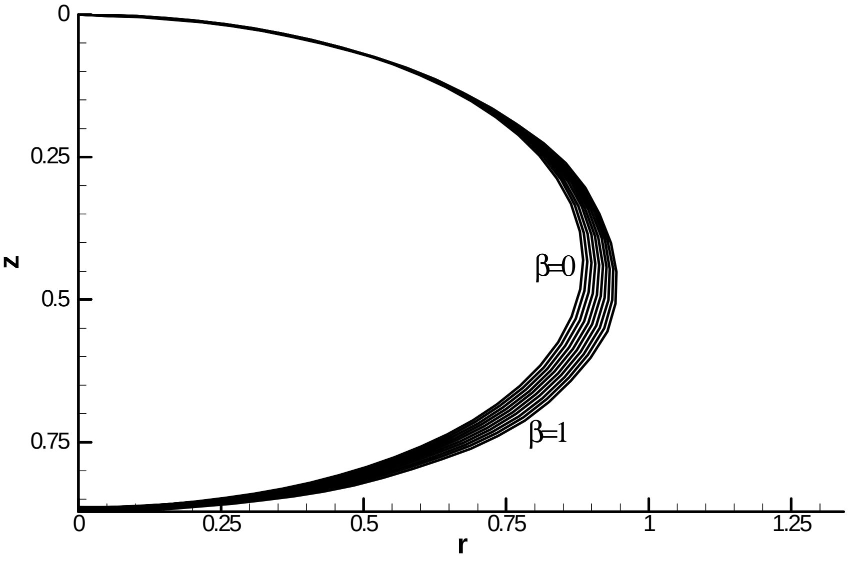

Figure 2.14: Change in shape for $W = 2$ bubble as β goes from 0 to 1 in increments of $\Delta\beta = 0.1$.

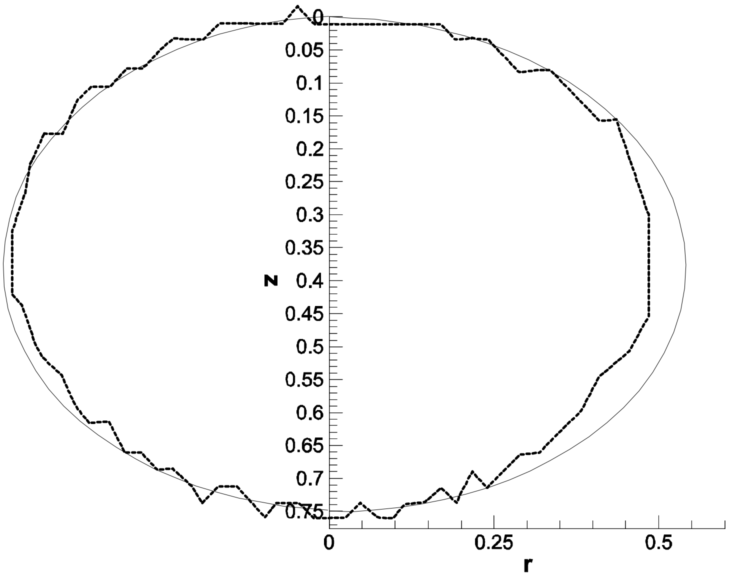

Figure 2.15: Comparison of computed (solid line) and experimental (dotted line, [8]) shape for a air bubble rising in pure water at $W = 2.3$. Computation without viscous effects. Streamwise bubble axis from computation is fitted to measurement by least squares method.

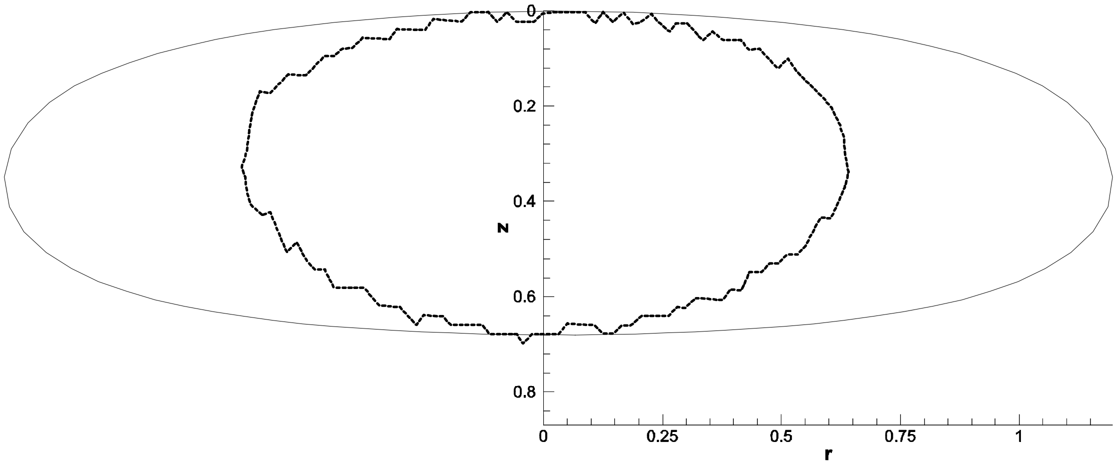

Figure 2.16: Comparison of computed (solid line) and experimental (dotted line, [8]) shape for a air bubble rising in pure water at $W = 3.36$. Computation without viscous effects.

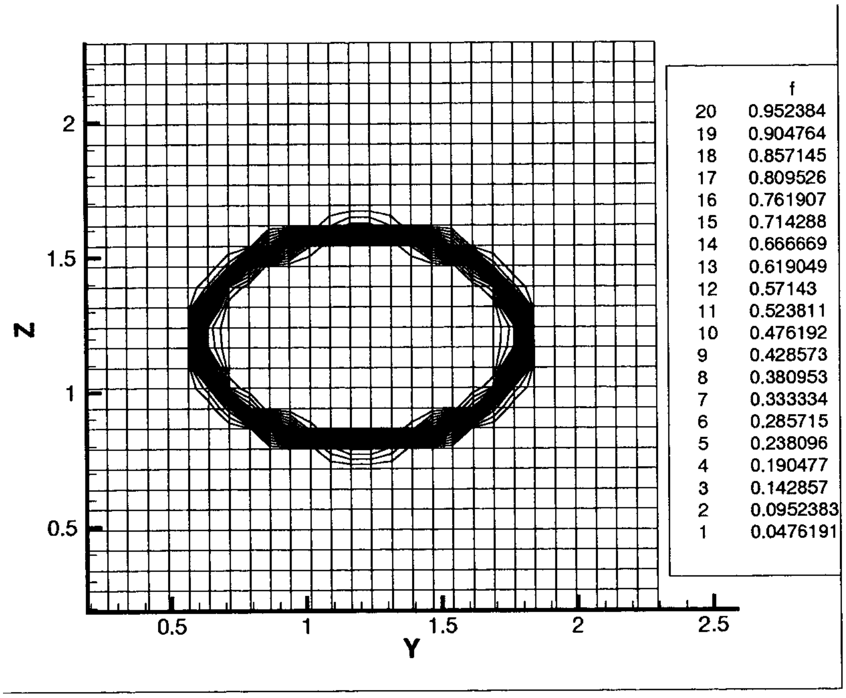

Figure 2.17: Void fraction distribution for a $W = 2.15$ bubble discretized over a rectangular 32x32x32 Cartesian grid in a $x = const$ plane.

2.3 Inviscid, axisymmetric momentum drift-flux term

A first estimate of the MDF term in (1.5) may be obtained by applying the above inviscid model. Note that the MDF term $\mathbf{D}$ reflects flow phenomena beneath the grid resolution of the VOF method. For any given discrete approximation of a bubble shape, the integral equation method presented above furnishes a more accurate description of the flow around a bubble than extrapolation from the velocities defined on the VOF grid. So even neglecting viscous effects it is of some interest to obtain some preliminary information on the magnitude of the MDF term. The void fraction distributions and norm of the divergence of the MDF term are shown in figures 2.17-2.20 for a $W = 2.15$ bubble at $\beta = 0$ and density ratio $\rho_2/\rho_1 = 0.001$ representative for an air bubble in water. One may note that the general features of the qualitative analysis presented in chapter 1 are observed. The bubble interface is captured along an average of two cells of the Cartesian grid so the bubble may be considered to be fully resolved within the framework of a VOF method. The MDF term varies in magnitude by a factor around 20 and shows spikes that are associated with the relative position of the bubble with respect to the Cartesian grid. Since a divergence is taken the MDF term is spread out over more cells of the Cartesian grid.

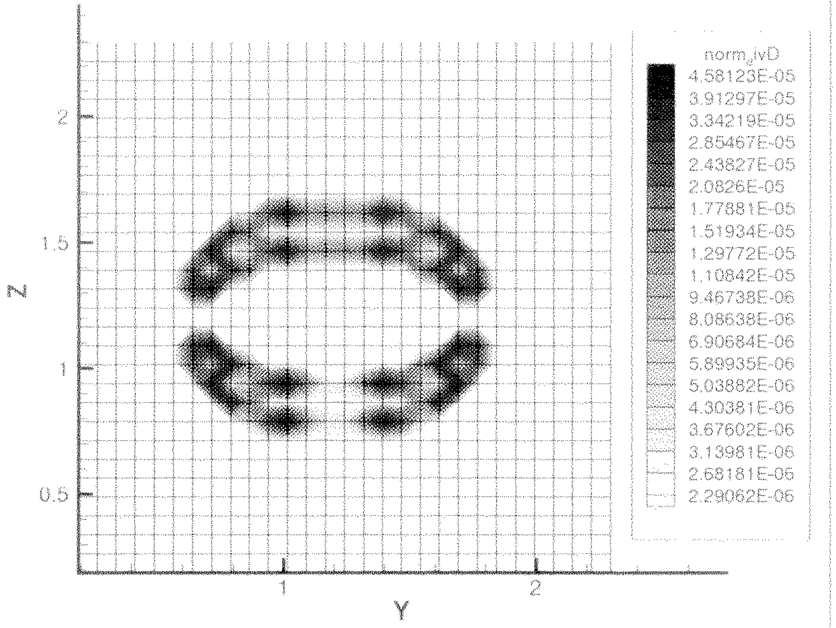

Figure 2.18: The norm of the divergence of the MDF term, $\|\nabla \cdot \mathbf{D}\|$ corresponding to plane in fig. 2.17.

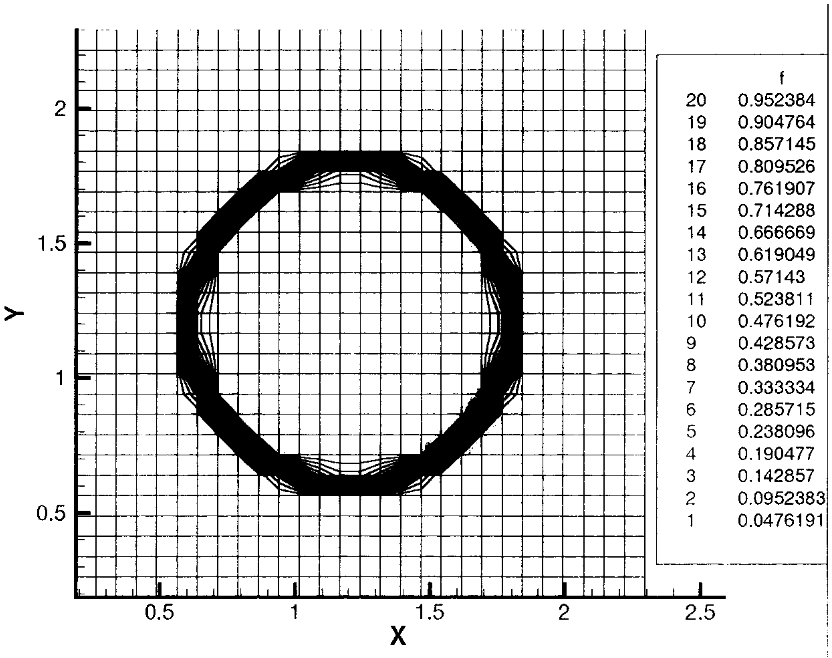

Figure 2.19: Same as previous figures for a $z = const$ plane.

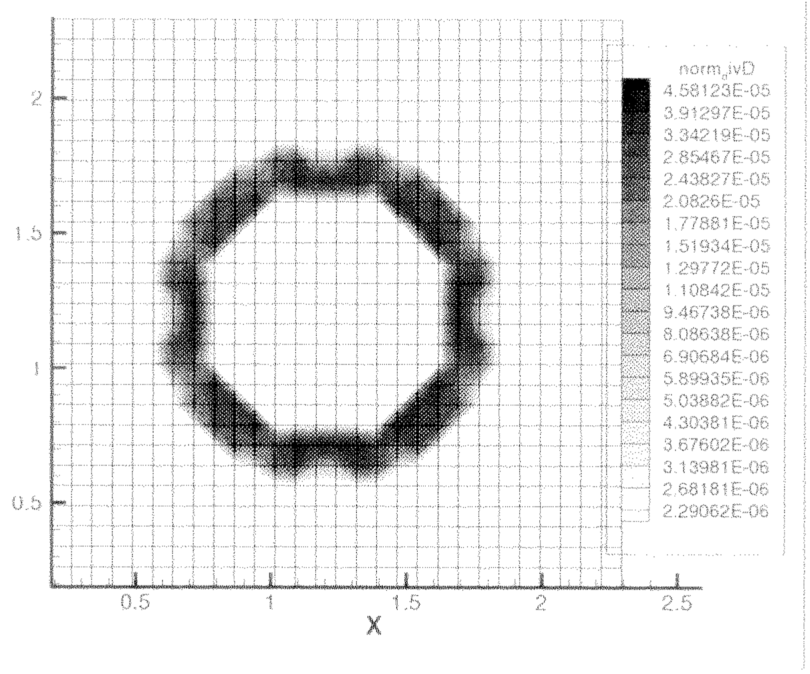

Figure 2.20: Same as 2.18 for a $z = const$ plane.

2.4 Viscous Effects

It is assumed that the bubble interface is incapable of sustaining a jump in tangential stress (i.e. there are no surfactants present). Since the gas inside the bubble is assumed to be stationary in the model considered here the continuity of tangential stress condition implies that

$$\frac{\partial u}{\partial n} = 0 \tag{2.104}$$

or that the normal derivative of the tangential velocity is zero at the bubble surface. This condition is not satisfied in general by the potential flow solution. In the immediate vicinity of the bubble surface a boundary layer therefore forms in which the viscous effects are significant and the potential flow field is modified so as to satisfy (2.104). There are two viscous effects that are important:

1. the effect of the normal deviatoric stress which will modify the bubble shape
2. the change in the velocity distribution very close to the bubble surface

2.4.1 Effect upon bubble shape

The bubble shape is determined by the balance of normal stresses. The pressure drop across the boundary layer is known to be negligible. The only viscous effect of significance is the normal deviatoric stress

$$2\rho\nu\frac{\partial u}{\partial n}. \tag{2.105}$$

After reducing the above term to non-dimensional form the normal stress boundary condition becomes [30]

$$F_k(X) = U_k^2 + \gamma - 2\mathcal{H}_k - \beta z_k - \frac{4}{\mathrm{Re}}\frac{\partial^2\phi}{\partial t^2} \tag{2.106}$$

where the Reynolds number is defined by

$$\mathrm{Re} = \frac{2r_e U_\infty}{\nu} \tag{2.107}$$

with r_e given in units of $D = 2\sigma/\rho U_\infty^2$. In general, the effect of the normal deviatoric stress upon the bubble shape is quite small, confirming the initial argument made in this chapter that the overall flow is dominated by non-viscous effects. Large effects are seen at the low Reynolds number range (Re ~ 50) when the flow changes from one being dominated by convection effects to one in which viscous effects become dominant (and therefore better described by the Stokes equations). Some of the changes in the geometric characteristics of the bubble brought about by changes in the Reynolds number are shown in figures 2.21-2.22. A comparison of a computed bubble with the Duineveld experiments is shown in fig. 2.23. There is no discernible change in the bubble shape by comparison to the inviscid computation.

2.4.2 Effect upon velocity distribution

The change in the velocity distribution close to the bubble surface may be modeled in a number of ways. One technique is to adapt the standard methods from boundary layer theory [40]. An example is the thesis by Bekkum [43] in which the Pohlhausen technique of fitting the velocity distribution with a fourth-degree polynomial is applied. This technique is appropriate if the boundary layer is not of negligible thickness. If the boundary layer thickness is negligible, then the analysis of Moore [33] is applicable. This basically amounts to a change in the boundary condition of the inviscid flow to account for the continuous tangential stress condition. Bekkum has shown [43] that the parameter separating the domains of applicability of the two techniques is the product of the curvature and the boundary layer thickness

$$k = \mathcal{H}\delta = \frac{\mathcal{H}}{\sqrt{\mathrm{Re}}} \tag{2.108}$$

since $\delta \sim 1/\sqrt{\mathrm{Re}}$. If $k = O(\delta)$ then the boundary layer thickness is negligible. If $k = O(1)$ the boundary layer has an appreciable thickness and the velocity distribution in this layer should be accounted for. It is of interest to verify the magnitude of the k parameter. The limit of applicability of the procedures described in this chapter

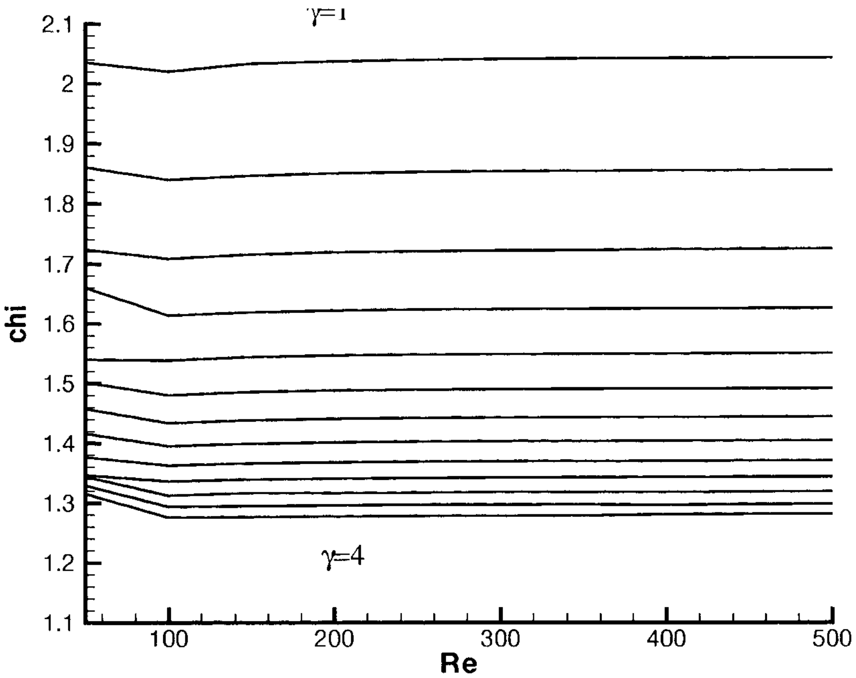

Figure 2.21: Variation of aspect ratio with Reynolds number ($\Delta\gamma = 0.25$).

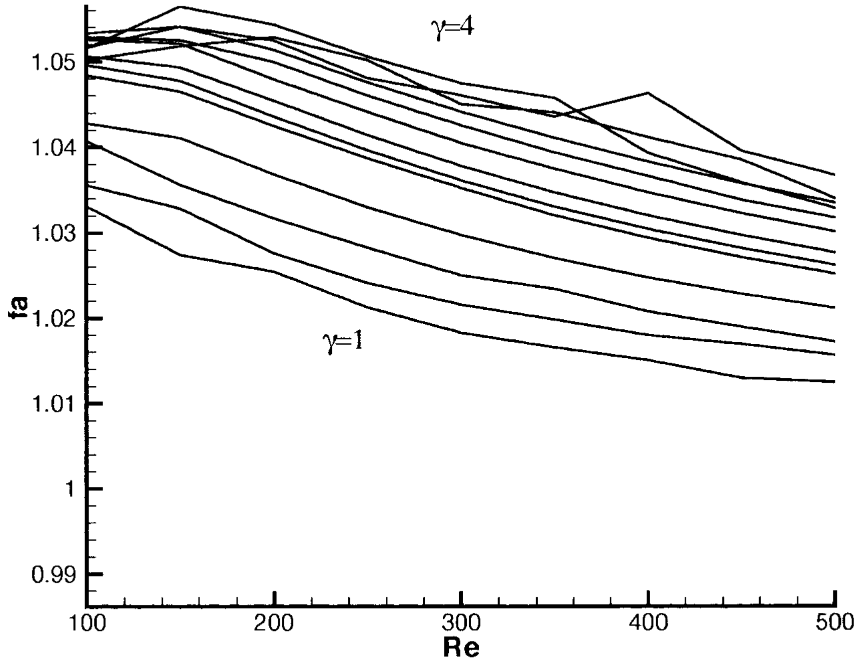

Figure 2.22: Variation of fore-aft asymmetry with Reynolds number ($\Delta\gamma = 0.25$). The parameter is sensitive to numerical errors.

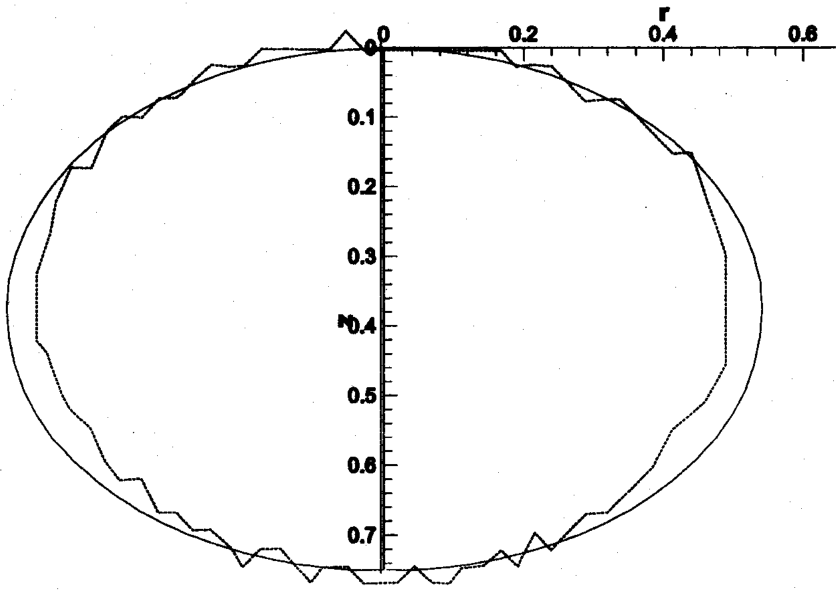

Figure 2.23: Comparison between computed shape (continuous line) and experimental result [8], $W = 1.919$, $\mathrm{Re} = 4.15 \cdot 10^5$.

is at $W \sim 3$ at which the axes ratio of the bubble is $\chi \sim 2$. The curvature along the computed bubble solution is shown in fig. 2.24 and has a maximum value of $\mathcal{H} \sim 5$. For the minimum Reynolds number at which convection effects dominate, $\mathrm{Re} \sim 100$, we would have $k = 0.5$ and for the normal range of Reynolds numbers representative for air-water bubbles $k \ll 0.1$. We conclude that the boundary layer thickness may be considered negligible in the general framework of the approximations of the present analysis. In order to account for the change in the velocity distribution close to the bubble surface it is sufficient to introduce a vorticity distribution on the bubble surface. The local intensity may be derived from the tangential stress boundary condition to be

$$\gamma = \frac{\partial \phi}{\partial t} \tag{2.109}$$

since a vorticity layer of intensity γ produces a velocity jump of magnitude γ and we need to model a jump from the zero velocity inside the bubble to the velocity $\partial\phi/\partial t = u$ on the bubble surface. The additional vorticity enters the computation of the velocity components $\vec{V} = u\vec{e}_r + v\vec{e}_z$ through the standard formulas

$$u(X,Y) = -\frac{1}{2\pi}\int_0^L \gamma(s)\frac{Y - y(s)}{\sqrt{[X - x(s)]^2 + [Y - y(s)]^2}}ds \tag{2.110}$$

$$v(X,Y) = \frac{1}{2\pi}\int_0^L \gamma(s)\frac{X - x(s)}{\sqrt{[X - x(s)]^2 + [Y - y(s)]^2}}ds. \tag{2.111}$$

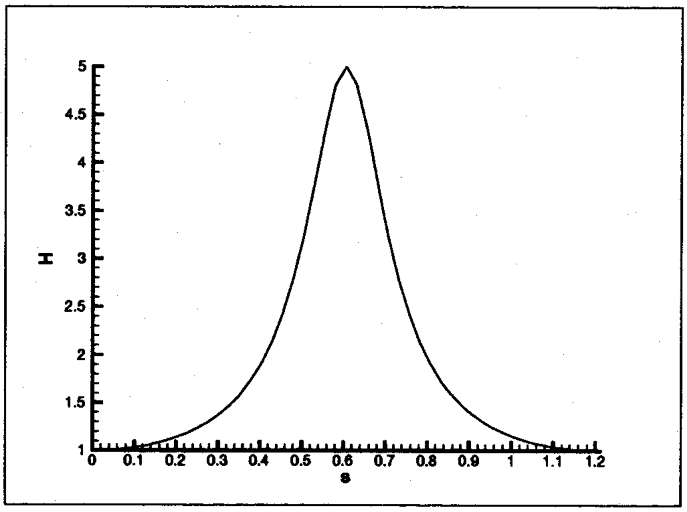

Figure 2.24: Curvature along a bubble with $\chi \sim 2$

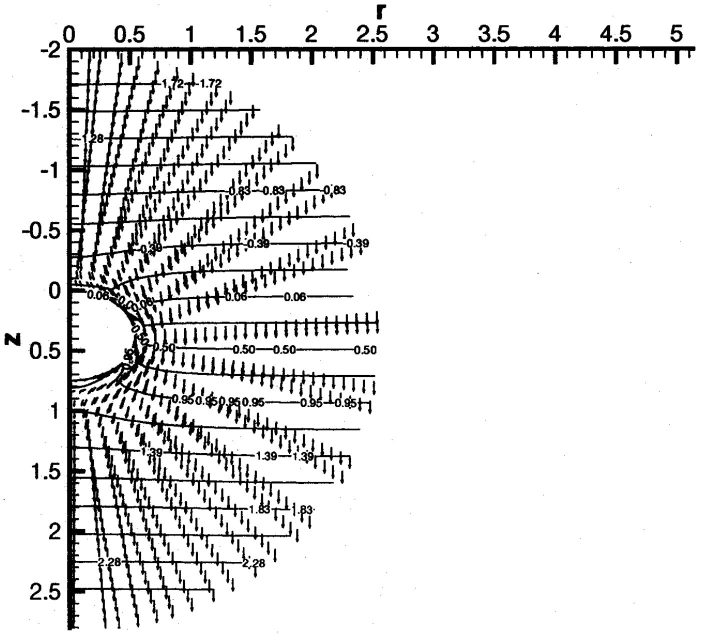

Figure 2.25: Velocity field around a bubble ($W = 1.9$) with viscous correction.

Chapter 3

The Dynamic Momentum Drift-Flux Model

We now turn to a different type of MDF model, that eliminates most of the restriction of the viscid-inviscid approach at the price of increased computational effort.

The basic components of the drift-flux model developed here, named the Dynamic Momentum Drift-Flux (DMDF) model, are now presented. The model is said to be "dynamic" in that the instantaneous bubble shape and surrounding flow conditions are taken into account; there is no over-all prescription for computing the drift-flux term. Rather an algorithm is devised to evaluate this term based upon local flow conditions, which change dynamically during the course of the VOF computation. In this section an overview of the model is presented. The explicit formulations for 2D and 3D are presented in sections §3.2 and §3.3, respectively. In the following it is assumed that a projection method is used to solve the averaged Navier-Stokes equations. This is not required though, and the DMDF model may easily be adapted to other VOF solvers. The main numerical algorithm used for the bubbly flow simulation shall be referred to as the *underlying* or *overall computational method.*

3.1 An overview

3.1.1 Decomposition of the velocity field

The flow is assumed to contain two phases which may be either incompressible or compressible. It is also assumed that the bubble shapes have been determined from the application of a reconstruction procedure to the f field and that a rectangular box surrounding a bubble may be identified (dilute bubbly flow). Let $\mathbf{U}^h$ be the numeric velocity field, at a given time step, as provided by the overall VOF computation on an uniform Cartesian grid. This field is defined only at the grid points $\mathbf{x}^h$. Let $\mathbf{U}$ be a continuous extension $\mathbf{U}^h$ that satisfies $\mathbf{U}(\mathbf{x}^h) = \mathbf{U}^h(\mathbf{x}^h)$. Typically $\mathbf{U}^h$, and therefore $\mathbf{U}$, would partially reflect the influence of the boundary conditions on the bubble interface through an appropriate momentum source, such as the $\mathbf{f}^{ext}$ term in (1.2). Effects below the grid resolution scale that give the difference in

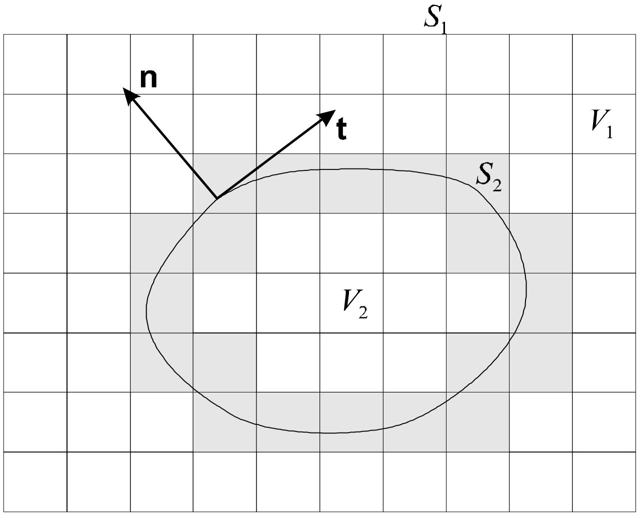

Figure 3.1: A resolved bubble in a local, rectangular bounding box. Irregular grid cells containing an interface are shaded.

average phase velocities $\langle \mathbf{U}_1 \rangle_1 - \langle \mathbf{U}_2 \rangle_2$ would not, however, be captured. Let $\mathbf{U}^*$ be a velocity field that includes the subgrid effects associated with a fluid interface. It is the goal of the DMDF model to accurately estimate and efficiently compute $\mathbf{U}^*$.

The presence of the phase interface induces additional vorticity so that the tangential stress boundary condition is satisfied. Surface phase changes would lead to sources and sinks of mass in the fluids on each side of the interface. It is, therefore, convenient to adopt a formulation in which the physical quantities of interest appear directly. From the $\mathbf{U}$ vector field we may compute the divergence and the curl

$$q = \nabla \cdot \mathbf{U}, \quad \boldsymbol{\omega}=\nabla \times \mathbf{U}\,. \tag{3.1}$$

The Helmholtz theorem states that a vector field of known divergence and curl may be decomposed into a part given by the gradient of a scalar potential and a part given by the curl of a vector potential

$$\mathbf{U} = \mathbf{U}^{\phi} + \mathbf{U}^{\psi} = \nabla \phi + \nabla \times \boldsymbol{\psi}\,. \tag{3.2}$$

The potentials satisfy Poisson equations

$$\triangle \phi = q, \quad \triangle \boldsymbol{\psi} = -\,\boldsymbol{\omega}\,, \tag{3.3}$$

assuming that a gauge has been chosen for $\boldsymbol{\psi}$ so that it is divergence-free. The representation of the velocity field by the potentials ϕ, $\boldsymbol{\psi}$ is adopted in the DMDF model since the physical quantities of interest q, $\boldsymbol{\omega}$ appear directly.

3.1.2 Modified representation due to interface effects

All the fields in (3.1)-(3.3) are continuously defined. As the grid cell size goes to zero the corresponding numeric fields from the VOF computation would have the above fields as their limits, i.e. $\mathbf{U}^h \to \mathbf{U}$ and so on. The influence of the interface upon these fields could come from an external force term $\mathbf{f}^{ext}$ defined to model interfacial effects. In the limit of infinitesimal control volumes all interfacial effects would be captured. In a numeric solution there is of necessity a finite grid cell size, so the external force term should be seen as capturing interfacial effects only at the grid resolution scale. The consequences of adopting a finite grid cell size are now investigated. The VOF formulation furnishes a discrete approximation of the source terms in (3.1),

$$q^h(\mathbf{x}^h) = \nabla_h \cdot \mathbf{U}^h, \quad \boldsymbol{\omega}^h(\mathbf{x}^h) = \nabla_h \times \mathbf{U}^h \,, \tag{3.4}$$

with ∇_h the discrete nabla operator defined on the underlying VOF grid. These source terms $q^h, \boldsymbol{\omega}^h$ do not fully take into account the presence of an interface. In the DMDF model a modified volume source distribution q^* and a modified vorticity distribution $\boldsymbol{\omega}^*$ are introduced. The source terms q^*, $\boldsymbol{\omega}^*$ are chosen to reflect boundary conditions on the interface, at the subgrid scale. This leads to a modified velocity field representation

$$\mathbf{U}^* = \nabla \phi^* + \nabla \times \boldsymbol{\psi}^* \,. \tag{3.5}$$

Along the interface normal stresses arising from fluid pressure, normal viscous stress and surface tension effects must balance. This boundary condition typically arises in solving a pressure equation for the overall flow field. This is not of direct interest in determining the drift-flux term, where only velocities appear. Of course the overall VOF computation is expected to provide the correct relationship between the phase-averaged pressure and the $\mathbf{U}^h$ velocity field.

If the interface is considered to be infinitesimal, tangential stresses must be the same on both sides. Since the two fluids typically have different viscosities, boundary layers form in the vicinity of the interface. In this region viscous effects lead to the formation of sufficient vorticity to ensure that the continuity of tangential stress condition is met. In the DMDF model this effect is modeled by changing the source term $\boldsymbol{\omega}$ in cells containing a portion of the interface. Such cells are called irregular grid cells. Let I^* denote the set of grid nodes belonging to irregular cells (fig. 3.1). Instead of solving (3.3), the equation

$$\triangle \boldsymbol{\psi}^* = -\boldsymbol{\omega}^* \tag{3.6}$$

is solved with

$$\boldsymbol{\omega}^*(\mathbf{x}^h) = \left\{ \begin{array}{cc} \boldsymbol{\omega} & \mathbf{x}^h \notin I^* \\ \boldsymbol{\omega} + \mathbf{C} & \mathbf{x}^h \in I^* \end{array} \right. . \tag{3.7}$$

The correction term $\mathbf{C}$ may be determined from the continuity of tangential stress as shown in §3.2 for the 2D case and in §3.3 for the 3D case.

In addition to the boundary conditions imposed on the fluid stresses, mass transfer conditions may also be imposed at the interface. These are typically associated with phase change phenomena at the interface. Similarly to the above technique, a modified source term is introduced for the irregular cells

$$q^*(\mathbf{x}^h) = \left\{ \begin{array}{cc} q & \mathbf{x}^h \notin I^* \\ q + D & \mathbf{x}^h \in I^* \end{array} \right. . \tag{3.8}$$

and the modified scalar potential is given by

$$\triangle \phi^* = q^* . \tag{3.9}$$

Within the volume occupied by any one phase the potentials ϕ^*, $\boldsymbol{\psi}^*$ may be assumed continuous and differentiable. Knowledge of the source terms and boundary conditions allow direct evaluation of the potentials through the application of the fundamental representation formula [28, p. 63]. For example, for the scalar potential and with $P \in V_1$ this would give

$$\phi^*(P) = \frac{1}{4\pi} \int_{S_1 \cup S_2} \left(\frac{1}{r} \frac{\partial \phi^*(M)}{\partial n} - \phi^*(M) \frac{\partial (1/r)}{\partial n} \right) dS - \frac{1}{4\pi} \int_{V_1} \frac{q^*(M)}{r} dV , \tag{3.10}$$

where $r = |\mathbf{r}| = |\mathbf{PM}|$. Evaluation of the volume integral is computationally costly however. It is more convenient to split the potentials into two parts

$$\boldsymbol{\psi}^* = \boldsymbol{\psi}^\omega + \boldsymbol{\psi}^S , \tag{3.11}$$

$$\phi^* = \phi^q + \phi^S , \tag{3.12}$$

with

$$\triangle \boldsymbol{\psi}^\omega = -\boldsymbol{\omega}^*, \quad \triangle \boldsymbol{\psi}^S = 0 \tag{3.13}$$

$$\triangle \phi^q = q^*, \quad \triangle \phi^S = 0 . \tag{3.14}$$

The values of ϕ^q, $\boldsymbol{\psi}^\omega$ at the grid points $\mathbf{x}^h$ may be efficiently computed by applying a fast Poisson solver on $V_1 \cup S_2 \cup V_2$ with some conveniently simple boundary conditions. Discontinuities arising in the discrete Laplace operator may be taken into account by adapting the procedures pioneered in [26]. Once $\phi^q(\mathbf{x}^h)$, $\boldsymbol{\psi}^\omega(\mathbf{x}^h)$ are known, interpolation procedures that include any discontinuities associated with the presence of the interface may be used to compute $\phi^q(\mathbf{x})$, $\boldsymbol{\psi}^\omega(\mathbf{x})$ and their derivatives for $\mathbf{x} \in S_2$. These values enter into the boundary problems for ϕ^S and $\boldsymbol{\psi}^S$ which are solved by setting up appropriate integral equations along the bubble. In the decompositions (3.11-3.12) ϕ^q, $\boldsymbol{\psi}^\omega$ have the role of modeling the subgrid interface effects while ϕ^S and $\boldsymbol{\psi}^S$ ensure that S_2 is either a streamline when there is no mass flow through the interface or S_2 is a surface with prescribed mass flow.

3.1.3 Subgrid-scale effects given by the DMDF model

After carrying out the above computations a new velocity field

$$\mathbf{U}^* = \nabla \phi^* + \nabla \times \boldsymbol{\psi}^*, \tag{3.15}$$

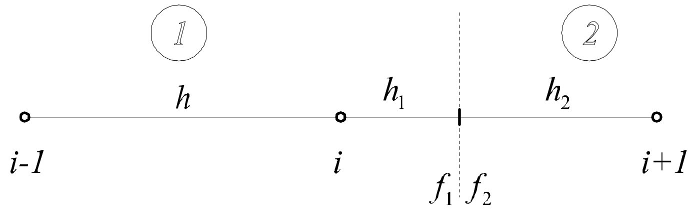

Figure 3.2: The one-dimensional irregular stencil.

that includes the physical effects of the bubble interface at the subgrid scale, may be computed. However, the $\mathbf{U}^*$ field is not directly required in evaluating the momentum drift-flux term (1.5). In the MDF term $\mathbf{D}$, the phase-averaged quantities $\langle \mathbf{U}_1 \rangle_1$, $\langle \mathbf{U}_2 \rangle_2$ appear. These involve an integration over the volume occupied by each phase in an irregular grid cell G^*,

$$\langle \mathbf{U}_k \rangle_k = \frac{1}{V_k} \int_{V_k \cap G^*} (\nabla \phi^* + \nabla \times \boldsymbol{\psi}^*)\, dV \,. \tag{3.16}$$

Using the divergence and curl theorems [46, Chap. IV] the above volume integrals may be conveniently transformed to surface integrals so ϕ^* and $\boldsymbol{\psi}^*$ appear directly

$$\langle \mathbf{U}_k \rangle_k = \frac{1}{V_k} \int_{\partial(V_k \cap G^*)} (\phi^* \mathbf{n} + \mathbf{n} \times \boldsymbol{\psi}^*)\, dS \,. \tag{3.17}$$

Equation (3.17) shows how naturally the subgrid, phase-averaged velocity is expressed in terms of the scalar and vector potentials introduced in (3.2).

The corrected velocity field $\mathbf{U}^*$ is largely determined by the initial velocity field $\mathbf{U}^h$ furnished by the VOF computation, since $\mathbf{U}^h$ is used to determine the source terms q^*, $\boldsymbol{\omega}^*$ in the regular grid cells. Of course, it is not identical to the $\mathbf{U}^h$ field since subgrid scale interface effects have been added. The influence of these effects is transmitted to the VOF computation by way of the drift-flux term.

3.1.4 Finite difference approximation of derivatives functions with discontinuities

The computational efficiency of the DMDF model is based upon the possibility of using fast Poisson solvers over rectangular domains which contain the bubble interface. The interface is modeled by a singularity distribution which induces jumps in the function satisfying the Poisson equation. These jumps are derived from physical conditions. The Poisson equation right hand side term is modified in order to account for the known jumps. The required corrections may be built up from a series of one-dimensional problems. We now derive the required 1D formula that accounts for the known jumps. This formula may be applied along each the spatial directions of a 2D or 3D Poisson solver.

Consider a function $f(x)$ which has a discontinuous second derivative at $x = x_i + h_1$. The jump in the derivative is $[f''] = f_2'' - f_1''$. The standard finite difference formula

$$f_i'' \cong (f_{i+1} - 2f_i + f_{i-1})/h^2 \tag{3.18}$$

is not an $O(h^2)$ approximation of the second derivative because of the discontinuity at $x_i + h_1$. Denote by the index 1 the values of the function and its derivatives to the left of $x_i + h_1$ and by index 2 those to the right (fig. 3.2). The following series expansions are valid

$$f_{i+1} = f_2 + h_2 f_2' + \tfrac{1}{2} h_2^2 f_2'' + \tfrac{1}{6} h_2^3 f_2''' + \tfrac{1}{24} h_2^4 f_2^{(iv)} \dots \tag{3.19}$$

$$f_1 = f_i + h_1 f_i' + \tfrac{1}{2} h_1^2 f_i'' + \tfrac{1}{6} h_1^3 f_i''' + \tfrac{1}{24} h_1^4 f_i^{(iv)} + \dots \tag{3.20}$$

$$f_1' = f_i' + h_1 f_i'' + \tfrac{1}{2} h_1^2 f_i''' + \tfrac{1}{6} h_1^3 f_i^{(iv)} + \dots \tag{3.21}$$

$$f_1'' = f_i'' + h_1 f_i''' + \tfrac{1}{2} h_1^2 f_i^{(iv)} + \dots \tag{3.22}$$

$$f_{i-1} = f_i - h f_i' + \tfrac{1}{2} h^2 f_i'' - \tfrac{1}{6} h^3 f_i''' + \tfrac{1}{24} h^4 f_i^{(iv)} + \dots \quad . \tag{3.23}$$

The jump conditions may be introduced by

$$f_2 = f_2 - f_1 + f_1 = [f] + f_1 \tag{3.24}$$

and similar relations for the derivatives. Evaluation of (3.18) gives

$$(f_{i+1} - 2f_i + f_{i-1}) = [f] + h_2 [f'] + \tfrac{1}{2} h_2^2 [f''] + \tfrac{1}{6} h_2^3 [f'''] + \dots \tag{3.25}$$

$$+ h^2 f_i'' + \tfrac{1}{12} h^4 f_i^{(iv)} + \dots \quad . \tag{3.26}$$

The resulting $O(h^2)$ accurate approximation of the second derivative is

$$f_i'' = (f_{i+1} - 2f_i + f_{i-1})/h^2 - \tag{3.27}$$

$$[f]/h^2 - [f'](h_2/h^2) - \tfrac{1}{2} [f''] (h_2/h)^2 - \tfrac{1}{6} [f'''] (h_2^3/h^2) + O(h^2). \tag{3.28}$$

3.2 The 2D Case

The details of the 2D DMDF model are now presented. The procedure is simpler in two dimensions since the vector potential and the vorticity have only one component $\boldsymbol{\omega} = \omega \mathbf{k}$, $\boldsymbol{\psi} = \psi \mathbf{k}$, so (3.3) becomes a scalar Poisson equation

$$\triangle \psi = -\omega \, . \tag{3.29}$$

The vector potential reduces to the standard stream function. The notation $(\mathbf{i}, \mathbf{j}, \mathbf{k})$ is used for the Cartesian unit vectors.

3.2.1 The stream function problems

Recall that the modified stream function is to be determined in two steps using the decomposition

$$\psi^* = \psi^\omega + \psi^S \,. \tag{3.30}$$

Boundary value problems for the two components are now derived. The additional vorticity generated by the boundary condition of continuity of tangential stress shall be captured in the ψ^ω term. The ψ^S correction shall ensure that the interface is a streamline at the subgrid-scale level. The DMDF model may be applied in two ways:

1. compute both ψ^ω and ψ^S and set $\psi^* = \psi^\omega + \psi^S$
2. compute only ψ^ω and set $\psi^* \cong \psi^\omega$

The first procedure is more accurate but shall be shown to require the solution of an additional integral equation on the bubble surface. The second procedure avoids the necessity of solving an integral equation at the price of not imposing the bubble surface to be a streamline at the subgrid scale level. The second procedure is typically acceptable from the viewpoint of the overall VOF computation. In the VOF computation the velocities and void fractions are defined upon a Cartesian grid. The bubble surface is reconstructed through some procedure. Usually, the procedure is not of very high order so that computational time may be kept within acceptable levels. Typically a first order bubble reconstruction procedure is used [39]. It is, therefore, counterproductive to insist that an inaccurately determined interface be a streamline, since the additional computational expense is significant even in 2D.

Tangential stress boundary condition

The continuity of tangential stress may be stated as

$$\mu_1 \left. \frac{\partial U_{t1}}{\partial n} \right|_{S_2^+} = \mu_2 \left. \frac{\partial U_{t2}}{\partial n} \right|_{S_2^-} \tag{3.31}$$

for $\mathbf{x} \in S_2$, with

$$\mathbf{U} = U_t \mathbf{t} + U_n \mathbf{n} \; = u\mathbf{i} + v\mathbf{j}, \tag{3.32}$$

and $\mathbf{t}$, $\mathbf{n}$ the unit tangent and normal vectors to S_2,

$$\mathbf{t} = t_x \mathbf{i} + t_y \mathbf{j}, \quad \mathbf{n} = n_x \mathbf{i} + n_y \mathbf{j} = -t_y \mathbf{i} + t_x \mathbf{j} \,. \tag{3.33}$$

S_2^- refers to the limit reached from fluid 2 in volume V_2, S_2^+ that reached from fluid 1 in volume V_1. The normal is assumed to point outward from the bubble fluid 2 into the surrounding fluid 1 (fig. 3.1).

Condition (3.31) is assumed to be satisfied over a computational cell G on average

$$\int_{V_1\cap G} \mu_1 \left.\frac{\partial U_{t1}}{\partial n}\right|_{S_2^+} dV = \int_{V_2\cap G} \mu_2 \left.\frac{\partial U_{t2}}{\partial n}\right|_{S_2^-} dV\,. \tag{3.34}$$

This is typically achieved in the overall VOF computation by adding an appropriate volume force term $\mathbf{f}^{ext}$ in (1.2).

Using the decomposition (3.2),

$$\begin{aligned} U_t &= (u^\phi + u^\psi)t_x + (v^\phi + v^\psi)t_y = \left(\frac{\partial\phi}{\partial x} + \frac{\partial\psi}{\partial y}\right)t_x + \left(\frac{\partial\phi}{\partial y} - \frac{\partial\psi}{\partial x}\right)t_y \\ &= \frac{\partial\phi}{\partial t} + \left(\frac{\partial\psi}{\partial y}t_x - \frac{\partial\psi}{\partial x}t_y\right) = \frac{\partial\phi}{\partial t} + \left(\frac{\partial\psi}{\partial y}n_y + \frac{\partial\psi}{\partial x}n_x\right) \\ &= \frac{\partial\phi}{\partial t} + \frac{\partial\psi}{\partial n}\,. \end{aligned}$$

The normal derivative of the tangential velocity is therefore

$$\frac{\partial U_t}{\partial n} = \frac{\partial^2\phi}{\partial n\partial t} + \frac{\partial^2\psi}{\partial n^2}\,. \tag{3.35}$$

Since the bubble is a streamline,

$$\mathbf{U}\cdot\mathbf{n} = (\mathbf{U}^\phi + \mathbf{U}^\psi)\cdot\mathbf{n} = U_n^\phi + U_n^\psi = 0\,. \tag{3.36}$$

If the condition

$$\psi_{S_2} = 0 \tag{3.37}$$

is imposed then $U_n^\phi = U_n^\psi = 0$. Condition (3.37) implies

$$\frac{\partial^2\phi}{\partial n\partial t} = \frac{\partial^2\phi}{\partial t\partial n} = \frac{\partial U_n^\phi}{\partial t} = 0 \tag{3.38}$$

so that (3.35) becomes

$$\frac{\partial U_t}{\partial n} = \frac{\partial^2\psi}{\partial n^2} \tag{3.39}$$

for $\mathbf{x}\in S_2$. The continuity of tangential stress (3.31) may be written as

$$\mu_1 \left.\frac{\partial^2\psi}{\partial n^2}\right|_{S_2^+} = \mu_2 \left.\frac{\partial^2\psi}{\partial n^2}\right|_{S_2^-}\,. \tag{3.40}$$

Assume that (n,t) form a natural coordinate system, i.e. coordinate differences equal arc lengths. Then (3.29) becomes

$$\frac{\partial^2\psi}{\partial t^2} + \frac{\partial^2\psi}{\partial n^2} = -\omega \tag{3.41}$$

in the (n, t) coordinate system. The velocity decomposition (3.2) is assumed to hold throughout the bounding box enclosed by S_1. On S_2 one has $\psi_{S_2} = 0$ and, therefore, all tangential derivatives are also zero. Applying (3.41) on S_2 would give

$$\left.\frac{\partial^2 \psi}{\partial n^2}\right|_{S_2} = -\omega_{S_2} \,. \tag{3.42}$$

Because of (3.40) a discontinuity in the second normal derivative of the stream function appears, such that

$$\left.\frac{\partial^2 \psi}{\partial n^2}\right|_{S_2^+} = -\omega_1, \quad \left.\frac{\partial^2 \psi}{\partial n^2}\right|_{S_2^-} = -\omega_2 \,. \tag{3.43}$$

Applying (3.40) the simple condition

$$\mu_1 \omega_1 = \mu_2 \omega_2 \tag{3.44}$$

is obtained. Equation (3.42) would be valid if there were no singularity, that is if the interface were disregarded. This is exactly the assumption in the underlying VOF computation. The vorticity value ω_{VOF} given by the VOF computation at a point on S_2 may thus be seen as the average value of the vorticities on the two sides of the interface

$$\omega_1 + \omega_2 = 2\omega_{VOF} \,. \tag{3.45}$$

The values

$$\omega_1 = \frac{2\mu_2}{\mu_1 + \mu_2}\omega_{VOF}, \quad \omega_2 = \frac{2\mu_1}{\mu_1 + \mu_2}\omega_{VOF} \tag{3.46}$$

result immediately and the jump in vorticity at the interface may be evaluated as

$$[\omega] = \omega_1 - \omega_2 = 2\frac{\mu_2 - \mu_1}{\mu_1 + \mu_2}\omega_{VOF} \,. \tag{3.47}$$

The conclusion is that the continuity of tangential stress across the interface leads to a discontinuity in $\partial^2\psi/\partial n^2$ of known magnitude,

$$\left[\frac{\partial^2 \psi}{\partial n^2}\right] = \left.\frac{\partial^2 \psi}{\partial n^2}\right|_{S_2^+} - \left.\frac{\partial^2 \psi}{\partial n^2}\right|_{S_2^-} = -\,[\omega] \,. \tag{3.48}$$

The effect of this discontinuity appears only in the rhs term and thus only affects ψ^ω.

Modified Poisson equation for ψ^ω

Having determined the effect of the tangential stress boundary condition, the corrections C that arise in $\omega^* = \omega + C$ are now evaluated. We wish to apply a fast Poisson solver to the inhomogeneous problem

$$\left\{ \begin{array}{ll} \triangle\psi^\omega = -\omega^* & \mathbf{x} \in V_1 \cup S_2 \cup V_2 \\ \psi^\omega = 0 & \mathbf{x} \in S_1 \end{array} \right. . \tag{3.49}$$

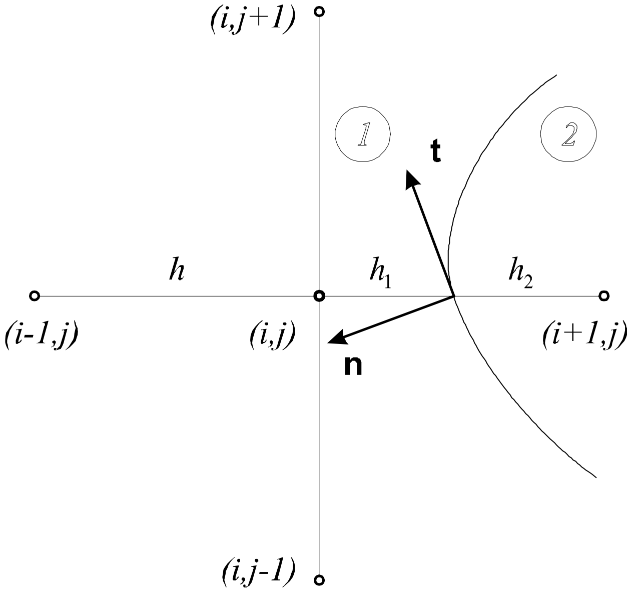

Figure 3.3: The discrete Laplace stencil for an irregular node.

As noted by Mayo [26], for an irregular cell the standard 5-point stencil formula

$$\triangle\psi^{\omega}_{ij} \cong (\psi^{\omega}_{i+1,j} + \psi^{\omega}_{i,j+1} + \psi^{\omega}_{i,j-1} + \psi^{\omega}_{i,j+1} - 4\psi^{\omega}_{ij})/h^2 = \triangle_h \psi^{\omega}_{ij} \tag{3.50}$$

does not furnish a $O(h^2)$ truncation error due to the discontinuities in $\partial^2\psi^{\omega}/\partial n^2$. If the magnitude of the discontinuity is known, then the correction required to restore $O(h^2)$ truncation error may be evaluated. This turns out to be a modification of the rhs term, $\omega^* = \omega + C$.

Discrete Laplace operator for irregular cells

The one-dimensional result (3.27) may be directly applied in evaluating a second order approximation of the Laplace operator for cells with discontinuities. Consider an interface that intersects the (i,j) to $(i+1,j)$ branch of the standard 5-point discrete Laplace stencil (fig. 3.3). The discontinuity in $\partial^2\psi^{\omega}/\partial n^2$ may be decomposed along the Cartesian axes

$$\left[\frac{\partial^2\psi^{\omega}}{\partial x^2}\right] = \left[\frac{\partial^2\psi^{\omega}}{\partial n^2}\right] n_x, \quad \left[\frac{\partial^2\psi^{\omega}}{\partial y^2}\right] = \left[\frac{\partial^2\psi^{\omega}}{\partial n^2}\right] n_y\,. \tag{3.51}$$

Applying the same series expansion procedures,

$$\triangle\psi^{\omega}_{ij} \cong \frac{\psi^{\omega}_{i+1,j} + \psi^{\omega}_{i,j+1} + \psi^{\omega}_{i,j-1} + \psi^{\omega}_{i,j+1} - 4\psi^{\omega}_{ij}}{h^2} - \frac{1}{2}\left[\frac{\partial^2\psi^{\omega}}{\partial x^2}\right]\left(\frac{h_2}{h}\right)^2 \tag{3.52}$$

is obtained. The correction to the vorticity is

$$C_{ij} = \frac{1}{2}\left[\frac{\partial^2\psi^{\omega}}{\partial x^2}\right]\left(\frac{h_2}{h}\right)^2\,. \tag{3.53}$$

Similar formulas may be written for the cases where the interface intersects other segments of the stencil. The ω^* term may now be computed, and the solution to (3.49) determined using a fast Poisson solver.

The homogeneous stream function problem

The ψ^S component of the stream function is now determined. The required conditions on ψ^S are

$$\left\{ \begin{array}{ll} \triangle\psi^S = 0 & \mathbf{x} \in V_1 \cup S_2 \cup V_2 \\ \psi^S = -\psi^\omega \equiv f & \mathbf{x} \in S_2 \end{array} \right. \tag{3.54}$$

Note that the boundary condition on ψ^S in the above problem is such that the combined stream function

$$\psi^* = \psi^S + \psi^\omega = 0 \quad \text{on } S_2 \tag{3.55}$$

i.e., the bubble surface S_2 is a streamline. The values of ψ^ω for $\mathbf{x} \in S_2$ are interpolated from the grid node values using third-order accurate formulas that take into account the jump in the second derivatives. The solution to (3.54) is represented as a distribution of a double layer potential $\mu(\mathbf{y})$ on S_2

$$\psi^S(\mathbf{x}) = \frac{1}{2\pi} \int_{S_2} \mu(\mathbf{y}) \frac{\partial}{\partial n} \log|\mathbf{y} - \mathbf{x}| \; d\mathbf{y} \,. \tag{3.56}$$

From general potential theory [18],

$$\lim_{\alpha \searrow 0} \psi^S(\mathbf{y} + \alpha\mathbf{n}) = \frac{1}{2\pi} \int_{S_1} \mu(\mathbf{y}) \frac{\partial}{\partial n} \log|\mathbf{y} - \mathbf{x}| \; d\mathbf{y} + \frac{1}{2}\mu(\mathbf{y}) \tag{3.57}$$

$$\lim_{\alpha \nearrow 0} \psi^S(\mathbf{y} + \alpha\mathbf{n}) = \frac{1}{2\pi} \int_{S_1} \mu(\mathbf{y}) \frac{\partial}{\partial n} \log|\mathbf{y} - \mathbf{x}| \; d\mathbf{y} - \frac{1}{2}\mu(\mathbf{y}) \tag{3.58}$$

with $\mathbf{y} \in S_1$. The above Plemelj formulas imply that we must seek a two branch representation of ψ^S

$$\psi^S(\mathbf{x}) = \left\{ \begin{array}{ll} \frac{1}{2\pi} \int_{S_1} \mu^+(\mathbf{y}) \frac{\partial}{\partial n} \log|\mathbf{y} - \mathbf{x}| \; d\mathbf{y} & \mathbf{x} \in V_1 \\ \frac{1}{2\pi} \int_{S_1} \mu^-(\mathbf{y}) \frac{\partial}{\partial n} \log|\mathbf{y} - \mathbf{x}| \; d\mathbf{y} & \mathbf{x} \in V_2 \end{array} \right. . \tag{3.59}$$

The required double-layer potentials are determined by solving the integral equations

$$\int_{S_1} \mu^+(\mathbf{y}) \frac{\partial}{\partial n} \log|\mathbf{y} - \mathbf{x}| \; d\mathbf{y} + \pi\mu^+(\mathbf{y}) = 2\pi f(\mathbf{y}) \tag{3.60}$$

$$\int_{S_1} \mu^-(\mathbf{y}) \frac{\partial}{\partial n} \log|\mathbf{y} - \mathbf{x}| \; d\mathbf{y} - \pi\mu^-(\mathbf{y}) = 2\pi f(\mathbf{y}) \,. \tag{3.61}$$

These equations have a nonsingular kernel since

$$\lim_{\mathbf{x}\to\mathbf{y}} \frac{\partial}{\partial n} \log|\mathbf{y}-\mathbf{x}| = -\frac{\mathcal{H}(\mathbf{y})}{2} \tag{3.62}$$

where $\mathcal{H}(\mathbf{y})$ is the local curvature, which is smooth for smooth bubbles. The integral equations (3.60) and (3.61) are solved using a Nyström method [12]. The discretization nodes for the Nyström procedure are the intersections of the bubble with the VOF Cartesian grid. Denote this set by I_1.

Once μ^+, μ^- are determined $\psi^S(\mathbf{x})$ and its derivatives may be determined from (3.59) for all $\mathbf{x} \in I_1$ and irregular grid nodes $\mathbf{x} \in I^*$. If M is the number of nodes in I_1 the evaluation of (3.59) costs $O(M)$ operations so the total computational effort for applying (3.59) is $O(3M^2)$ since, on average, for every $\mathbf{x} \in I_1$ there are two irregular grid nodes. The alternative to applying (3.59) directly is to apply a fast Laplace solver. In this case one would solve

$$\begin{cases} \triangle\psi^S = 0 & \mathbf{x} \in V_1 \\ \psi^S = f_2 & \mathbf{x} \in S_2 \end{cases} \tag{3.63}$$

for the bubble exterior with the f_2 along S_2 given by applying (3.59). One would need to solve a separate problem for the bubble interior. Since in the DMDF method we are only interested in evaluating ψ^S at comparatively few points, those in the irregular grid cells, the direct application of (3.59) is usually preferable.

3.2.2 The scalar potential problems

The two components of the scalar potential decomposition $\phi^* = \phi^q + \phi^S$ are now determined. The procedure is similar to that adopted for the stream function. The modified source term q^* models the overall effects of mass flow through the interface. The ϕ^S term shall ensure that the mass flow is of the prescribed velocity.

Mass flow boundary condition

The Poisson equation to find ϕ^q is

$$\begin{cases} \triangle\phi^q = q^* & \mathbf{x} \in V_1 \cup S_2 \cup V_2 \\ \phi^q = 0 & \mathbf{x} \in S_1 \end{cases} . \tag{3.64}$$

A mass flow through the interface may exist as a result of phase transition phenomena. The mass conservation condition at the interface is

$$\dot{m}_1 = \dot{m}_2 , \tag{3.65}$$

i.e., the mass flow of the condensing vapor must equal that of the resulting liquid. Equation (3.65) implies

$$\rho_1 v_1 = \rho_2 v_2 . \tag{3.66}$$

But, at the interface

$$v_1 = \left.\frac{\partial \phi}{\partial n}\right|_{S_2^+}, \quad v_2 = \left.\frac{\partial \phi}{\partial n}\right|_{S_2^-} \tag{3.67}$$

and we obtain

$$\rho_1 \left.\frac{\partial \phi}{\partial n}\right|_{S_2^+} = \rho_2 \left.\frac{\partial \phi}{\partial n}\right|_{S_2^-}. \tag{3.68}$$

This equation is the analog of (3.40). The VOF method furnishes a value for the normal derivative of ϕ in which jump effects are not accounted for. Similarly to the procedure for the stream function, we assume that the VOF procedure gives an average value

$$\left.\frac{\partial \phi}{\partial n}\right|_{VOF} = \frac{1}{2}\left(\left.\frac{\partial \phi}{\partial n}\right|_{S_2^+} + \left.\frac{\partial \phi}{\partial n}\right|_{S_2^-} \right). \tag{3.69}$$

We are therefore able to compute the jump in the normal derivative of ϕ

$$\left[\frac{\partial \phi}{\partial n}\right] = 2\frac{\rho_2 - \rho_1}{\rho_1 + \rho_2} \left.\frac{\partial \phi}{\partial n}\right|_{VOF}. \tag{3.70}$$

The source term from the VOF computation q is modified to account for the jump of known magnitude in $\partial\phi/\partial n$. For instance, if the interface intersects the (i, j) to $(i+1, j)$ branch of the Laplace stencil the (i, j) second order approximation of the Poisson equation is

$$\frac{\phi^q_{i+1,j} + \phi^q_{i,j+1} + \phi^q_{i,j-1} + \phi^q_{i,j+1} - \phi^q_{ij}}{h^2} = q_{ij} + \left[\frac{\partial \phi^q}{\partial x}\right] \frac{h_2}{h^2} \tag{3.71}$$

with

$$\left[\frac{\partial \phi^q}{\partial x}\right] = \left[\frac{\partial \phi}{\partial n}\right] n_x \,. \tag{3.72}$$

The homogeneous scalar potential problem

It is sometimes the case that the normal velocities v_{S_2} at the interface are prescribed. This usually is the result of including a specific phase transition model for the interface. The combined effect of the q source term from the VOF computation and the correction imposed by the continuity of mass flow condition (3.65) is such that the normal velocity at the interface is not that prescribed by the phase transition model. An additional correction ϕ^S may be computed in order to recover the prescribed normal velocity v_{S_2} by solving

$$\left\{ \begin{array}{cc} \triangle \phi^S = 0 & \mathbf{x} \in V_1 \cup S_2 \cup V_2 \\ \dfrac{\partial \phi^S}{\partial n} = v_{S_2} - \dfrac{\partial \phi^q}{\partial n} - v^{\psi} \equiv g & \mathbf{x} \in S_2 \end{array} \right. . \tag{3.73}$$

Again, the boundary condition is such that the total normal velocity takes on the prescribed value

$$v = \frac{\partial \phi^*}{\partial n} + \frac{\partial \psi^*}{\partial t} = v_{S_2} \tag{3.74}$$

on S_2. We now have a Neumann problem (3.73) in contrast to the analogous Dirichlet problem (3.54) encountered previously. The appropriate representation is in this case in terms of a single-layer potential

$$\phi(\mathbf{x}) = \frac{1}{2\pi} \int_{S_1} \nu(\mathbf{y}) \log |\mathbf{y} - \mathbf{x}| \; d\mathbf{y}. \tag{3.75}$$

The single-layer potential induces a jump in the normal derivative given by

$$\lim_{\alpha \searrow 0} \frac{\partial \phi(\mathbf{y} + \alpha \mathbf{n})}{\partial n} = \frac{1}{2\pi} \int_{S_1} \nu(\mathbf{y}) \log |\mathbf{y} - \mathbf{x}| \; d\mathbf{y} + \frac{1}{2} \nu(\mathbf{y}) \tag{3.76}$$

$$\lim_{\alpha \nearrow 0} \frac{\partial \phi(\mathbf{y} + \alpha \mathbf{n})}{\partial n} = \frac{1}{2\pi} \int_{S_1} \nu(\mathbf{y}) \log |\mathbf{y} - \mathbf{x}| \; d\mathbf{y} - \frac{1}{2} \nu(\mathbf{y}). \tag{3.77}$$

Again, a two-branch representation is adopted

$$\phi(\mathbf{x}) = \begin{cases} \frac{1}{2\pi} \int_{S_1} \nu^+(\mathbf{y}) \log |\mathbf{y} - \mathbf{x}| \; d\mathbf{y} & \mathbf{x} \in V_1 \\ \frac{1}{2\pi} \int_{S_1} \nu^-(\mathbf{y}) \log |\mathbf{y} - \mathbf{x}| \; d\mathbf{y} & \mathbf{x} \in V_2 \end{cases}. \tag{3.78}$$

The integral equations to be solved are

$$\int_{S_1} \nu^+(\mathbf{y}) \log |\mathbf{y} - \mathbf{x}| \; d\mathbf{y} + \pi \nu^+(\mathbf{y}) = 2\pi g(\mathbf{y}) \tag{3.79}$$

$$\int_{S_1} \nu^-(\mathbf{y}) \log |\mathbf{y} - \mathbf{x}| \; d\mathbf{y} - \pi \nu^-(\mathbf{y}) = 2\pi g(\mathbf{y}). \tag{3.80}$$

Once ν^+, ν^- are determined the convolution formula (3.78) may be applied to evaluate ϕ and its derivatives at the points of interest $\mathbf{x} \in I_1$, $\mathbf{x} \in I^*$.

3.2.3 Algorithm schematic and computational effort

The 2D DDF algorithm is presented schematically in fig. 3.4. Let N be the linear dimension of the bounding box and M the number of intersection points of the bubble with the Cartesian grid. The required computational effort is:

- $O(M)$ for computing ω^*
- $O(N^2 \log_2 N^2)$ for applying a fast Poisson solver to eq. (3.49) to compute ψ^ω
- $O(4M^3/3)$ to solve the four integral equations (3.60), (3.61), (3.79), (3.80)

- $O(6M^2)$ for applying (3.59) to compute derivatives of ψ^S thus giving $\mathbf{U}^\omega$
- $O(6M^2)$ for applying (3.78) to compute derivatives of ϕ thus giving $\mathbf{U}^\phi$
- $O(5M)$ for evaluating $\langle \mathbf{U}_1 \rangle_1$, $\langle \mathbf{U}_2 \rangle_2$

The total cost is thus $O(4M^3/3+12M^2+N^2\log_2 N^2)$. Typically $16 \leq M, N \leq 32$ so the cost is on the order of 10 to 62 KFLOPs for each bubble.

3.3 The 3D Case

The three-dimensional algorithm follows the same general procedures as for the 2D model. There are two additional difficulties though:

1. the rotational part of the flow is now represented by a vector potential $\boldsymbol{\psi}$ so we shall require the solution of 3 Poisson equations to find each of the components of $\boldsymbol{\psi}$;
2. the solution of the integral equations in order to find $\boldsymbol{\psi}^S$ or ϕ^S must be carried out over a surface

The first difficulty is of manageable proportions due to the efficiency of the fast Poisson solvers. However, solving the integral equations required for $\boldsymbol{\psi}^S$ and ϕ^S is prohibitively expensive. This would require a triangulation of the surface fine enough so that fourth order accuracy of the integral equation solver is actually achieved. Since the DMDF procedure is envisaged to applied at each time step of the underlying VOF method, the computational penalty is severe. We therefore abandon the corrections given by $\boldsymbol{\psi}^S$ and ϕ^S and compute only those given by $\boldsymbol{\psi}^\omega$ and ϕ^q. This corresponds to:

1. taking into account the additional vorticity produced by the interface and the continuity of mass flow across the interface in the case of phase transitions, but
2. not imposing that the interface be a stream surface or a surface of prescribed velocity *at the subgrid scale level.*

The last emphasis is important. The underlying VOF computation furnishes an approximation of the bubble surface through the reconstruction procedure. In general the interface reconstructed from the void fraction field f is not a stream surface within a computational cell. This is an error accepted in the overall VOF computation. The role of the $\boldsymbol{\psi}^S$ and ϕ^S corrections would be to ensure that the reconstructed interface would be indeed a stream surface (or a surface of prescribed normal velocity). The computational effort for this is however too high so we revert to the approximations accepted within the VOF method in this regard. The $\boldsymbol{\psi}^\omega$ and ϕ^q corrections from the DMDF model are however included and they account for the essential effects induced by the presence of an interface that were not captured by the VOF method: generation of additional vorticity and jump in normal velocities due to phase transitions.

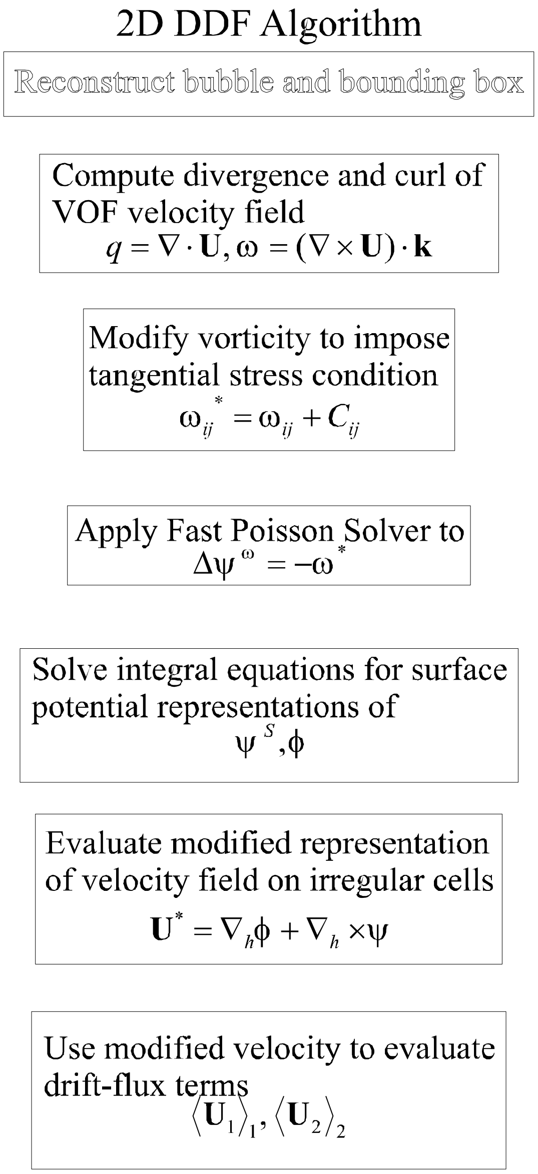

Figure 3.4: The 2D DDF algorithm.

3.3.1 The vorticity correction

The procedure is essentially similar to that from the 2D case. The only difference is that we now have a vector continuity of tangential stress condition

$$\mu_1 \left(\frac{\partial U_{t1}}{\partial n} \mathbf{t}_1 + \frac{\partial U_{t2}}{\partial n} \mathbf{t}_2 \right)_{S_2^+} = \mu_2 \left(\frac{\partial U_{t1}}{\partial n} \mathbf{t}_1 + \frac{\partial U_{t2}}{\partial n} \mathbf{t}_2 \right)_{S_2^-} . \tag{3.81}$$

The vorticity from the VOF method is

$$\boldsymbol{\omega}_{VOF} = \omega_{VOF}^{n} \mathbf{n} + \omega_{VOF}^{t1} \mathbf{t}_1 + \omega_{VOF}^{t2} \mathbf{t}_2 \,. \tag{3.82}$$

The jumps for the two tangential components of the vorticity are

$$[\omega_{t1}] = \left[\frac{\partial^2 \Psi_{t1}}{\partial n^2} \right] = 2 \frac{\mu_2 - \mu_1}{\mu_2 + \mu_1} \omega_{VOF}^{t1} \tag{3.83}$$

$$[\omega_{t2}] = \left[\frac{\partial^2 \Psi_{t2}}{\partial n^2} \right] = 2 \frac{\mu_2 - \mu_1}{\mu_2 + \mu_1} \omega_{VOF}^{t2} . \tag{3.84}$$

We compute the three components of the modified vector stream function

$$\Psi^* = \Psi^{x*} \mathbf{i} + \Psi^{y*} \mathbf{j} + \Psi^{z*} \mathbf{k}$$

by solving three Poisson equations

$$\begin{cases} \triangle \Psi^{x*} = -\omega^{x*} & \mathbf{x} \in V_1 \cup S_2 \cup V_2 \\ \dfrac{\partial \Psi^{x*}}{\partial n} = \mathbf{U} \cdot \mathbf{i} & \mathbf{x} \in S_1 \end{cases} \tag{3.85}$$

$$\begin{cases} \triangle \Psi^{y*} = -\omega^{y*} & \mathbf{x} \in V_1 \cup S_2 \cup V_2 \\ \dfrac{\partial \Psi^{y*}}{\partial n} = \mathbf{U} \cdot \mathbf{j} & \mathbf{x} \in S_1 \end{cases} \tag{3.86}$$

$$\begin{cases} \triangle \Psi^{z*} = -\omega^{z*} & \mathbf{x} \in V_1 \cup S_2 \cup V_2 \\ \dfrac{\partial \Psi^{z*}}{\partial n} = \mathbf{U} \cdot \mathbf{k} & \mathbf{x} \in S_1 \end{cases} . \tag{3.87}$$

The modified source terms are given by

$$\omega^{x*} = \omega_{VOF}^{x} + \frac{1}{h^2} \left\{ \tfrac{1}{2} \left[\Psi_{nn}^{t1} \right] \left(h_{2x}^2 \cos\theta_x^{t1} + h_{2y}^2 \cos\theta_y^{t1} + h_{2z}^2 \cos\theta_z^{t1} \right) + \right. \tag{3.88}$$

$$\left. \tfrac{1}{2} \left[\Psi_{nn}^{t2} \right] \left(h_{2x}^2 \cos\theta_x^{t2} + h_{2y}^2 \cos\theta_y^{t2} + h_{2z}^2 \cos\theta_z^{t2} \right) \right\} + O(h) \tag{3.89}$$

where $\theta_x^{t1}, \theta_y^{t1}, \theta_z^{t1}$ are the angles of the $\mathbf{t}_1$ tangential vector with respect to the $(\mathbf{i}, \mathbf{j}, \mathbf{k})$ system and $\theta_x^{t2}, \theta_y^{t2}, \theta_z^{t2}$ those of the $\mathbf{t}_2$ tangential vector. Similar relations hold for the other two components and the relation may be extended to higher order $(O(h^2))$ by including the jumps $[\Psi_{nnt}^{t1}], [\Psi_{nnn}^{t1}]$.

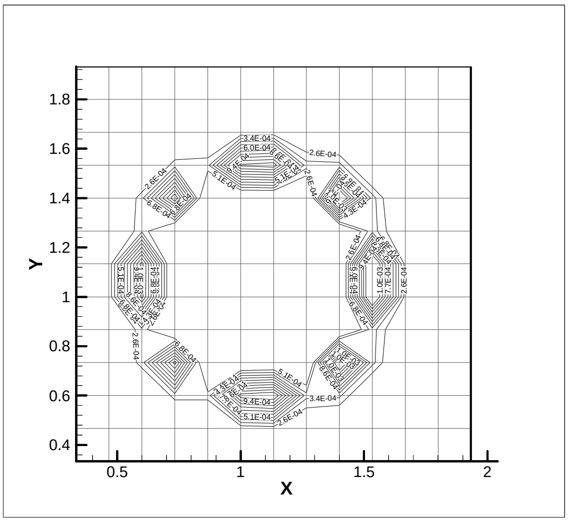

Figure 3.5: $\|\nabla \cdot \mathbf{D}\|$ from DMDF model for a $\rho_2/\rho_1 = 10^{-3}$ bubble.

3.3.2 The normal velocity correction

There is no essential difference with respect to the 2D formulation. We solve

$$\begin{cases} \triangle \phi^q = q^* & \mathbf{x} \in V_1 \cup S_2 \cup V_2 \\ \phi^q = 0 & \mathbf{x} \in S_1 \end{cases} \tag{3.90}$$

with the jump in the normal derivative given by the continuity of mass condition

$$\left[\frac{\partial \phi}{\partial n} \right] = 2 \frac{\rho_2 - \rho_1}{\rho_1 + \rho_2} \left. \frac{\partial \phi}{\partial n} \right|_{VOF} \tag{3.91}$$

Of course the Poisson problem (3.90) is now over a 3D domain.

3.4 Typical computational result

A full test of the MDF model requires the development of an underlying computational procedure (e.g. TURBIT-VOF) to provide the required turbulent velocity fields. Until this development is completed an initial verification may be made by using the viscid-inviscid model from the previous chapter. This verification is however trivial since the procedure for the computation of the velocities over Cartesian grid outlined in 2.1.6 is exactly the restriction of the DMDF model to the case of potential flow. It is, therefore, no surprise that the computed MDF term (fig. 3.5) is identical to that computed in 2.3.

3.5 Conclusions

A model for the sub-grid scale flow arising in the presence of a fluid interface has been constructed for both two- and three-dimensional bubbly flow. The model has the following characteristics:

1. It takes into account the local, turbulent flow conditions as given by the underlying bubbly flow computation (e.g. VOF method). This may be contrasted with the previous viscid-inviscid model in which laminar conditions had to be imposed on the box surrounding the bubble.

2. It imposes physical corrections on the underlying velocity field that account for the tangential stress boundary condition and the stream surface condition at the interface.

The most attractive feature of the model is that it dynamically adapts to the local flow conditions. This is important in the context of numerical simulation of turbulent bubbly flow in which considerable effort is expended to ensure a good representation of turbulent effects away from the interfaces. The accuracy of this information would be wasted if simplified subgrid scale models were applied. The DMDF model adds the minimal corrections to the turbulent velocity field that take into account the physical effects of a fluid interface.

The DMDF model may be applied in one of two ways:

1. disregarding the condition that the bubble interface must be an stream surface;

2. imposing the condition that the bubble interface must be an stream surface.

It is suggested that the first method is sufficiently accurate for the purposes of the overall VOF computation. It accounts for the most important effect of interest in the computation of turbulent bubbly flow, namely the generation of additional vorticity due to the boundary conditions on the bubble interface. The second method requires the triangulation of the bubble surface and the solution of an integral equation on this surface. This leads to an unacceptably large time penalty for the overall VOF computation since the DMDF model is envisaged as being applied at each time step of the computation for each of the bubbles.

Part II

Turbulent Subgrid Stress Closures

Chapter 4

Problem formulation and overview of research

The second closure problem arising in a computation of a bubbly flow using a large eddy simulation method studied in this report is that of deriving an appropriate subgrid scale turbulence model. Recall the center of mass momentum transport equation

$$\frac{\partial}{\partial t}\rho\mathbf{U} + \nabla \cdot (\rho\mathbf{U} \otimes \mathbf{U}) = -\nabla p + \nabla \cdot \boldsymbol{\tau} + \mathbf{f}^{ext} + \sum \mathbf{B}_k + \mathbf{m}_{int}^{\sigma} - \nabla \cdot \mathbf{D} \,. \tag{4.1}$$

In the derivation of this equation a spatial averaging operation was carried out so the $\rho, p, \mathbf{U}$ fields are spatial averages. Let the velocity, pressure, density fluctuations be denoted by $\rho', p', \mathbf{U}'$. The effect of these fluctuations upon the averaged fields is captured by the $\mathbf{B}_k$ term [2]

$$\mathbf{B}_k = \nabla \cdot \langle \boldsymbol{\tau}_k' \rangle + \nabla \cdot \langle \boldsymbol{\tau}_k^{u\prime} \rangle - \frac{\partial}{\partial t} \langle \rho_k' \mathbf{U}_k' \rangle - \tag{4.2}$$

$$\nabla \cdot \left(\langle \rho_k \rangle_k \langle \mathbf{U}_k' \otimes \mathbf{U}_k' \rangle + 2 \langle \mathbf{U}_k \rangle_k \otimes \langle \rho_k' \mathbf{U}_k' \rangle + \left\langle \rho_k' \mathbf{U}_k' \otimes \mathbf{U}_k' \right\rangle \right) . \tag{4.3}$$

The most difficult step in evaluating $\mathbf{B}_k$ is modeling $\langle \mathbf{U}_k' \otimes \mathbf{U}_k' \rangle$, the second moment of the velocity fluctuations. For single phase flow there exist quite a number of procedures to compute this subgrid stress (SGS) term. The most successful is probably the dynamic SGS model devised by Germano [11]. For bubbly flow the question that arises is how to account for unresolved bubbles. The interaction between these bubbles and between the bubbles and the turbulent velocity field are not well known at this time. There have been a number of qualitative experimental observations [23], [45] that show that the turbulence of the continuous phase is strongly modified by the presence of a dispersed phase, even for very small void fractions. The additional fluctuations that are observed have been tentatively classified into “true turbulence” and “pseudo turbulence”. The second term refers to the additional fluctuations associated with the bubbles motion, which enhance overall momentum transport but do not give rise to an entire spectrum of fluctuations through the well-established cascade mechanism of true turbulence.

The theoretical identification of which effects should be classified as "true turbulence" and which as "pseudo turbulence" is lacking at present. Also the mechanism by which the turbulence of the liquid phase is affected by the motion of the dispersed phase is not well understood. In this research a rational explanation of these effects is proposed for dilute bubbly flow. The viewpoint taken here is that:

1. The turbulence within the gas phase may be considered to have negligible effect upon the overall flow. Only the turbulence in the liquid phase is of interest due to the large density differential between the two phases.

2. The essential effects of the bubbles upon the liquid turbulence are:

    (a) volume displacement of the liquid;

    (b) excitation of turbulent wavemodes associated with bubble oscillation modes;

    (c) filtering of the turbulent energy transfer in Fourier space due to collective behavior of bubble clusters.

The first point may be taken as a working hypothesis for this research. Some discussion of the second point is warranted though. We have seen in the first part of this report that the potential flow approximation furnishes a good description of the flow of a liquid around a gas bubble. Moreover, the viscid corrections required for satisfying the continuity of tangential stress boundary condition have been seen to be small. Thus, the additional vorticity generated by the presence of the bubbles is hypothesized to be small in relation to the vorticity induced by the large scales of motion. The question that then naturally arises is why there should be a marked change in the behavior of turbulence when bubbles are present? The viewpoint taken here is that while the bubbles *do not* generate significant amounts of vorticity in themselves, they *do* modify the turbulent cascade mechanism of the liquid phase. Admittedly this picture of dilute bubbly flow is not universal. Duineveld [9] has studied the approximate ranges of Weber number in which such a hypothesis might be valid. The main interest here is not on the description of the properties of the mixture of bubbles and liquid in itself but rather in identifying the procedures by which physical knowledge about this mixture might be used to construct turbulence models for bubbly flow.

In this viewpoint, the viscid effects on a bubble's boundary are of secondary interest. The main effect is conjectured to be potential in nature, namely the modification of the liquid pressure field due to the presence and motion of the bubbles. In pursuing this viewpoint it is therefore appropriate to introduce a potential model for the motion of the bubbles and investigate the consequences of such a representation for the liquid motion. For the dilute bubbly flow regime it is natural to consider that the bubbles form, collectively, a weakly interacting gas. The interactions between bubbles are potential in nature. The appropriate physical techniques for studying particles interacting by means of a potential are those of statistical thermodynamics. This is the approach taken here. Contrary to the statistical thermodynamics of other systems of particles (i.e. electrons, molecules) the potential interaction between bubbles is not of constant intensity since it reflects locally changing flow conditions. However, some first order variations may be considered from which to start the analysis. The most interesting consequence of this viewpoint is that the turbulent fluctuations of the fluid may be identified as a system temperature for the bubbles. This provides a means of linking the statistical thermodynamic treatment of the bubbles with the liquid turbulence. In particular, one may apply the standard techniques used in kinetic theory [5], [19], [37] to study the physical behavior of systems of particles which interact through the means of a known potential. The standard Chapman-Enskog expansion then furnishes an expression for the apparent viscosity, interpreted here as an overall intensity of interaction between the liquid and dispersed phase.

Once a mechanism for the interaction of the bubble motion with the liquid turbulence is identified, a turbulence model may be derived. This may be accomplished by a variety of means including heuristic reasoning, analogy with gas kinetics or theoretical field methods. The last approach is adopted here, mainly because it is more rational in nature and thus allows the verification of the initial hypotheses of this model, free from any heuristic uncertainty. The technique that is adopted is that of the renormalization group. This technique has been used to derive constants for a number of widely used turbulence models [48] that are close to those derived from experimental correlations. It is assumed in the research presented here that the technique is appropriate for isolating the effect of groups of differently sized bubbles on the overall flow. The renormalization group is used both to derive an overall model and an SGS model.

In order to test the models derived in this work a model computational problem is defined and its solution attempted. The problem consists of a periodic bubble array interacting with a liquid in which the turbulence is produced by forcing at low wave numbers. The progress achieved in solving this problem is presented in §7. Some proposals regarding relevant experimental verifications are also made.

Chapter 5

Statistical Thermodynamics of Ideal Bubbly Flow

5.1 Motivation

Experimental observations [44], [20], [21], [9] have shown that well separated bubbles interact in a fashion reminiscent of particle interactions (e.g., molecules interacting through electric fields). Domains of the flow parameters (mainly the Weber number) have been observed [9] in which bubble coalescence is reduced so individual particles maintain their identity. The interaction between the particles is hydrodynamic in nature and very well approximated by the potential interaction, i.e. viscous effects play only a small role in these interactions. This observation suggests that the methods of kinetic theory and statistical thermodynamics may furnish insights in to the behavior of dilute bubbly flow. The intuitive reasoning is that there exists an analogy with the situation typically encountered in molecular dynamics (fig. 5.1). From kinetic theory and statistical thermodynamics we know [5], [19] that global properties of the ensemble of particles may be obtained. Significant examples include the estimates of viscosity available from kinetic theory or the prediction of cooperative behavior which may be obtained from statistical thermodynamics. The investigation of the analogous quantities for bubbly flow presents some interest. Since the hydrodynamic potential of a bubble may be estimated (§ 2) one may investigate the consequences of this type of potential interaction, similarly to the molecular dynamics case in which a known (e.g. Lennard-Jones) potential is used to investigate the overall properties of a system (fig. 5.2).

The application of statistical thermodynamics to bubbly flow has been previously suggested by Smerka [41], mainly with a view to establishing constitutive relationships for bubbly fluids. Yurkovetsky and Brady [49] carried out a computation of the collective properties of a bubbly flow with the bubbles modeled as dipoles. The main new points studied in the present research are:

1. the possibility of defining a rational procedure to isolate velocity fluctuations brought about by the hydrodynamic interactions between bubbles from those associated with the liquid turbulence;

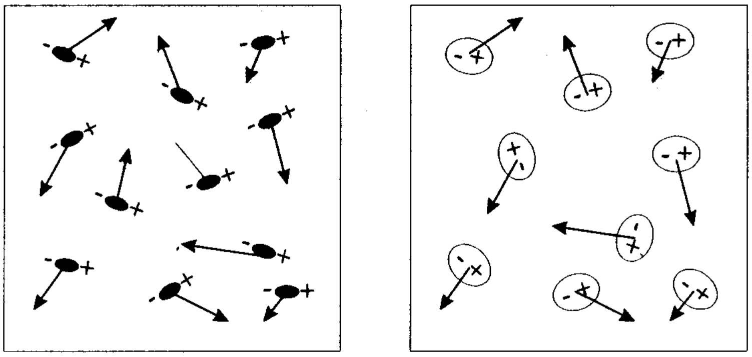

Figure 5.1: Analogy between molecules interacting through electric fields and bubbles interacting through hydrodynamic fields.

2. the implications of collective bubble behavior for the turbulence of the liquid phase.

5.2 Bulk behavior estimates from pairwise interaction potential

5.2.1 Some results from kinetic theory

It is well known from kinetic theory [19] that simple models of molecular interaction furnish insight into the bulk properties of fluids. For instance, the hypothesis of an ideal gas, interacting only through elastic collisions, leads to an estimate of the bulk viscosity

$$\mu = \frac{1}{2}\rho \bar{v} L \tag{5.1}$$

(ρ - bulk density, $\bar{v}$ - mean molecular viscosity, L - mean free path length) that furnishes estimates within 10-20% of the measured dynamic viscosity. More refined estimates, furnishing 2 or 3 significant digits of the viscosity, may be obtained by introducing more realistic models of molecular interaction. A widely used interaction model is that suggested by Lennard-Jones [25]

$$P = \frac{a}{r^m} - \frac{b}{r^n}, \tag{5.2}$$

which gives estimates precise enough for most practical applications. P is the interaction force. The corresponding force potential would have the form

$$V = \frac{\alpha}{r^{m-1}} - \frac{\beta}{r^{n-1}}.$$

The details of obtaining the viscosity from the above interaction force model involves computation of the so-called "collision-integrals", a tedious procedure which shall not be reproduced here. The final result [5] of interest is the estimate of dynamic viscosity,

$$\mu = \mu_0 \left\{ 1 + S\,(2kT)^{\frac{3-m}{m-1}} \right\}^{-1} \tag{5.3}$$

with

$$S = 2\frac{B_2(m)}{A_2(m)} \frac{b}{a^{\frac{2}{m-1}}} \frac{1}{\Gamma\left(4-\frac{2}{m-1}\right)} \tag{5.4}$$

$$\mu_0 = \frac{5\sqrt{\dfrac{m_M kT}{\pi}} \left(\dfrac{2kT}{a}\right)^{\frac{2}{m-1}}}{8\,\Gamma\left(4-\dfrac{2}{m-1}\right) A_2(m)} \tag{5.5}$$

for a long range $n = 3$ attractive interaction. In the above μ_0 represents the viscosity of a gas interacting through collisions (a limiting case of the potential interaction model with no attraction, and strong repulsion on distances on the order of the molecular diameter). Other quantities are T - the temperature, Γ - the Euler gamma function, m_M - the molecular mass and k - the Boltzmann constant. The numerical coefficients A_2 and B_2 depend on the details of the interaction potential and are given in the following table.

Table of $A_2(m), B_2(m)$ coefficients [5]

m	$A_2(m)$	$B_2(m)$
5	0.436	-0.4829
7	0.357	-0.2758
9	0.332	-0.1649
11	0.319	-0.0953
15	0.309	-0.0177
21	0.307	0.0514
25	0.306	0.0804
∞	0.333	0.2337

A final point from the kinetic treatment of gases that is significant is the observation that viscosity arises as a result of the departure of the velocity distribution from the Maxwell distribution. This is the molecular level explanation of why viscosity appears only as a result of fluid motion. The fluid motion introduces a bias in the average molecular velocities that gives a deviation from the Maxwell distribution.

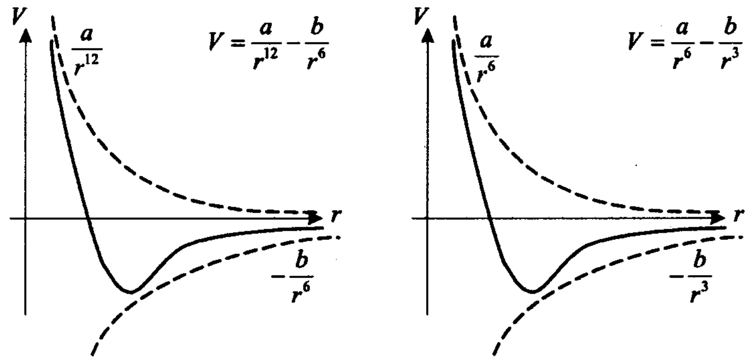

Figure 5.2: Analogy between pairwise potential interactions for molecular dynamics and bubble hydrodynamics.

5.3 Some results from statistical thermodynamics of gases

Another aspect of interest in the study of gases is the prediction of phase transitions. It is known that the ideal gas model leads to an equation of state

$$\frac{p}{T} = \frac{R}{v} \tag{5.6}$$

which exhibits no phase transition. This is to be expected from the molecular viewpoint since the interaction is strictly collisional corresponding to a repulsive short range potential and no attractive longer range component. It is, therefore, not possible to have the sort of collective behavior necessary for modeling a phase transition. The simplest model exhibiting a phase transition is the Van der Waals gas for which the equation of state becomes

$$\frac{p}{T} = \frac{R}{v}\left(1 + \frac{B(T)}{v}\right). \tag{5.7}$$

The initial derivation by Van der Waals of the above equation was heuristic. Further research [19], [37] showed that (5.7) is the first term in a general expansion, the so-called "virial expansion"

$$\frac{p}{T} = \frac{R}{v}\left(1 + \frac{B(T)}{v} + \frac{C(T)}{v^2} + \dots\right) \tag{5.8}$$

in which the coefficients $B(T), C(T), \dots$ model pair, triplet interactions and so on. These coefficients may be computed from a model of the interaction potential. The most important is the pair interaction coefficient, also known as the *second virial coefficient*, which is

$$B = \frac{N_A}{2} \int_0^\infty \{1 - \exp\left[V(r)/RT\right]\} 4\pi r^2 dr \tag{5.9}$$

with R the gas constant. The critical state (where a phase transition occurs) is then predicted by

$$\left(\frac{\partial p}{\partial v}\right)_{T_{cr}} = 0\,. \tag{5.10}$$

5.4 Analogous quantities for dilute bubbly flow

We now turn to the problem of determining analogous quantities for ideal dilute bubbly flow. The first important aspect is to identify how a system temperature may be gainfully defined. Recall that our final objective is to furnish a rational means of separating fluctuations in a bubbly flow that are due to true liquid turbulence from those that are associated with bubble motion. The mixture exhibits enhanced transport properties, typically captured in an increased transport coefficient such as a mixture effective viscosity. The interest here is to investigate the means by which the mixture effective viscosity may be determined from the molecular viscosity of the liquid and a model of the interaction between the bubbles. Given the negligible mass of the bubbles with respect to the liquid it is natural to assume that the fluctuations of the turbulent liquid flow form a thermal background for the bubbles. A rigorous argument, based upon defining the equilibrium of the canonical ensemble for ideal bubbly flow, leads to the same conclusion [49]. The appropriate replacement for the temperature is therefore

$$kT \leftarrow \frac{1}{\beta} = \frac{1}{3\rho\tau N}\left\langle \mathbf{p}\cdot\mathbf{M}\cdot\mathbf{p}\right\rangle \tag{5.11}$$

where ρ is the liquid density, N - the number of bubbles, $\tau = 4\pi R^3/3$ - the bubble volume, $\mathbf{p}$ - the vector of all the bubbles' fluctuating impulse and $\mathbf{M}$ - the virtual mass matrix of the system. The virtual mass matrix of an ensemble of N bubbles has been computed by Yurkovetsky and Brady as

$$\mathbf{M} = -(\mathbf{I} - \mathbf{M}_1)^{-1}\cdot\mathbf{M}_2\,, \tag{5.12}$$

with $\mathbf{M}_1$ and $\mathbf{M}_2$ reflecting the relative positions of the bubbles,

$$\mathbf{M}_1 = -\frac{R^3}{2}\begin{bmatrix} \mathbf{0} & \nabla\nabla r_{12}^{-1} & \cdots & \nabla\nabla r_{1N}^{-1} \\ \nabla\nabla r_{21}^{-1} & \mathbf{0} & \cdots & \nabla\nabla r_{2N}^{-1} \\ \vdots & \vdots & \ddots & \vdots \\ \nabla\nabla r_{N1}^{-1} & \nabla\nabla r_{N2}^{-1} & \cdots & \mathbf{0} \end{bmatrix} \tag{5.13}$$

$$\mathbf{M}_2 = -\frac{R^3}{2}\begin{bmatrix} R^{-3}\mathbf{I} & \nabla\nabla r_{12}^{-1} & \cdots & \nabla\nabla r_{1N}^{-1} \\ \nabla\nabla r_{21}^{-1} & R^{-3}\mathbf{I} & \cdots & \nabla\nabla r_{2N}^{-1} \\ \vdots & \vdots & \ddots & \vdots \\ \nabla\nabla r_{N1}^{-1} & \nabla\nabla r_{N2}^{-1} & \cdots & R^{-3}\mathbf{I} \end{bmatrix} \tag{5.14}$$

and $\mathbf{r}_{ij}$ the relative position vector between bubbles i and j, $r_{ij} = \|\mathbf{r}_{ij}\|$. The kinetic energy of the bubble ensemble may be expressed in terms of the virtual mass matrix as

$$K = \frac{1}{2}\rho\tau\mathbf{U}\cdot\mathbf{M}\cdot\mathbf{U} \tag{5.15}$$

where $\mathbf{U}$ is the vector of bubble center velocities. The molecular mass appearing in the kinetic theory formula (5.5) is therefore appropriately replaced by the norm of the virtual mass matrix

$$m_M \leftarrow \frac{\rho\tau}{N}\|\mathbf{M}\| \tag{5.16}$$

with N the number of bubbles.

The last quantity for which an analogy must be established is the second virial coefficient which is now expressed as [24]

$$B(\beta) = \frac{1}{2}\int [1 - \exp(-\beta V)]\, d\Omega \tag{5.17}$$

the integration running over the volume of interest. The second order approximation to the equation of state for the bubbly flow is

$$p = \frac{1}{\beta v}\left(1 + \frac{B(\beta)}{v}\right). \tag{5.18}$$

5.5 Predictions from the analogy

Carrying out the above analogy in full would require knowledge of the bubble distribution. This type of information is, however, superfluous if all we're interested in is to construct a subgrid scale turbulence model. In order to make progress towards this goal an assumed local distribution and estimate of the norm of the virtual mass matrix may be made. The most natural hypothesis is to assume a uniform spatial distribution of the unresolved bubbles within a computational grid cell of volume $V_G = \Delta x\,\Delta y\,\Delta z$. Let $X(R)$ be the normalized distribution of bubbles of radius R within the grid cell, so that the total void volume is

$$V = \frac{4\pi}{3}\int_0^\infty X(R)R^3 dR \tag{5.19}$$

and the local void fraction is

$$f = \frac{V}{V_G}. \tag{5.20}$$

Isolate a band of radius values $(R, R + dR)$. The average separation between these bubbles is

$$r_R = (V_G - V)^{1/3} = (1 - f_R)^{1/3} V_G^{1/3} \tag{5.21}$$

where f_R is the void fraction of the $(R, R+dR)$ band,

$$f = \int_0^\infty X(R) f_R dR \,. \tag{5.22}$$

The Hessian $\nabla\nabla r_{ij}^{-1}$ is of order

$$\nabla\nabla r_{ij}^{-1} \cong \frac{1}{r_R^3} \tag{5.23}$$

in this case. Using the 2-norm in (5.16), the contribution to the virtual mass from this band of radius values is

$$m_{M,R} = \frac{\rho\tau}{4} \cdot \frac{1+2\varepsilon}{1-\varepsilon} \tag{5.24}$$

with

$$\varepsilon = \frac{1}{2}\frac{R^3}{r_R^3} \,. \tag{5.25}$$

Since we are considering dilute bubbly flow, the bubble radius R is much less than the average separation r so ε is small and

$$m_{M,R} = \frac{\rho\tau}{4}(1+2\varepsilon)(1+\varepsilon+\dots) \cong \frac{\rho\tau}{4}(1+3\varepsilon) = \frac{\rho\tau}{4}\left\{1+\frac{3}{2}\left(\frac{R}{r_R}\right)^3\right\} . \tag{5.26}$$

The typical virtual mass associated with one bubble may now be estimated as

$$m_M = \frac{\rho\tau}{4}\int_0^\infty X(R)\left\{1+\frac{3}{2}\left(\frac{R}{r_R}\right)^3\right\} dR \tag{5.27}$$

or

$$m_M = \frac{\rho\tau}{4}\int_0^\infty X(R)\left\{1+\frac{3}{2}\frac{R^3}{(1-f_R)V_G}\right\} dR \,. \tag{5.28}$$

The simplest case is when all unresolved bubbles are assumed to be of a single radius, say R_0, in which case $X(R) = \delta(R-R_0)$ and the virtual mass estimate becomes

$$m_M = \frac{\rho\tau}{4}\left\{1+\frac{3}{2}\frac{R_0^3}{(1-f)V_G}\right\} . \tag{5.29}$$

5.5.1 Estimates of the additional viscosity

In order to use (5.3) we must adopt a hydrodynamic interaction potential. The analysis of chapter 2 and the analytical representation of the potential flow around spheres and ellipsoids [22] give the first approximation potential as that between dipoles. The pairwise attractive potential is in this case $\sim r^{-2}$. The short range repulsive behavior of bubbles interacting through an inviscid potential and which do not coalesce is $\sim r^{-6}$ so the appropriate total pairwise interaction force has the form

$$P = \frac{a}{r^7} - \frac{b}{r^3}. \tag{5.30}$$

Replacing $m = 7$ and $n = 3$ in (5.3) we obtain

$$\mu^V = \mu_0 \left(1 - 0.243 \frac{b}{a^{1/3}} \beta^{2/3}\right) \tag{5.31}$$

$$\mu_0 = 0.3102 \frac{\sqrt{m_M}}{a^{1/3} \beta^{5/6}}\,. \tag{5.32}$$

For single radius unresolved bubbles we may use (5.29) and obtain

$$\mu_0 = \frac{0.155}{a^{1/3}\beta^{5/6}} \sqrt{\rho\tau \left[1 + \frac{3}{2} \frac{R_0^3}{(1-f)V_G}\right]}.$$

The question naturally arises as to the significance of this viscosity. Recall that for molecular viscosity the interpretation is the transfer of momentum tangentially, typically visualized as the lateral transfer of a packet of fluid into a region of different streamwise momentum. The bubbles are also able to transfer momentum laterally through the interaction of their hydrodynamic fields. The interpretation of μ is therefore that it represents an additional tangential momentum transfer coefficient. The shear it induces is also proportional to the strain rate

$$\tau_{ij}^V = \frac{\mu^V}{2} \left(\frac{\partial U_i}{\partial x_j} + \frac{\partial U_j}{\partial x_i}\right).$$

This is understandable since there must be difference in the relative velocities of a bubble pair in order for one to accelerate the other in the streamwise direction. The kinetic viscosity is obtained by dividing by the virtual density

$$\nu^V = \frac{\mu^V}{\rho\left[1 + \frac{3}{2}\frac{R_0^3}{(1-f)V_G}\right]} = \frac{0.155}{a^{1/3}\beta^{5/6}} \sqrt{\frac{\tau}{\rho} \left[1 + \frac{3}{2} \frac{R_0^3}{(1-f)V_G}\right]^{-1}}. \tag{5.33}$$

5.5.2 Phase transition prediction

The second prediction of the statistical thermodynamic approach is the existence of a phase transition between "gas"-like behavior in which the bubbles have independent fluctuating velocities and "gas"-like behavior in which the bubbles form a cluster. The transition occurs at a temperature given by the solution of

$$\left(\frac{\partial p}{\partial v}\right)_{\beta_{cr}} = 0\,. \tag{5.34}$$

Using (5.18) the critical value of β is the solution of

$$B(\beta_{cr}) = -\frac{v}{2}\,. \tag{5.35}$$

Replacing (5.30) in the expression for the second virial coefficient, expanding the exponential and keeping only first order terms leads to

$$B = -4\pi\beta \ln \frac{R_G}{R} \tag{5.36}$$

with R_G a radius representative of the grid cell volume

$$R_G = \left(\frac{3V_G}{4\pi}\right)^{1/3}\,. \tag{5.37}$$

The above evaluation disregards bubble interactions separated by more than a representative dimension of the grid cell. This cutoff is similar to the screened potential appearing in evaluations in which the integration domain is extended to infinity. The above expression of the virial coefficient leads to a critical value for β of

$$\beta_{cr} = \frac{1}{8\pi}\frac{v}{b}\frac{1}{\ln(R_G/R)}\,. \tag{5.38}$$

The above formula predicts that the critical temperature

$$T_{cr} \sim \frac{1}{\beta_{cr}} \sim \frac{1}{v} = \frac{N}{V_G} = \frac{N\tau}{V_G\tau} = \frac{1}{\tau}\frac{V}{V_G} = \frac{f}{\tau} \tag{5.39}$$

is proportional to the void fraction.

The interpretation of the phase transition is that in ideal, dilute bubbly flow there is a threshold value for the liquid turbulence intensity under which the bubbles tend to form clusters and above which they behave independently. This is important for turbulence models since it suggests that the relevant physical length scale is the correlation length when the bubbles form clusters and the mean distance between the bubbles when they behave independently.

5.6 Current experimental evidence and suggestions for further verifications

Detailed quantitative experiments on bubbly flow are still rare. There are some indications of the domain of validity of the potential interaction approach from Duineveld [9]. The important implication from Duineveld's experiments for this work is that a domain in which the current approach may be tested does exist. This furnishes a test bed on which the turbulence models may be tested.

Another set of experiments of interest are those by Lance and Bataille [23]. Figure 5.3 reproduced from that work shows evidence of a change in the excess turbulent

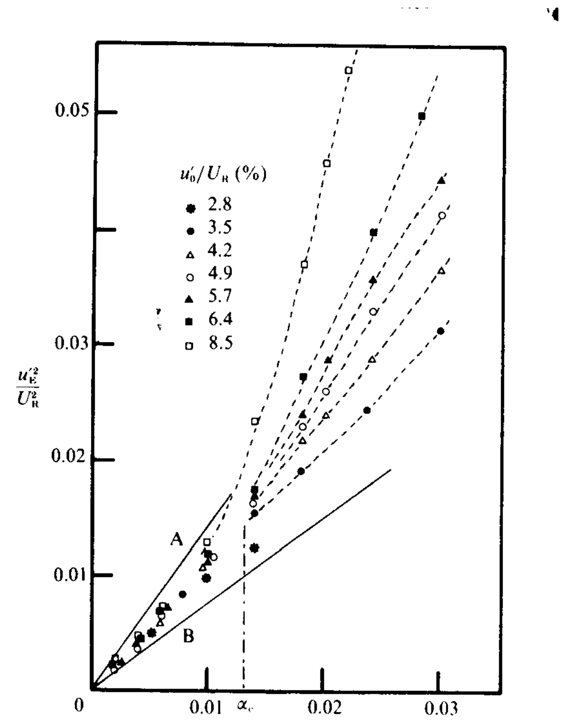

Figure 5.3: Change in excess turbulent fluctuations as a function of the void fraction. Experimental results from Lance and Bataille [23].

fluctuations when the void fraction exceeds a critical value. The qualitative observation is in line with the predictions of a phase transition from the potential interaction approach, even though the quantitative values at which the phase transition occurs are not in agreement with the theory.

The above summary inspections of the available experimental data suggest that the interaction potential approach is viable but the exact form of the potential used is open to question. In particular the dipolar interaction potential used in the previous sections is hardly a comprehensive description of the interaction process. The principal critique of the dipolar interaction potential is that it does not include any deformation effects of the bubble arising from compression of the gas under the influence of the liquid velocity fluctuations and from bubble surface oscillations.

The above observations indicate that the most important piece of information that should be obtained from experiment or numerical simulation is a more precise approximation of the pairwise interaction potential, especially under turbulent flow conditions. From the point of view of numerical simulation this would require direct numerical simulations of a pair of bubbles in a turbulent flow field. From the experimental viewpoint, one may envisage an experiment in which bubble pairs are tracked while in a turbulent flow field and use the measured trajectories to obtain a least-squares estimate of the pairwise interaction potential parameters.

Chapter 6

Turbulence models for bubbly flow

The problem of the derivation of turbulence models for bubbly flow is now considered. Through the statistical thermodynamics treatment presented in the previous chapter an effective "viscosity" of the interacting bubbles has been determined. This information may be used in building turbulence models in a variety of means, similarly to the construction of turbulence models for single phase flow. One particular technique is studied here, namely the application of the renormalization group to the Navier-Stokes equations for the liquid phase in which the viscosity is modified in order to reflect the interaction of the liquid with the gas bubbles.

6.1 General principles of the renormalization group

The renormalization group (RNG) is a general field theoretic technique used to study the behavior of systems with many degrees of freedom. The technique involves the study of the properties of the system are modified under operations of changes of scale and has had its most notable success in the study of phase transitions [47]. The technique has also been suggested as a means of studying the general turbulence problem [48], in which application it has had limited success. An exposition of the RNG applications to turbulence may be found in McComb [27] and some recent developments in an ICASE report [50]. The simplest application of RNG is probably the study of phase transitions of discrete spin systems. This classic example has been presented extensively in the RNG literature. Just a few points are made here in order to better understand the application of RNG to the more complicated situation of turbulent flow.

A spin system consists of particles placed at the nodes of a discrete lattice. In one such model system (known as the Ising model 6.1) the spins are assumed to interact only with their nearest neighbor. The model is a simplification of the physics of magnetism. The interest is to establish whether such a simple model can exhibit some of the phenomena of real magnetic systems, mainly the existence of phase transitions. In a phase transition a physical system exhibits some overall change in its properties. Such changes can only be realized if the components of the system interact collectively. For the Ising model the question is whether the large number of pair interactions present in the model can lead to cooperative behavior. Cooperative

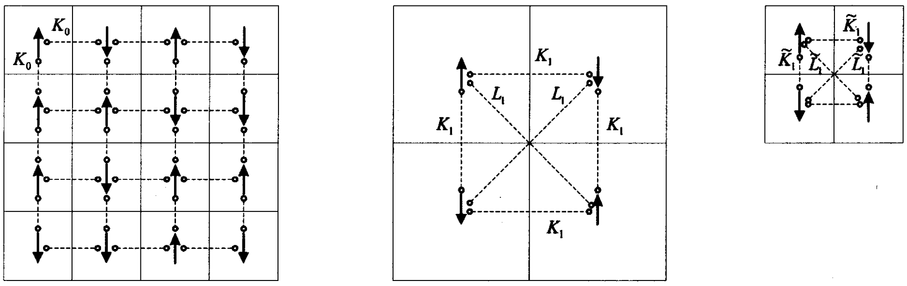

Figure 6.1: Representation of RNG applied to 2D Ising model.

behavior is understood here as correlated values of the spin over a large number of sites.

The physical behavior of the initial system is completely contained in the Hamiltonian function

$$H_0 = K_0 \sum_i \sum_{nn} s_i^{(0)} s_j^{(0)}. \tag{6.1}$$

The above formula affirms that the system Hamiltonian is the sum over all lattice points $(\sum_{i,j})$ of all nearest-neighbors $(\sum\limits_{nn})$ pair interactions $K_0 s_i^{(0)} s_j^{(0)}$. For a given lattice node (i, j) the nearest neighbor would be $(i \pm 1, j)$, $(i, j \pm 1)$. The specifics of the physical situation are not of direct interest here. The only important piece of information is that the coupling constant $K = K_0$ is small so perturbation expansions are possible. The effects of a change of scale operation are now investigated. If the system were to be looked at with half the original resolution the outer sum would run over only half of the lattice nodes $(\sum_{i,2})$. The same physical system must be described so the inner sum cannot include just the nearest neighbor interactions since this would leave out some of the interactions. We must also include next-nearest neighbor interactions $(\sum\limits_{nnn}$, corresponding to $(i \pm 1, j \pm 1))$ in the Hamiltonian

$$\begin{aligned} H_1 &= A_1 \frac{N^2}{2} + 2B_1 \sum_{i,2} \sum_{nn} s_i^{(1)} s_j^{(1)} + B_1 \sum_{i,2} \sum_{nnn} s_i^{(1)} s_j^{(1)} s_k^{(1)} + \ldots \\ &= A \frac{N^2}{2} + K_1 \sum_{i,2} \sum_{nn} s_i^{(1)} s_j^{(1)} + L_1 \sum_{i,2} \sum_{nnn} s_i^{(1)} s_j^{(1)} s_k^{(1)} + \ldots \quad . \end{aligned} \tag{6.2}$$

The Hamiltonian is now computed by a sum with half as many terms as before but has a more complicated structure because of the *nnn* term. The new coupling constants may be expressed in terms of the old as

$$A_1(K) \cong \ln 2 + 2K^2 + O(K^4) \quad B(K) \cong K^2 + O(K^4). \tag{6.3}$$

Since we would like to apply the procedure recursively, we define an average of the spins included in the $i, 2$ sum (step 2 of fig. 6.1), and try to rewrite the Hamiltonian in a similar form (6.2) but with different coupling constants

$$H_2 = A_2 \frac{N^2}{2^2} + K_1 \sum_{i,2} \sum_{nn} s_i^{(1)} s_j^{(1)} + L_1 \sum_{i,2} \sum_{nnn} s_i^{(1)} s_j^{(1)} s_k^{(1)} + \dots \quad . \tag{6.4}$$

The sequence of operations is therefore

1. averaging of spins to obtain a "block spin";
2. rewriting the Hamiltonian in order to obtain a form similar to the original form.

It may be repeated indefinitely leading to the recursion relations for the coupling constants

$$K_i = 2K_{i-1}^2 + L_{i-1} \tag{6.5}$$

$$L_i = K_i^2. \tag{6.6}$$

The important physical question is now to ask whether there exist fixed points of the above system (6.5). If such points exist, then the coupling constants would no longer change under the scale transformation. We can then affirm that all relevant physical degrees of freedom have been accounted for. In order to seek fixed points we solve the system

$$K_* = 2K_*^2 + L_* \tag{6.7}$$

$$L_* = K_*^2 \tag{6.8}$$

and obtain the solutions

$$(K_*, L_*) \in \{(0,0), (\infty, \infty), (1/3, 1/9)\}. \tag{6.9}$$

The first two solutions are not interesting physically. They correspond to perfectly disordered and perfectly ordered systems. When $(K_*, L_*) = (1/3, 1/9)$ we have an interesting situation in that there exists cooperative behavior between the block spins and the coupling constants remain constant.

The relevance of this for fluid turbulence is that we hope to find for the Navier-Stokes solution also a fixed point at which the coupling constant (i.e. the turbulent viscosity) remains constant.

6.2 Derivation of an eddy-viscosity model for single phase flow by RNG

There are a number of variants of the RNG technique applications to turbulence [48], [27], [35]. The specific technique adopted here is that of "iterative averaging" [35]. A summary of the application of this technique to single-phase flows is now

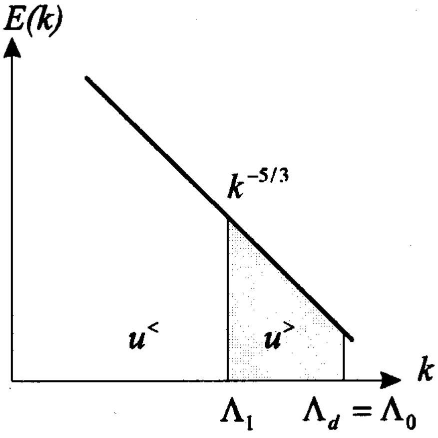

Figure 6.2: Wavebands of turbulent energy eliminated in the RNG process.

presented. The velocity field of a fluid is separated into an average part ($\overset{\frown}{U}_i$) and a fluctuating part (u_i) by appropriately truncating their Fourier expansions

$$\overset{\frown}{U}_i(\mathbf{x},t) = \sum_{k \ll \Lambda_e} \overset{\frown}{U}_i(\mathbf{k},t) \exp(i\mathbf{k}\cdot\mathbf{x}) \tag{6.10}$$

$$u_i(\mathbf{x},t) = \sum_{k \gg \Lambda_e} u_i(\mathbf{k},t) \exp(i\mathbf{k}\cdot\mathbf{x}) \tag{6.11}$$

with Λ_e the wavenumber of the energetic eddies. Note that this corresponds to the spatial averaging technique used in LES. We are interested in finding what effect the fluctuations have upon the average velocities. This is to be studied by systematically eliminating some of the degrees of freedom of the system. The wavenumber range is divided into slices $S_p = (\Lambda_{p+1}, \Lambda_p)$ with

$$\Lambda_{p+1} = (1-\epsilon)\Lambda_p \tag{6.12}$$

and $0 < \epsilon \ll 1$. We seek to successively eliminate each waveband S_p by computing its influence upon the velocities at lower wavenumbers.

The fluctuating velocity is split into a part outside the waveband to be eliminated $u^{<}$ and a part within this waveband $u^{>}$. For the first waveband this may be written as:

$$u_i(\mathbf{k},t) = u_i^{<}(\mathbf{k},t) + u_i^{>}(\mathbf{k},t) \tag{6.13}$$

$$u_i^{<}(\mathbf{k},t) = \left\{ \begin{array}{cc} 0 & k \in S_0 \\ u_i(\mathbf{k},t) & k \notin S_0 \end{array} \right. , \quad u_i^{>}(\mathbf{k},t) = \left\{ \begin{array}{cc} u_i(\mathbf{k},t) & k \in S_0 \\ 0 & k \notin S_0 \end{array} \right. . \tag{6.14}$$

In order to eliminate the S_0 waveband we must compute its effect upon the other velocity components. This is similar to the operation of rewriting the Hamiltonian in the Ising model above. In our case the equation governing the physics is the Navier Stokes equation. It is convenient to use this equation in Fourier space

$$\left(\frac{\partial}{\partial t} + \nu_0 k^2\right) u_i(\mathbf{k}, t) = -\frac{i}{2} P_{imn}(\mathbf{k}) \sum_q u_m(\mathbf{q}, t) u_n(\mathbf{k} - \mathbf{q}, t) \tag{6.15}$$

where

$$P_{imn}(\mathbf{k}) = k_m P_{in}(\mathbf{k}) + k_n P_{im}(\mathbf{k}) \tag{6.16}$$

$$P_{ij}(\mathbf{k}) = \delta_{ij} - \frac{k_i k_j}{k^2}. \tag{6.17}$$

The nonlinearity of the Navier-Stokes equations in real space leads to the convolution sum in (6.15). This is the term which shall give the effect of the high-k modes upon the low-k modes.

Similarly to the definition of block spins in the Ising model an averaging operation must also be introduced. The averaging should be over the scales which are to be eliminated, and is called a conditional average [27], [35]. It affects only the high-k modes with S_p. The conditional average of the convolution product gives

$$\left\langle \sum_q u_m u_n \right\rangle_c = \left\langle \sum_q u_m^< u_n^< + u_m^< u_n^> + u_m^> u_n^< + u_m^> u_n^> \right\rangle_c . \tag{6.18}$$

We have

$$\left\langle \sum_q u_m^< u_n^< \right\rangle_c = \sum_q u_m^< u_n^< \tag{6.19}$$

since the conditional average does not affect the low-k modes. For the same reason we obtain

$$\left\langle \sum_q u_m^< u_n^> \right\rangle_c = \sum_q u_m^< \langle u_n^> \rangle_c = 0 \tag{6.20}$$

$$\left\langle \sum_q u_m^> u_n^< \right\rangle_c = \sum_q \langle u_m^> \rangle_c u_n^< = 0 \tag{6.21}$$

so the average of the convolution sum comes out as

$$\left\langle \sum_q u_m u_n \right\rangle_c = \sum_q u_m^< u_n^< + \sum_q \langle u_m^> u_n^> \rangle_c \tag{6.22}$$

as might have been expected. We encounter the typical situation in which the effect upon the larger scales of motion is through a correlation of the product of smaller scale fluctuations. The conditional average of the small scale fluctuations may be estimated by a perturbation expansion of the transport equation for the second order velocity correlation [35]

$$\sum_q \langle u_m^> u_n^> \rangle_c = -\nu_1 s_{mn} \tag{6.23}$$

with

$$s_{mn} = i\left(k_m \overset{\backsim}{U}_n + k_n \overset{\backsim}{U}_m\right) \tag{6.24}$$

$$\nu_1 = \Delta\nu_0 = \frac{7}{30\nu_0}\int_{\Lambda_1}^{\Lambda_0} \frac{E(q)}{q^2} dq\,. \tag{6.25}$$

The situation is similar to that encountered in the Ising model. A new coupling constant ν_1 has been introduced which captures the effect of the eliminated waveband S_1.

The procedure may be repeated and we obtain a recursion relation for the effective viscosity

$$\nu_{n+1} = \nu_n + \Delta\nu_n \tag{6.26}$$

$$\Delta\nu_n = \frac{7}{30\nu_n}\int_{\Lambda_{n+1}}^{\Lambda_n} \frac{E(q)}{q^2} dq. \tag{6.27}$$

In the case of fluid turbulence a fixed point would be obtained when there are no more significant changes to ν_v, that is when $E(q)/q^2$ starts having negligible contributions to the above integral.

If all of the scales of motion, up to that of the energy containing eddies Λ_e, are included in the above process we obtain in the end an eddy viscosity model. The final effective viscosity is

$$\nu_N = \sqrt{\frac{7\alpha}{40}}\varepsilon^{1/3}(\Lambda_N^{-8/3} - \Lambda_0^{-8/3})^{1/2} \tag{6.28}$$

but since $\Lambda_N \ll \Lambda_0$ we have

$$\nu_N = \sqrt{\frac{7\alpha}{40}}\varepsilon^{1/3}\Lambda_N^{-4/3}. \tag{6.29}$$

In this formula Nagano and Itazu [35] have set $\Lambda_N = \Lambda_e$ and used the relation between the total turbulent kinetic energy K and the dissipation rate ε

$$\Lambda_e = \left(\frac{3\alpha}{2}\right)^{3/2} \frac{\varepsilon}{K^{3/2}} \tag{6.30}$$

to obtain

$$\nu_{eff} = C_\mu \frac{K^2}{\varepsilon} \tag{6.31}$$

with

$$C_\mu = \sqrt{\frac{7\alpha}{40}} \left(\frac{2}{3\alpha}\right)^2 \tag{6.32}$$

or using the accepted $\alpha = 1.6$ value for the Kolmogorov constant

$$C_\mu = 0.092 \tag{6.33}$$

a value in good agreement with standard eddy viscosity models.

For a SGS model we would set Λ_N equal to the largest wave number resolved by the grid.

6.3 Derivation of an eddy-viscosity model for bubbly flow by RNG

6.3.1 Using an assumed turbulent kinetic energy spectrum

We now turn to how the above technique may be applied to bubbly flow. The additional viscosity at each step of the RNG procedure was determined above (6.27) by using the Kolmogorov spectrum for the turbulent kinetic energy

$$E(k) = \alpha \varepsilon^{2/3} k^{-5/3}. \tag{6.34}$$

In bubbly flow, experimental results [23] suggest that the dependence of the turbulent kinetic energy on the wavenumber is $E(k) \sim k^{-8/3}$. If such a dependence is accepted we may use the following turbulent energy spectrum

$$E(k) = \alpha \varepsilon^{2/3} k^{-8/3} / \lambda \tag{6.35}$$

in (6.27) where λ is a length indicative of the bubble interactions needed to ensure dimensional homogeneity. Carrying out the computations we find that

$$\nu_N^2 = \sum_{i=0}^{N-1} (\nu_{i+1}^2 - \nu_i^2) = 2 \sum_{i=0}^{N-1} \nu_i \Delta\nu_i + \underbrace{\sum_{i=0}^{N-1} (\Delta\nu_i)^2}_{O(\varepsilon^2)} = \frac{7\alpha}{55} \varepsilon^{2/3} \left(\Lambda_N^{-11/3} - \Lambda_0^{-11/3}\right) / \lambda.$$

An eddy-viscosity model may now be written as

$$\nu = C_\mu \frac{K^2}{\varepsilon}, \quad C_\mu = 0.078/\sqrt{\lambda}.$$

If an SGS model is sought the appropriate expression is

$$\nu_N^2 = \frac{7\alpha}{55}\varepsilon^{2/3}\left(\Lambda_N^{-11/3} - \Lambda_0^{-11/3}\right)/\lambda \tag{6.36}$$

with Λ_N the highest wavenumber resolved by the grid. Since $\Lambda_N \ll \Lambda_0$ we have

$$\nu_N = \sqrt{\frac{7\alpha}{55\lambda}\frac{\varepsilon^{1/3}}{\Lambda_N^{11/6}}}. \tag{6.37}$$

The difficulty that arises in this approach is what length λ should be used in the above models to describe the interaction range of the bubbles. To answer this question further experimental and numerical simulation results must be waited for. The existence of a phase transition in the clustering behavior of the bubbles does however suggest that λ should be taken as r_R, the average separation between two bubbles when there is no clustering (high thermal background motion). When the thermal background is low, and bubble clusters form, λ should be taken as representing the average cluster size (e.g. a correlation length). This observation leads to a turbulence model which dynamically adapts to the local state of the bubbles.

6.3.2 Using a bubbly mixture viscosity

Another approach is to employ the results from the statistical thermodynamics analysis presented in §5. The attractive aspect of this approach is that it is more rational. If an acceptable approximation of the bubble pairwise interaction potentials can be achieved then the bubbly mixture viscosity ν^V may be computed. The mixture viscosity corresponding to a specific waveband being eliminated may then be used in the RNG computation

$$\nu_{n+1} = \nu_n + \Delta\nu_n + \nu_n^V = \nu_n + \frac{7}{30\nu_n}\int_{\Lambda_{n+1}}^{\Lambda_n}\frac{E(q)}{q^2}dq + \nu_n^V \tag{6.38}$$

$$\nu_n^V = \frac{0.155}{a^{1/3}\beta^{5/6}}\sqrt{\frac{\tau_n}{\rho}\left[1 + \frac{3}{2}\frac{R_n^3}{(1-f_n)V_G}\right]^{-1}} \tag{6.39}$$

and an overall effective viscosity or an SGS model determined. In the above R_n is the size of the bubbles whose influence is being considered in step n of the RNG procedure, f_n is the void fraction of the bubbles of radius R_n and τ_n is their volume defined as

$$\tau_n = \frac{4\pi}{3}R_n^3 H(f_n)\,. \tag{6.40}$$

The Heaviside function $H(f_n)$ appears so as to zero out any contributions when there are no bubbles of size R_n in the mixture, i.e. when $f_n = 0$.

In order to carry out the above strategy a procedure must be established which selects which bubbles are included in the elimination of a spectral waveband. When the wavenumber is in the $(\Lambda_{n+1}, \Lambda_n)$ waveband the relevant length scale is

$$l_n = \frac{2\pi}{\Lambda_n}. \tag{6.41}$$

The bubble sizes to be considered in this waveband must be small enough so that the dilute bubbly flow hypothesis remains valid. Let $f_{\max}$ be the limiting upper value of the void fraction that defines dilute bubbly flow. Typically $f_{\max} \leq 0.05$. The bubble sizes that should be included in this waveband are then

$$R_n = \left(\frac{3f_{\max}}{4\pi}\right)^{1/3} l_n = \left(\frac{3f_{\max}}{4\pi}\right)^{1/3} \frac{2\pi}{\Lambda_n}. \tag{6.42}$$

The volume over which the dilute bubbly flow hypothesis is being applied at stage n of the RNG procedure is

$$V_G = l_n^3\,. \tag{6.43}$$

Using (6.40)-(6.43) the additional viscosity due to the bubbles comes out as

$$\nu_n^V = \frac{0.155}{a^{1/3}\beta^{5/6}} \sqrt{\frac{f_{\max} H(f_n)}{\rho} \left(\frac{2\pi}{\Lambda_n}\right)^3 \left[1 + \frac{9f_{\max}}{4\pi(1-f_n)}\right]^{-1}}\,. \tag{6.44}$$

The sum of all these contributions over the entire wavenumber range eliminated in the RNG procedure is

$$\sum_{n=0}^{N-1} \nu_n^V = \frac{2.44\, f_{\max}^{1/2}}{a^{1/3}\beta^{5/6}\rho^{1/2}} \sum_{n=0}^{N-1} \frac{\sqrt{H(f_n)}}{\Lambda_n^{3/2}} \left[1 + \frac{9f_{\max}}{4\pi(1-f_n)}\right]^{-1/2}. \tag{6.45}$$

The evaluation of the above sum generally requires knowledge of the distribution of bubble sizes (the f_n term). This, of course, shall not be available for unresolved grid cells and a hypothesis must be made about this distribution. Lacking experimental data at present, we make the simplest choice

$$f_n = const = \bar{f} > 0. \tag{6.46}$$

The additional viscosity may now be estimated as

$$\sum_{n=0}^{N-1} \nu_n^V = \frac{1.22\, f_{\max}^{1/2}}{a^{1/3}\beta^{5/6}\rho^{1/2}} \left[1 + \frac{9f_{\max}}{4\pi(1-\bar{f})}\right]^{-1/2} \frac{1}{\Lambda_N^{1/2}} \tag{6.47}$$

and the effective SGS turbulent viscosity comes out as

$$\nu_N = \sqrt{\frac{7\alpha}{40}} \frac{\varepsilon^{1/3}}{\Lambda_N^{4/3}} + \frac{1.22\, f_{\max}^{1/2}}{a^{1/3}\beta^{5/6}\rho^{1/2}} \left[1 + \frac{9f_{\max}}{4\pi(1-\bar{f})}\right]^{-1/2} \frac{1}{\Lambda_N^{1/2}}. \tag{6.48}$$

The SGS eddy viscosity model given by (6.48) has a number of attractive properties:

1. The eddy viscosity depends on the liquid turbulence level through the generalized inverse temperature β. When there is a high liquid turbulence level (T large, β small) the eddy viscosity model predicts a greater momentum transfer effect associated with the bubbles. This sort of dependency of the overall turbulent bubbly flow aspect on the liquid turbulence intensity has been observed experimentally [23]. To the author's knowledge (6.48) is the only model that exhibits this property.

2. The model may be tuned by measurements in simplified situations. The principal parameters arising in the model are a and $\bar{f}$. The first reflects the repulsive behavior associated with two-bubble interactions in a laminar flow. It is much easier to carry out complete experimental measurements of the fluid flow around a configuration of two interacting bubbles than to study a general, turbulent bubbly flow. The $\bar{f}$ parameter may be measured from void distributions in turbulent bubbly flow directly. By contrast, in the previous SGS model (6.37) the λ parameter reflects a local correlation length between bubbles in turbulent flow. This is much harder to obtain from measurements and also much more likely not to be universal in nature but to depend on the overall flow boundary conditions.

The (6.48) model should form the main objective of numerical and experimental verification. A model problem solved by numerical means is presented in the next chapter. From the experimental side the most useful information would be that of the interaction of bubble pairs over a wide variety of flow regimes so that an empirical estimate of the interaction force may be educed.

Chapter 7

Direct Numerical Simulation of a Model of Turbulent Bubbly Flow

In order to test the interaction between the liquid turbulence and gas bubbles numerical simulation provides the most flexible technique. The details of the modification of the turbulent energy spectrum may be investigated in depth. In this chapter the progress achieved in carrying out such a simulation for a model problem is presented.

7.1 A model turbulent bubbly flow problem

There are at present no full numerical simulations of the interaction of turbulence in a liquid phase with a gas bubble with full tracking of the bubble surface. Most of the current direct numerical simulations of turbulent two-phase flow are oriented to particulate flows [4]. The simulations for bubbly flows are usually limited to an assumed shape for the bubble or to two-dimensional flow [10]. Given this situation it is advisable to start with the definition of a model flow problem, sufficiently simple to enable study of basic aspects of the interaction between turbulence and phase interfaces. Taking a cue from single phase turbulence simulations, the simplest problems arise when considering isotropic, homogeneous turbulence. Such a case may be simulated by solving the flow equations in a periodic box with forcing of the flow at low wave numbers. In order to include phase interface effects the standard setup is modified by the placement of a gas bubble inside the box. Since the box is periodically repeated in space, the setup corresponds to a simple model of forced, turbulent, bubbly flow.

In order to enable comparison and overall validation of the procedures with the known results from single phase flow the parameters of the simulation are chosen to be identical to those from [17]. The same overall numerical parameters defining the geometric domain and the low wave number forcing are used as surmised in the following table (see [17], Table 1)

Re_λ	L	L/λ	L/η
35.1	1.97	2.55	30
61.1	1.76	3.34	52
94.1	1.37	4.39	84

The Reynolds number used here is defined in terms of the Taylor microscale λ, $\mathrm{Re}_\lambda = U\lambda/\nu$ and η is the Kolmogorov scale $\eta = (\nu^3/\varepsilon)^{1/4}$. The forcing is achieved by using a negative viscosity coefficient for the low wavenumbers $k = |\mathbf{k}| \leq 2.5$ [17]. The main difference from the single phase simulation of Jimenez et al. [17] is the placement of a bubble in the turbulent flow field. The bubble diameter a may be varied. The ratios of bubble size to Taylor microscale ratios $a/\lambda = 1, 10, 100$ have been attempted. A visual depiction of the test problem is presented in fig. 7.1.

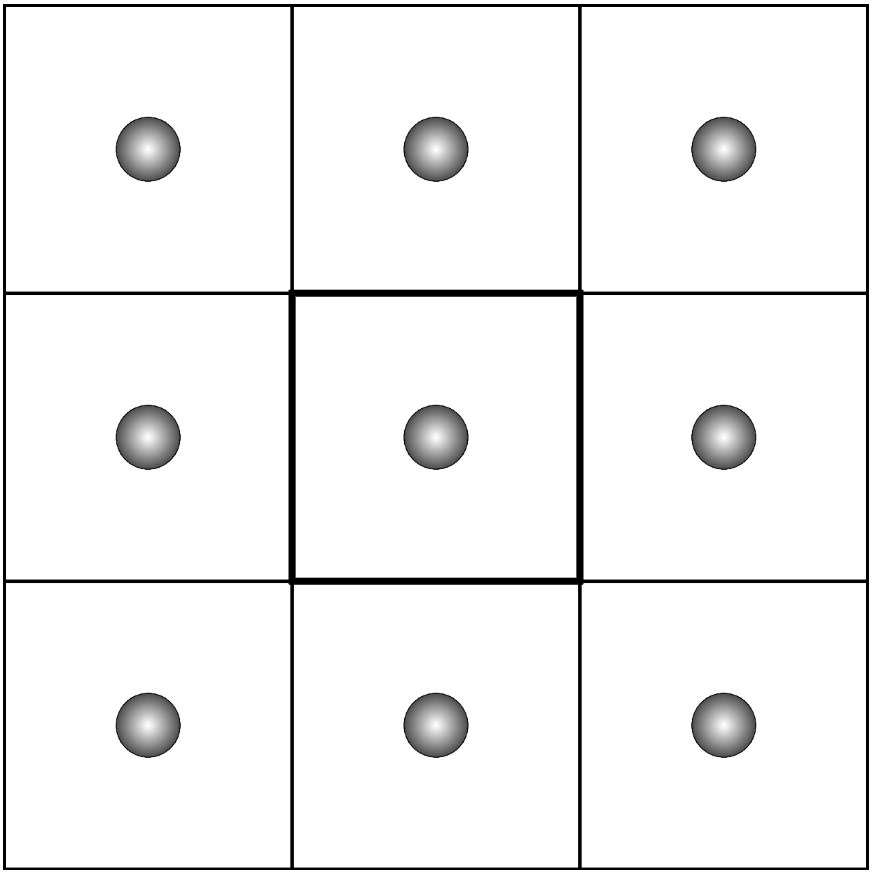

Figure 7.1: A model problem for the study of turbulence - phase interface interactions.

7.2 Overview of numerical techniques applied in OCTLES

For the solution of the above model problem a modification of the OCTLES code is used. OCTLES is a research code intended as a test-bed for various numerical techniques. It includes the following features:

- truly multi-dimensional discretization procedures;
- application of different sets of conservation laws on computational subdomains;
- dynamically adaptive, unstructured grids.

The possibility of dynamic adaptation of the grid to the motion of the bubble interface makes OCTLES an attractive technique for the study of the problem of interaction of turbulence with phase interfaces. The possibility of applying different sets of conservation laws to different subdomains is used in order to solve the standard conservation equations for the gas phase and a pseudo-compressibility formulation for the liquid phase. A summary of the numerical techniques applied in OCTLES is now presented. In addition, in appendix C essential features of OCTLES data structure and procedures are given.

7.2.1 Multidimensional discretization procedures

Most of the numeric techniques applied to multidimensional flow simulations are first obtained by analysis in an 1D setting. Common examples include upwinding, TVD schemes, ENO schemes. They are generally extended to multi-dimensional flow by applying the relevant discretization formulas along each coordinate direction. This procedure is known as *dimensional splitting.* It is known [38] that this procedure induces spurious oscillations in the numerical solution. This may be exemplified on the simpler case of the 2D Euler equations

$$\mathbf{q}_t + \mathbf{A}\mathbf{q}_x + \mathbf{B}\mathbf{q}_y = 0 \tag{7.1}$$

$$\mathbf{q} = \begin{bmatrix} \rho & u & v & p \end{bmatrix}^T \tag{7.2}$$

$$\mathbf{A} = \begin{bmatrix} u & \rho & 0 & 0 \\ 0 & u & 0 & 1/\rho \\ 0 & 0 & u & 0 \\ 0 & c^2\rho & 0 & u \end{bmatrix}, \mathbf{B} = \begin{bmatrix} v & 0 & \rho & 0 \\ 0 & v & 0 & 0 \\ 0 & 0 & v & 1/\rho \\ 0 & 0 & c^2\rho & v \end{bmatrix} \tag{7.3}$$

with c the sound velocity. All practical numerical methods for solving the above equations use some sort of local linearization. The local behavior of the numerical scheme may therefore be theoretically analyzed in terms of the Fourier decomposition with frozen matrix coefficients $\mathbf{A}, \mathbf{B}$. If we seek wave like (Fourier mode) solutions

$$\mathbf{q} = \mathbf{r} \exp\left\{ i(\mathbf{k} \cdot \mathbf{x} - \lambda t) \right\} \tag{7.4}$$

the following eigenvalue problem is obtained

$$\left(k_x \mathbf{A} + k_y \mathbf{B} \right) \mathbf{r} = \lambda \mathbf{r}$$

with the well known solution $\lambda^e = \lambda^s = k_x u + k_y v$, $\lambda^{a\pm} = k_x u + k_y v \pm c$

$$\mathbf{r}^e = (1, 0, 0, 0)^T; \quad \mathbf{r}^s = (0, -k_y, k_x, 0)^T; \quad \mathbf{r}^{a\pm} = (\rho, \pm k_x c, \pm k_y c, \rho c^2)^T. \tag{7.5}$$

The above eigenvectors depend on the direction upon which the Jacobian matrices $\mathbf{A}, \mathbf{B}$ are projected. In a dimensionally split method the $(k_x, k_y) = (1, 0)$ and $(k_x, k_y) = (0, 1)$ directions are used. Roe [38] showed how this procedure leads to non-physical modes. Consider the propagation of an acoustic mode that is not aligned with the grid in the step where x derivatives are taken. No matter what particular numerical method is used, the acoustic mode is described in terms of the eigenvectors associated with the $(k_x, k_y) = (1, 0)$ direction

$$\begin{bmatrix} \rho \\ k_x c \\ \boxed{k_y c} \\ \rho c^2 \end{bmatrix} = \underbrace{\alpha^e \begin{bmatrix} 1 \\ 0 \\ 0 \\ 0 \end{bmatrix} + \alpha^s \begin{bmatrix} 0 \\ 0 \\ \boxed{1} \\ 0 \end{bmatrix} + \alpha^{a+} \begin{bmatrix} \rho \\ c \\ 0 \\ \rho c^2 \end{bmatrix} + \alpha^{a-} \begin{bmatrix} \rho \\ -c \\ 0 \\ \rho c^2 \end{bmatrix}}_{(k_x, k_y) = (1, 0)}.$$

It is apparent that the only way of satisfying the above equation is for $\alpha^s \neq 0$. This implies the acoustic wave is described by the numerical scheme as a combination of acoustic and shear modes ($\alpha^s \neq 0$). The shear mode is non-physical. It is a numerical artefact produced by dimensional splitting.

7.2.2 Residual distribution schemes

OCTLES utilizes a class of discretization methods that include true multidimensional flow physics. The schemes are specially adapted to a geometric discretization into simplicial elements, triangles in 2D, tetrahedra in 3D. A piecewise linear representation of the flow variables along each simplicial element is used. The flow variables are stored at each node. The piecewise linear representation along each cell allows an exact formulation [38] of the linearized time evolution problem as the superposition of waves corresponding to the eigenmodes of the convective part of the flow equations. The wave propagation directions may be oriented at arbitrary directions in the cell thus allowing true multidimensional transmission of information in a time step. This is sometimes too costly in terms of computer time and a simplified, partially multidimensional approach may be used whereby the residue over a cell is distributed to the cell nodes in accordance with some scheme reflecting the true wave propagation direction. [15]

The basic idea in one dimension

Following [6] we present the basic ideas underlying the residual distribution approach for the simplified, one-dimensional conservation law

$$q_t + F_x = 0. \tag{7.6}$$

Let $c = F_q$ be the propagation velocity. Considering an initially piecewise linear approximation a wave type solution for each cell $[x_i, x_{i+1}]$ of measure $\Delta x_{i+1/2} = x_{i+1} - x_i$ may be defined by

$$q\left(x,t\right) = q_i^n + \frac{q_{i+1}^n - q_i^n}{x_{i+1} - x_i}\left(x - x_i - \bar{c}\left(t - t^n\right)\right), \tag{7.7}$$

with $\bar{a}$ some average velocity over the considered computational cell. Taking $t = t^{n+1} = t^n + \Delta t$, we obtain

$$q_i^{n+1} = q_i^n + \frac{\Delta t}{\Delta x_i}\left(\beta_{i+1/2}^i \Phi_{i+1/2} + \beta_{i-1/2}^i \Phi_{i-1/2}\right), \tag{7.8}$$

with $\Delta x_i = \frac{1}{2}\left(\Delta x_{i+1/2} + \Delta x_{i-1/2}\right)$ the i node median cell and $\Phi_{i+1/2}$ the residue on cell $i + 1/2$ defined by

$$\Phi_{i+1/2} = -\bar{c}\left(q_{i+1}^n - q_i^n\right). \tag{7.9}$$

The distribution coefficients β are defined in accordance with a physical analysis of the domains of influence and dependence

$$\begin{aligned} &\beta_{i+1/2}^i = 0 \text{ and } \beta_{i+1/2}^{i+1} = 1 \text{ if } \bar{c} \geq 0 \\ &\beta_{i+1/2}^i = 1 \text{ and } \beta_{i+1/2}^{i+1} = 0 \text{ if } \bar{c} < 0, \end{aligned} \tag{7.10}$$

which leads to a scheme identical to that of standard upwinding

$$q_i^{n+1} = q_i^n - \frac{\Delta t}{\Delta x}\left[\bar{c}_{i+1/2}^{-}\left(q_{i+1}^n - q_i^n\right) + \bar{c}_{i-1/2}^{+}\left(q_i^n - q_{i-1}^n\right)\right]. \tag{7.11}$$

The difference is that the above procedure has a natural generalization to multi-dimensional flow whereas simple upwinding is usually implemented in a split flux formulation based upon the coordinate axes.

2D Euler equations

Consider now a discretization of the flow domain into triangles. The equivalent of 7.8 for the 2D Euler equations is

$$q_i^{n+1} = q_i^n + \frac{\Delta t}{S_i}\sum_T \beta_T^i \Phi_T \tag{7.12}$$

with the sum running over all triangles that share the vertex i. The surface of area S_i is the dual median cell surrounding a node.

The distribution coefficients β must satisfy

$$\sum_{j=1}^{3} \beta_T^j = 1 \tag{7.13}$$

a generalization of 7.10. The residual (or fluctuation) is defined by

$$\Phi_T = -\oint\limits_{\Gamma_T} \vec{F} \cdot \vec{n} d\vec{l} = -\int\limits_{S_T} \vec{\nabla} \vec{F}\left(u\left(\vec{x}\right)\right) ds\,. \tag{7.14}$$

Using a constant Jacobian matrix over a cell we have

$$\Phi_T = -S_T \vec{\vec{A}} \vec{\nabla} q = -\sum_{i=1}^{3} K_i q_i \tag{7.15}$$

with

$$K_i = \frac{1}{2} \vec{\vec{A}} \vec{n}_i, \tag{7.16}$$

and $\vec{n}_i$ the inward pointing normal opposite to node i.

Any given residual distribution scheme is specified by a choice of the β_i coefficients subject to restriction 7.13. A typical choice is the N scheme, used in this investigation, for which the β coefficients are given by

$$\beta_T^i = \frac{\gamma_T^i}{\Phi_T}, \ \sum_{j=1}^{3} \gamma_T^{i(j)} = \Phi_T, \tag{7.17}$$

with γ_T^i linear functions of q defined by

$$\gamma_T^i = \frac{K_i^+}{\sum\limits_{j=1}^{3} K_j^+} \sum_{j=1}^{3} \left[K_j^- \left(q_i^n - q_j^n\right)\right]. \tag{7.18}$$

The physical interpretation of the N scheme is the decomposition of each inflowing eigenmode along the cell edges. There may be two or only one downstream node. If there is only one, then that node receives the entire fluctuation associated with the considered eigenmode. If there are two downstream nodes the fluctuation is split proportionally to the decomposition of the wave vector along the cell edges.

The above scheme is of first order. It may be made of formal second order by the use of limiters [32]. All of the standard limiters (Super Bee, Albado, etc.) may be applied in conjunction with the above formulation.

Viscosity effects

Viscosity effects do not affect the basic multidimensional splitting procedure presented above. These effects are included using a standard Galerkin formulation in the computation. To ease notation we present the procedure as applied to the simple scalar diffusion equation

$$\frac{\partial u}{\partial t} + \vec{\lambda} \cdot \nabla u = \nu \Delta u. \tag{7.19}$$

The procedure may be easily extended to the full Navier-Stokes equations.

Integrating over a control volume (the dual median cell) Ω we obtain

$$\int_\Omega \frac{\partial u}{\partial t} \omega_i d\Omega + \int_\Omega \vec{\lambda} \cdot \nabla u \omega_i d\Omega = \int_\Omega \nu \Delta u \omega_i d\Omega \tag{7.20}$$

with ω a weight function describing the residual procedure presented above. In order to eliminate the second order derivative (inappropriate in as much as we are using a piecewise linear representation of the flow variables) we integrate by parts

$$\int_\Omega \frac{\partial u}{\partial t} \omega_i d\Omega + \sum_T \int_T \vec{\lambda} \cdot \nabla u \omega_i d\Omega = \oint \omega \frac{\partial u}{\partial n} d\partial\Omega - \sum_T \nu \int_T \nabla \omega_i \cdot \nabla u d\Omega. \tag{7.21}$$

The viscosity term contains now only first order derivatives. We introduce a Galerkin representation for the viscous term

$$u = \sum u_i N_i \tag{7.22}$$

where N_i are the standard shape functions associated with linear interpolation over a cell.

Modifications for the liquid phase

The fluctuation distribution schemes described above are appropriate for compressible flows. The compressibility of the liquid phase for the model problem considered here is very low. In order to overcome the stiffness associated with this term the standard technique of pseudo-compressibility is used [13, 23.3.2] with the continuity equation for the liquid phase being written as

$$\frac{1}{\beta^2} \frac{\partial^2 P}{\partial t^2} + \nabla \cdot \mathbf{U} = 0\,. \tag{7.23}$$

7.3 Initial results

At the time this report was written the full simulation of the interaction of a bubble array with the liquid turbulence was not completed. Problems with the interface tracking procedure have not yet allowed the runs to be conducted for sufficiently long times in order to accumulate the statistics required for analysis of the turbulent flow field. Snapshots of the instantaneous flow before a breakdown in the tracking procedure occurs have been obtained though. A typical result, for the first test case of the model problem is presented in fig. 7.2.

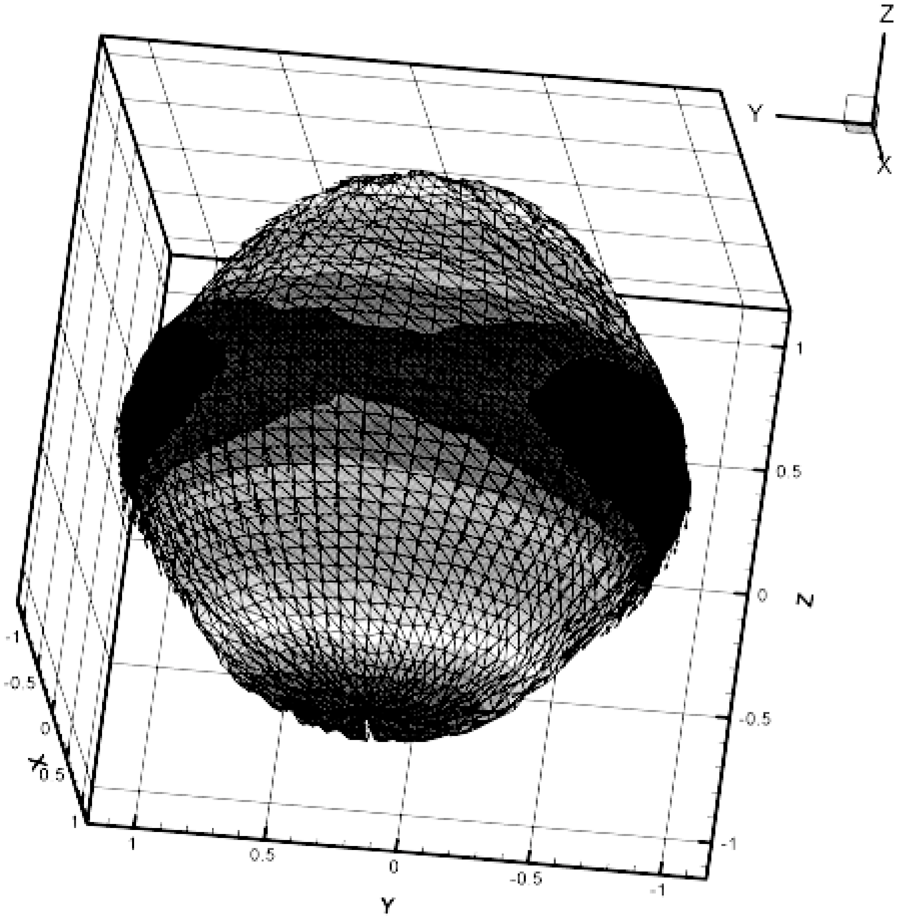

Figure 7.2: Typical snapshot of the flow on a gas bubble immersed in a liquid. The contour lines on the bubble indicate pressure levels. Velocity vectors on the bubble surface are also represented.

Part III

Local Thermodynamic Analysis of Phase Interface Formation

Chapter 8

Considerations on interface reconstruction procedures

A number of computational procedures for multiphase flow use an additional field in order to determine the phase interface. The VOF method uses a transport equation for the void fraction f while the Level Set Method uses an additional function g whose null lines determine the interface. In both of these cases the evolution in time of the interface is assumed to be given by the local advection velocity, so the Navier-Stokes equations determine this advection process.

However, the processes involved in phase interface formation are molecular. The scales of motion involved are not included in the Navier-Stokes equations. Since the Navier-Stokes equations may be obtained by the first order expansion of the Boltzmann kinetic equation, we may say that the relevant scales of motion for interface formation have been averaged out of the Navier-Stokes equations. It is, therefore, not to be expected that the interface shapes predicted by advection imposed by the Navier-Stokes equations is the true physical interface since the physical processes involved in interface formation are not captured.

This type of situation has been met before in fluid dynamics computations in connection with the computation of shock waves in gas dynamics. There also the shock wave internal structure depends on the motion of gas molecules on scales of motion averaged out of the Navier-Stokes equations. In order to obtain correct shock behavior additional constraints are imposed on the numeric approximations, such as the entropy condition [13].

8.1 The MFEIR Algorithm

Given the existent experience with the treatment of shock waves in gas dynamics it is natural to inquire how an interface reconstruction procedure that includes physical information lacking in the Navier-Stokes equations themselves may be constructed. The main aspect neglected is the energetics of interface formation. But we know that locally the interface shall always assume a shape in which the free energy is minimized [36], [7].

The Minimum Free Energy Interface Reconstruction Algorithm (MFEIR) is defined so that local patches of the interface minimize the surface free energy. The algorithm uses a piecewise spline approximation of the surface. The degree of the spline approximation is chosen so that information available from the underlying VOF procedure may be used and also that conditions of minimum free energy may be imposed. The data from the VOF method are typically a set of normal vectors $\mathbf{n}_i$ and their application points $\mathbf{b}_i$ defining a tangent plane to the surface at a particular point. Since the points $\mathbf{b}_i$ are not necessarily ordered a non-uniform rational basis spline (or NURBS) is the best suited type of spline approximation

$$\mathbf{S}^w(u,v) = \sum_{j=0}^{1}\sum_{k=0}^{1} N_j^p(u) N_k^p(v)\mathbf{b}_{j,k}^w \tag{8.1}$$

where

$$u \in \{\underbrace{a \ \cdots \ a}_{p+1};\underbrace{b \ \cdots \ b}_{p+1}\},\ v \in \{\underbrace{c \ \cdots \ c}_{p+1};\underbrace{d \ \cdots \ d}_{p+1}\} \tag{8.2}$$

and $N_j^p(u)$ is the standard normal basis function of degree p.

The conditions imposed on the surface are:

1. that it have the normals specified by the VOF procedure

$$\left(\frac{\dfrac{\partial \mathbf{S}^w}{\partial u} \times \dfrac{\partial \mathbf{S}^w}{\partial v}}{\left\|\dfrac{\partial \mathbf{S}^w}{\partial u} \times \dfrac{\partial \mathbf{S}^w}{\partial v}\right\|}\right)_i = \mathbf{n}_i \tag{8.3}$$

2. that the free energy of the surface is at a stationary (minimal) value

$$\delta f^\sigma = \delta u^\sigma - T\delta s^\sigma = 0. \tag{8.4}$$

The second condition is variational in nature. It can therefore be used to determine as many parameters of the NURBS surface as desired. If we do not consider any heat transfer, chemical or phase transition effects we have

$$\delta s^\sigma = 0 \tag{8.5}$$

and therefore

$$\delta f^\sigma = \delta u^\sigma . \tag{8.6}$$

The internal energy may be computed as the work done to deform the surface

$$\delta u^\sigma = -\delta w \tag{8.7}$$

with

$$w = \frac{\sigma}{A}\iint \frac{(R_1+R_2)z}{R_1R_2} dxdy\,. \tag{8.8}$$

8.2 Comparisons with other Interface Reconstruction Algorithms

The MFEIR algorithm is currently being implemented so detailed comparisons with other reconstruction procedures have not been obtained at the time of this report. However, from the theoretical point of view we may observe that:

1. it provides a rational means of carrying out higher order reconstruction of a phase interface as opposed to the zero or first order reconstruction procedures commonly encountered at present (e.g. the FLAIR algorithm [1]);
2. it includes physical effects typically neglected in interface tracking or reconstruction procedures namely the condition of local minimum free energy;
3. it is extendable to include phase transition and chemical effects.

Part IV

Conclusions

This investigation has concentrated on the means whereby closures for the large-scale computation of bubbly flow may be obtained. The two principal closure problems that have been considered are:

1. The effect of the momentum drift flux term (1.5);
2. The effect of subgrid scale momentum transfer due to turbulence effects modeled in the VOF computation by a subgrid scale stress term.

For the first closure problem two methods have been studied. The main conclusions regarding these models may be stated as follows.

1. *The viscid-inviscid axisymmetric bubble model.* This model provides an estimate of the magnitude of the MDF term in the simplified case of a bubble placed in an uniform flow. Parameter variations (Weber, Reynolds numbers) may allow a correlation to be devised in which the order of magnitude effects of the MDF term are captured. The basic limitation of the model is the restriction to simple flow conditions around the bubble, i.e. bubble placed in an uniform flow. This limits the applicability to devising an MDF model for turbulent flow.
2. *The dynamic momentum drift-flux model.* In this model the true, turbulent flow field around a model is taken into account. The model modifies the vorticity field of the volume of fluid computation to account for under-resolved boundary conditions on the bubble surface. The model uses fast Poisson solvers in order to ensure computational efficiency. The model may be applied in one of two fashions:
    (a) by disregarding the condition that a bubble should be a stream surface at the subgrid scale level. This leads to an acceptable computational effort, suitable for inclusion as a correction of each time step of the VOF computation.
    (b) by imposing the stream surface condition. This requires solving an additional integral equation on the bubble surface which usually leads to unacceptably large computational time penalties in the context of a turbulent VOF computation. The procedure is suitable for achieving greater precision in simpler flows though.

In order to achieve some progress on the second closure problem, a statistical thermodynamic treatment of dilute bubbly flow has been proposed. In this approach the bubble interactions are modeled through hydrodynamic potentials. The general results of kinetic theory and statistical hydrodynamics allow estimates of the additional momentum transfer associated with the presence of the bubbles. The additional momentum transfer is included in the flow equations for the liquid through an additional viscosity coefficient. The equations are then subjected to a renormalization group procedure in order to devise subgrid scale turbulence models.

Two procedures are studied for the construction of SGS models for dilute bubbly flow. The first, which uses measured turbulence energy spectra, requires information about the local correlation length of the bubbles' motion, a quantity difficult to obtain from experiments. The second, which uses the results of the statistical treatment of the bubbles, furnishes an expression for the turbulent eddy viscosity with a number of desirable features. These include a dependence on the overall liquid turbulence intensity level and the possibility of tuning the model constants from measurements of bubble interactions in laminar flow, much easier to set up experimentally. Some suggestions for experiments needed for verifying the model coefficients have been presented.

In order to verify the predictions of this approach a model problem involving a bubble placed in a periodically repeated box has been defined. The progress on carrying out a full DNS simulation while tracking the bubble boundary has been presented. This computation is not complete at present.

Finally some considerations on the algorithms used in interface reconstruction are presented. It is argued that a rational reconstruction procedure should include a formulation of the energetics of the process. A procedure has been proposed in which the interface is reconstructed in accordance with the physical criterion of minimization of the surface free energy.

Appendix A

Partition over Cartesian grid algorithms

A common problem that arises in numerical descriptions of bubbly flow is the partition of a bubble over grid cells. A few efficient algorithms for the partitioning of convex shapes over a Cartesian grid are presented here.

A.1 The two-dimensional case

A 2D Cartesian grid cell is denoted by $C_{ij} = [x_i, x_{i+1}] \times [y_j, y_{j+1}]$. It has the area $D_{ij} = (x_{i+1} - x_i)(y_{j+1} - y_j)$. We introduce the indicator function f_{ij} of C_{ij} which is equal to 1 for $(x, y) \in C_{ij}$ and zero otherwise. Let S_{ij} be the area of the convex body S within C_{ij}. There are many relative positions of an arbitrary cell C_{ij} with respect to S (as may be seen by observing fig. A.1). Rather than treat each case separately it is preferable to reduce the problem to a simpler one suggested by the expansion of the indicator function of C_{ij}.

The indicator function may be expressed in terms of the Heaviside step function $H(x)$ as

$$f_{ij}(x, y) = [H(x - x_i) - H(x - x_{i+1})]\,[H(y - y_j) - H(y - y_{j+1})] \tag{A.1}$$

which, when expanded, gives

$$f_{ij}(x, y) = H(x - x_i)H(y - y_j) - H(x - x_{i+1})H(y - y_j) - \tag{A.2}$$
$$H(x - x_i)H(y - y_{j+1}) + H(x - x_{i+1})H(y - y_{j+1})\,. \tag{A.3}$$

This formula may be interpreted as specifying how to combine areas in the first quadrant relative to the point (x_i, y_j) so as to obtain C_{ij}. Let Q_{ij} be the area in the first quadrant of the point (x_i, y_j). We assume that there exists a cutoff at the grid boundaries defined by $x = x_M$, $y = y_N$, so that the areas Q_{ij} are finite. The area addition formula for D_{ij} derived from (A.2) is

$$D_{ij} = Q_{ij} - Q_{i+1,j} - Q_{i,j+1} + Q_{i+1,j+1} \tag{A.4}$$

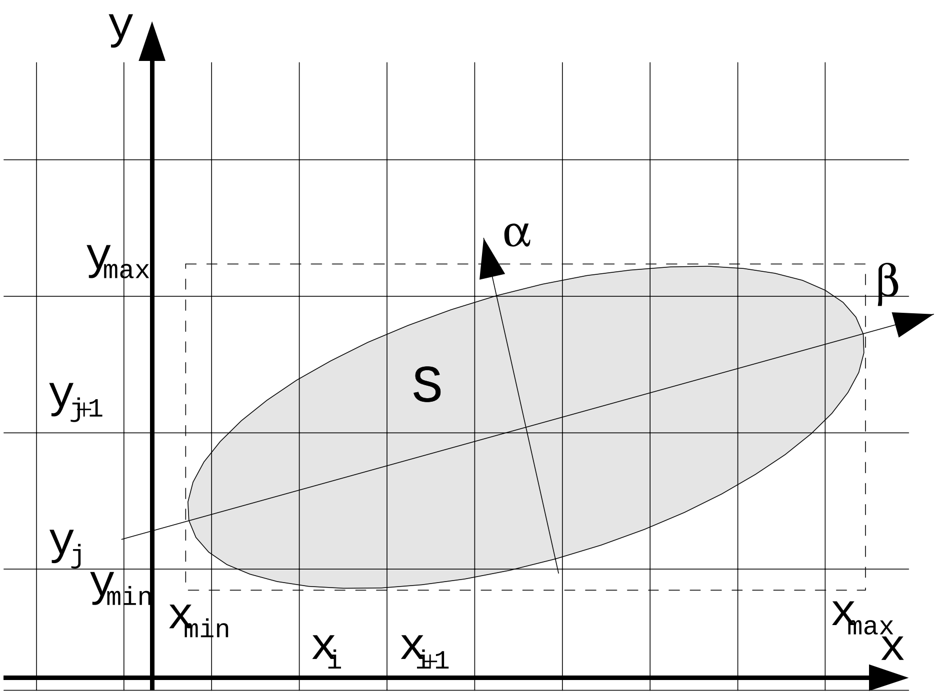

Figure A.1: A depiction of the grid partition problem.

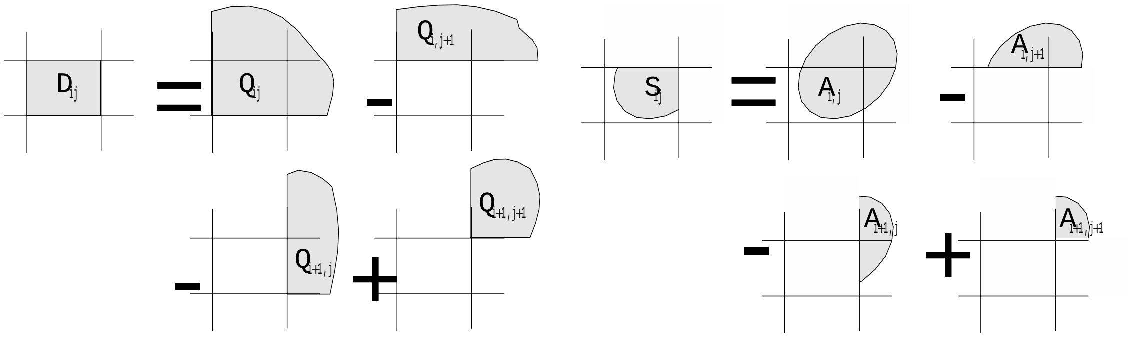

Figure A.2: Depiction of the area addition formulas (A.4) and (A.5).

which has the pictorial depiction represented in fig. A.2.

This suggests that we introduce the area of S in the first quadrant relative to point (x_i, y_j) which we denote by A_{ij}. The formula analogous to (A.4) is

$$S_{ij} = A_{ij} - A_{i+1,j} - A_{i,j+1} + A_{i+1,j+1} \,. \tag{A.5}$$

There are nine possible relative positions between a convex body and the axes that form the first quadrant of the plane. These are depicted in fig. A.3. Only four of these have a non-zero part of the body inside the first quadrant, so we have five distinct cases:

1. $x_i \leq x_{\min}$ and $y_j \leq y_{\min}$ for which $A_{ij} = S$
2. $x_{\min} < x_i \leq x_{\max}$ and $y_j \leq y_{\min}$
3. $x_i \leq x_{\min}$ and $y_{\min} < y_j \leq y_{\max}$
4. $x_{\min} < x_i \leq x_{\max}$ and $y_{\min} < y_j \leq y_{\max}$
5. $x_{\max} < x_i$ or $y_{\max} < y_j$ for which $A_{ij} = 0$

In cases 2 and 3 there are two, while in case 4 there are four intersection points between the $x = x_i$, $y = y_j$ axes and S. Let $\{x = x(s),\, y = y(s)\}$ be the natural parametrization of the boundary of S. Denote by s_k the arc coordinates of the intersection points of S with the axes and assume $s_{k+1} \geq s_k$. We introduce the notation $x^{(k)} = x(s_k)$, $y^{(k)} = y(s_k)$.

We now compute A_{ij}. This may be done through an area integral, but it is more convenient to transform this into a contour integral using the divergence theorem

$$\iint_S \nabla \cdot \vec{V}\, dS = \oint_{\partial S} \vec{V} \cdot \vec{n}\, ds \tag{A.6}$$

for the field $\vec{V} = (x\vec{i} + y\vec{j})/2$. The unit vector $\vec{n}$ is the outward normal to the boundary of S and is given by

$$\vec{n}(s) = \frac{y'(s)\vec{i} - x'(s)\vec{j}}{\sqrt{[x'(s)]^2 + [y'(s)]^2}} \tag{A.7}$$

where it is assumed that as s increases the interior of S is always on the left-hand side. The areas A_{ij} for the four non-zero cases considered above are as follows.

1.

$$A_{ij} = \frac{1}{2}\int_0^p \frac{x(s)y'(s) - y(s)x'(s)}{\sqrt{[x'(s)]^2 + [y'(s)]^2}}\, ds \,, \tag{A.8}$$

with p denoting the perimeter of S.

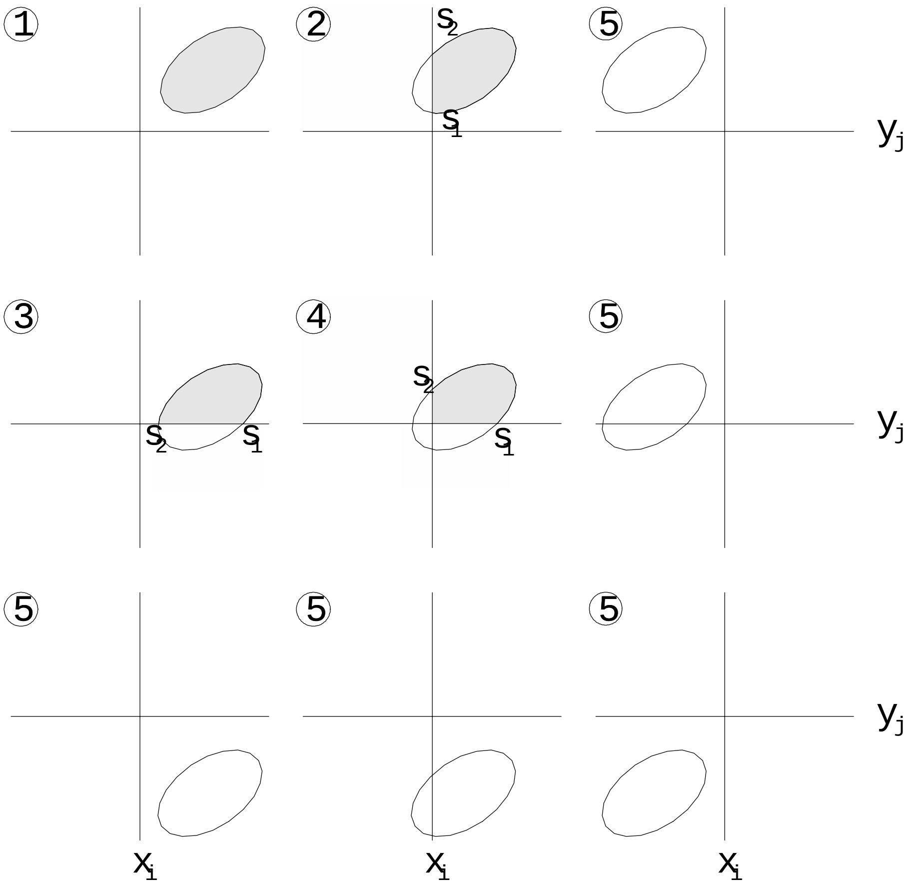

Figure A.3: Possible relative positions of a convex body with respect to the first quadrant.

2.

$$A_{ij} = \frac{1}{2}\int_{s_1}^{s_2} \frac{x(s)y'(s) - y(s)x'(s)}{\sqrt{[x'(s)]^2 + [y'(s)]^2}} ds \, + \frac{x_i}{2}\left(y^{(1)} - y^{(2)}\right) \, . \tag{A.9}$$

3.

$$A_{ij} = \frac{1}{2}\int_{s_1}^{s_2} \frac{x(s)y'(s) - y(s)x'(s)}{\sqrt{[x'(s)]^2 + [y'(s)]^2}} ds \, + \frac{y_j}{2}\left(x^{(2)} - x^{(1)}\right) \, . \tag{A.10}$$

4. We may identify a number of subcases, depending on the position of the intersection points $(x^{(k)}, y^{(k)})$ with respect to (x_i, y_j). Let $k = 1, 4$ correspond to the intersections of S with the $y = y_j$ axis and $k = 2, 3$ to those of S with the $x = x_i$ axis and assume $x^{(1)} \geq x^{(4)}$ and $y^{(2)} \geq y^{(3)}$.

   (a) $y^{(2)}, y^{(3)} > y_j$ and $x^{(1)}, x^{(4)} < x_i$. This reduces to case 2.

   (b) $x^{(1)}, x^{(4)} > x_i$ and $y^{(2)}, y^{(3)} < y_j$. This reduces to case 3.

   (c) $y^{(2)}, y^{(3)} > y_j$ and $x^{(1)}, x^{(4)} > x_i$ (fig. A.4).

$$A_{ij} = \frac{1}{2}\int_{s_1}^{s_2} \frac{x(s)y'(s) - y(s)x'(s)}{\sqrt{[x'(s)]^2 + [y'(s)]^2}} ds \, + \frac{y_j}{2}\left(x^{(4)} - x^{(1)}\right) + \tag{A.11}$$

$$\frac{1}{2}\int_{s_3}^{s_4} \frac{x(s)y'(s) - y(s)x'(s)}{\sqrt{[x'(s)]^2 + [y'(s)]^2}} ds \, + \frac{x_i}{2}\left(y^{(3)} - y^{(2)}\right) \, . \tag{A.12}$$

   (d) $y^{(2)} \geq y_j \geq y^{(3)}$ and $x^{(1)} \geq x_i \geq x^{(4)}$.

$$A_{ij} = \frac{1}{2}\int_{s_1}^{s_2} \frac{x(s)y'(s) - y(s)x'(s)}{\sqrt{[x'(s)]^2 + [y'(s)]^2}} ds \, + \frac{x_i}{2}\left(y_j - y^{(2)}\right) + \frac{y_j}{2}\left(x_i - x^{(1)}\right) \, . \tag{A.13}$$

   (e) $x^{(1)} \leq x_i$ and $y^{(2)} \leq y_j$. This gives a zero contribution (case 5).

A.1.1 Example: partition of an ellipse

The parametric representation of an ellipse of semi-axes a, b, centered at (x_C, y_C) with the a axis at angle ψ from the x axis is

$$x(\theta) = x_C + a\cos\theta\cos\psi - b\sin\theta\sin\psi \tag{A.14}$$

$$y(\theta) = y_C + a\cos\theta\sin\psi + b\sin\theta\cos\psi \, . \tag{A.15}$$

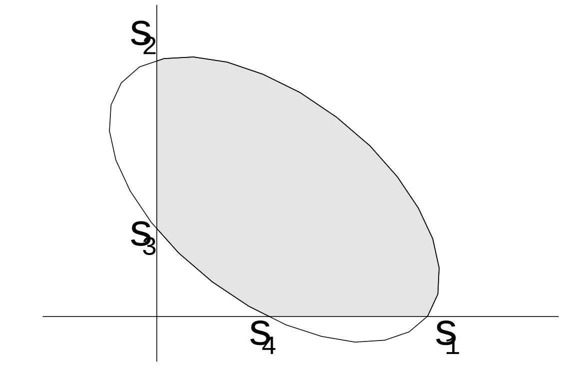

Figure A.4: Subcase 4b, four intersection points between the convex body S and the axes.

In order to apply formulas (A.8)-(A.11) we need to compute the natural parameter integral along an arbitrary arc from θ_M to θ_N (or s_M to s_N in terms of the natural parameter)

$$I(\theta_M, \theta_N) = \frac{1}{2}\int_{s_M}^{s_N} [x(s)n_x(s) + y(s)n_y(s)]\, ds \tag{A.16}$$

$$= \frac{1}{2}\int_{\theta_M}^{\theta_N} [x(\theta)n_x(\theta) + y(\theta)n_y(\theta)]\, \frac{ds}{d\theta} d\theta\,. \tag{A.17}$$

From $(ds)^2 = (dx)^2 + (dy)^2$ we obtain $ds = \left(a^2\sin^2\theta + b^2\cos^2\theta\right)^{1/2} d\theta$. The outward-pointing, unit normal vector is

$$\vec{n}(\theta) = \frac{(-a\sin\psi\sin\theta + b\cos\psi\cos\theta)\,\vec{i} + (a\cos\psi\sin\theta + b\sin\psi\cos\theta)\,\vec{j}}{\left(a^2\sin^2\theta + b^2\cos^2\theta\right)^{1/2}}. \tag{A.18}$$

The integral may be evaluated analytically, and we obtain

$$I(\theta_M, \theta_N) = \frac{1}{2}\left[a(\cos\theta_N - \cos\theta_M)(x_C\sin\psi - y_C\cos\psi) + \right. \tag{A.19}$$

$$\left. b(\sin\theta_N - \sin\theta_M)(x_C\cos\psi + y_C\sin\psi) + ab(\theta_N - \theta_M)\right]\,. \tag{A.20}$$

The positions along the ellipse corresponding to $x_{\max}$, $x_{\min}$ may be determined from $x'(\theta) = 0$ which leads to $\tan\theta = -(b/a)\tan\psi$. Likewise $\tan\theta = (b/a)\cot\psi$ gives the extremal y positions. Intersections of $x = const$ lines with the ellipse are determined from $x(\theta) = x_i$ and those of $y = const$ from $y(\theta) = y_j$. Both lead to a trigonometric equation of the form

$$p\cos\theta + q\sin\theta = r \tag{A.21}$$

which may be solved by introducing $\tan\varphi = p/q$ and obtaining

$$\sin(\theta + \varphi) = \frac{r}{q}\cos\varphi \Rightarrow \theta = (-1)^k \arcsin\left(\frac{r}{q}\cos\varphi\right) - \varphi + k\pi\,. \tag{A.22}$$

An example is presented in fig. A.5 for a coarse grid. Processing for a 100x100 grid and 10-20 ellipses is carried out in a few seconds on a typical Pentium PC.

A.2 The three-dimensional case

The above procedure may be readily extended to 3D. The analogue of (A.5) is

$$S_{ijk} = A_{ijk} - A_{i+1,jk} - A_{i,j+1,k} - A_{ij,k+1} + \tag{A.23}$$

$$A_{i+1,j+1,k} + A_{i+1,j,k+1} + A_{i,j+1,k+1} - A_{i+1,j+1,k+1} \tag{A.24}$$

with S_{ijk} the volume of S within the cell $C_{ijk} = [x_i, x_{i+1}] \times [y_j, y_{j+1}] \times [z_k, z_{k+1}]$, and A_{ijk} the volume of S within the first octant. There are now 27 relative positions of S with respect to an octant. Of these only 8 give a non-zero value of A_{ijk} so we obtain 9 distinct cases. Again it is easier to evaluate the volume through an equivalent surface integral, using $\vec{V} = (x\vec{i} + y\vec{j} + z\vec{k})/3 = \vec{r}/3$ in the divergence theorem. Let $\{x = x(s,t),\ y = y(s,t),\ z = z(s,t)\}$ be the natural parametrization of the boundary surface of S. The outward normal to the surface is

$$\vec{N} = \begin{vmatrix} \vec{i} & \vec{j} & \vec{k} \\ \dfrac{\partial x}{\partial s} & \dfrac{\partial y}{\partial s} & \dfrac{\partial z}{\partial s} \\ \dfrac{\partial x}{\partial t} & \dfrac{\partial y}{\partial t} & \dfrac{\partial z}{\partial t} \end{vmatrix} \tag{A.25}$$

with the unit normal vector being of course

$$\vec{n} = \frac{\vec{N}}{\left|\vec{N}\right|}. \tag{A.26}$$

Formulas involving surface integrals may be written for all the cases mentioned above. As an example, for $x_i \le x_{\min}$, $y_j \le y_{\min}$, $z_k \le z_{\min}$ we have

$$A_{ijk} = S = \frac{1}{3} \int_0^p \int_0^{q(t)} \frac{\vec{r}(s,t) \cdot \vec{N}(s,t)}{\left|\vec{N}(s,t)\right|} ds dt \tag{A.27}$$

with p the perimeter along the t natural coordinate and $q(t)$ the perimeter along the s natural coordinate for a given t. Even for simple bodies (e.g. ellipsoids) the evaluation of these integrals becomes error-prone though. We therefore turn to a procedure that may be easily automated with minimum effort.

A.3 Extensions to arbitrary bodies

Since computation of the surface integrals arising in the above algorithm is tedious for bodies of general shape, it is more convenient to apply a hybrid numerical-analytical algorithm. An arbitrary body V may be discretized into tetrahedra T_i to

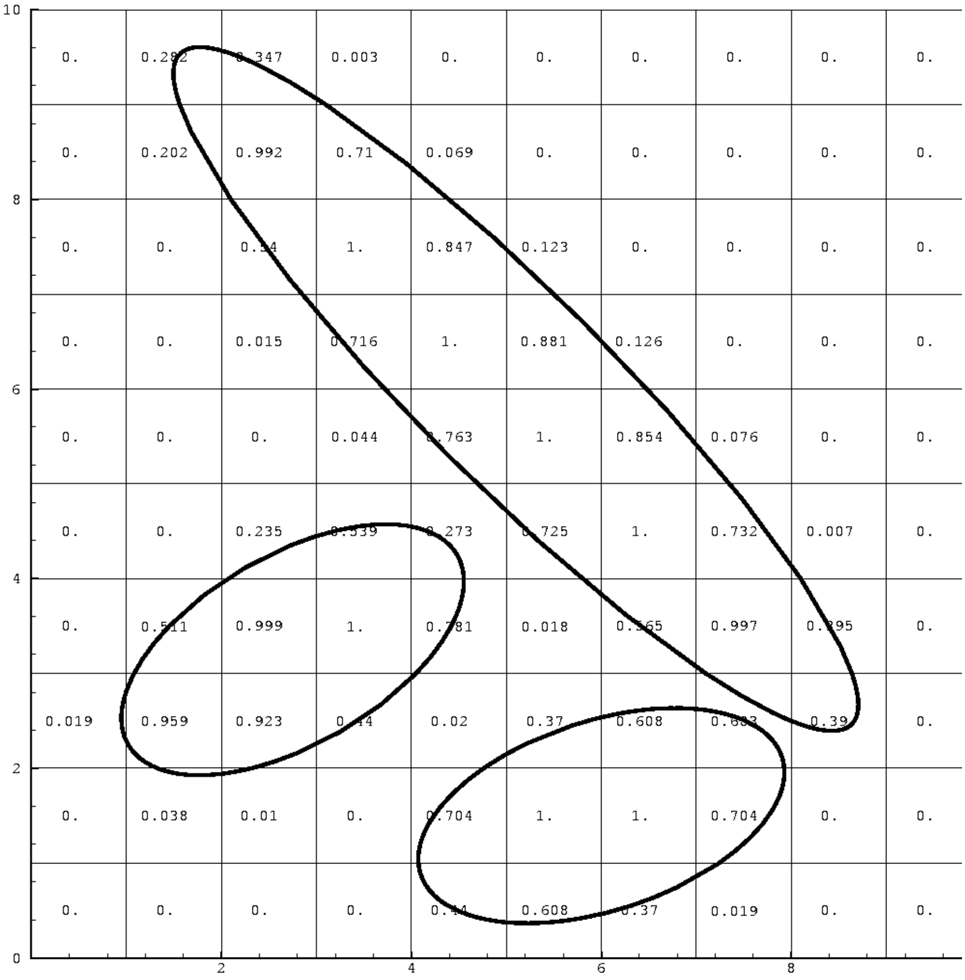

Figure A.5: Example results obtained for the partitioning of 3 ellipses $(a, b, x_c, y_c, \psi) \in \{(2, 1, 2.75, 3.25, \pi/6),\ (1, 5, 5.1, 6, \pi/4),\ (2, 1, 6, 1.5, \pi/10)\}$.

any required precision

$$V = \cup_i T_i, \tag{A.28}$$

so we need only consider the problem of partitioning of a single tetrahedron T on a Cartesian grid. By applying (A.23) the problem reduces to finding the portion of a tetrahedron in the first octant of the point (x_i, y_j, z_k). This problem may in turn be reduced to finding the portion of a tetrahedron above a plane

$$V(T; x \geq x_i, y \geq y_j; z \geq z_k) = V(T; x \geq x_i) \cap V(T; x \geq x_i) \cap V(T; x \geq x_i), \tag{A.29}$$

where $V(T; cond)$ signifies the volume of the portion of T that satisfies conditions *cond*. It is straightforward to split a tetrahedron along the intersection points with a plane to obtain smaller tetrahedrons satisfying the conditions $x \geq x_i, y \geq y_j; z \geq z_k$.

This algorithm is used in the MDFTerm program (Appendix B) to compute the void fractions corresponding to the partition of a bubble over a Cartesian grid, information that is required in the computation of the MDF term.

Appendix B

The AxiBubble program

The procedures described in chapter 2 have been implemented in an user-friendly program named AxiBubble. The source code and distribution package for this program are available on `\\IRSSERV05\IRS3\AxiBubble` (as of July 1999). A description is provided here of the general program construction, input and output data and compilation procedures. Files are referred according to the top level directory.

B.1 Main program components

AxiBubble is built from the following files:

1. `AxiBubbleEngine\AxiBubbleEngine.f90`. This Fortran 90 source file contains all of the computational procedures in AxiBubble.
2. `AxiBubbleEngine\AxiBubbleCommon.f90`. This Fortran 90 source file contains declarations for the variables in the global common area. Most of the geometric and flow data needed by the various AxiBubble routines are stored here.
3. `AxiBubbleEngine\DLLInterface.f90`. This Fortran 90 source file is the interface of the computational routines to the graphical user interface (GUI). The GUI never calls routines in `AxiBubbleEngine` directly, rather the interface routines given here.
4. `AxiBubbleEngine\GUICommon.f90`. This Fortran 90 source file contains global data for the GUI routines.
5. `AxiBubbleEngine.frm`. This Visual Basic file is the main interface to AxiBubble (fig. B.1).
6. `Dialog2.frm, Dialog3.frm, Tetra.frm, frmAbout.frm`. These Visual Basic files contain the additional dialogs in AxiBubble.
7. `AxiBubbleGlobal.bas`. This Visual Basic file contains the declarations for global data within the GUI. It also contains the calling specifications towards routines in `DLLInterface.f90`.

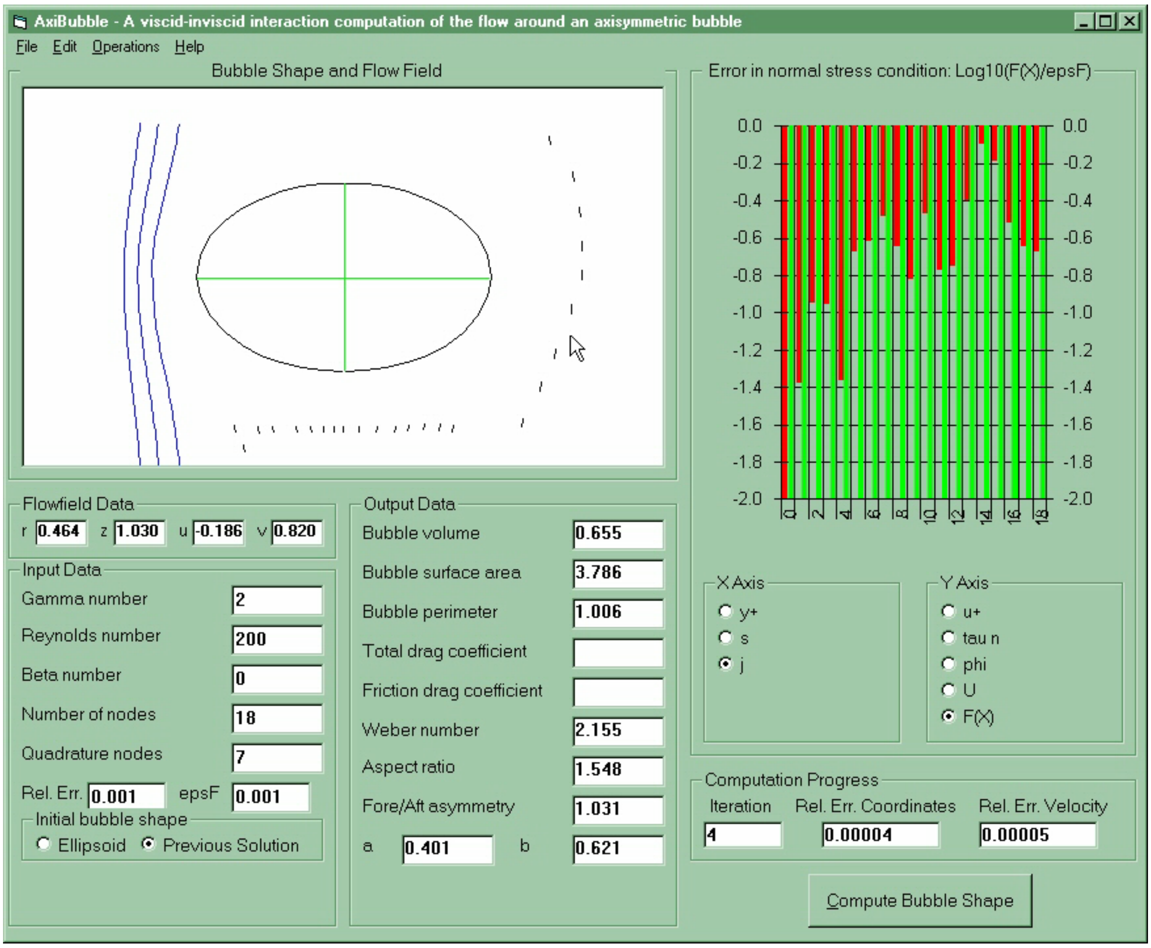

Flowfield Data
r 0.464 z 1.030 u -0.186 v 0.820

Input Data
Gamma number 2
Reynolds number 200
Beta number 0
Number of nodes 18
Quadrature nodes 7
Rel. Err. 0.001 epsF 0.001
Initial bubble shape ○ Ellipsoid ● Previous Solution

Output Data
Bubble volume 0.655
Bubble surface area 3.786
Bubble perimeter 1.006
Total drag coefficient
Friction drag coefficient
Weber number 2.155
Aspect ratio 1.548
Fore/Aft asymmetry 1.031
a 0.401 b 0.621

X Axis ○ y+ ○ s ● j
Y Axis ○ u+ ○ tau n ○ phi ○ U ● F(X)

Computation Progress
Iteration 4
Rel. Err. Coordinates 0.00004
Rel. Err. Velocity 0.00005

Figure B.1: AxiBubble graphical user interface.

B.2 Program input, output, flowchart

B.2.1 `Tetra.dat`

This file contains a tetrahedral discretization of the bubble. The file is in text format and contains the following fields:

```
nNodes nTets      - The number of nodes and of tetrahedra
x1 y1 z1          - The coordinates of the first node
...
xn yn zn          - The coordinates of the last node
i1 j1 k1 l1       - The node numbers forming the first tetrahedron
...
in jn kn ln       - The node numbers forming the last tetrahedron
```

B.2.2 `SurfTri.dat`

This file contains a triangular discretization of the bubble surface. The file is in text format and contains the following fields:

```
nNodes nTri      - The number of nodes and of triangles
x1 y1 z1         - The coordinates of the first node
...
xn yn zn         - The coordinates of the last node
i1 j1 k1         - The node numbers forming the first triangle
...
in jn kn         - The node numbers forming the last triangle
```

B.2.3 `grid.dat`

This file contains the x, y, z coordinates defining the Cartesian grid used in computing the velocity field around the bubble. The file is in text format and contains the following fields:

```
nX nY nZ         - The number of x,y,z coordinates
x1               - The first x coordinate
...
xn               - The last x coordinate
y1               - The first y coordinate
...
yn               - The last y coordinate
z1               - The first z coordinate
...
zn               - The last z coordinate
```

B.2.4 `gridvel.dat`

This file contains the velocities on the Cartesian grid surrounding a bubble. It is generated by the instructions

```
DO k=2,Nz-1
 DO j=2,Ny-1
  DO i=2,Nx-1
     WRITE(1,2004)x,y,z,Phi(i,j,k)-z,Jumps(i,j,k),u,v,w
     WRITE(2,2004)u,v,w
2004 FORMAT(7(E14.7,2x))
  END DO
 END DO
END DO
```

B.2.5 `mdfterm.dat`

This file contains the MDF tensor $\mathbf{D}$. It is output by the postprocessing utility `mdfterm`. It is provided outside of the AxiBubble program due to the large memory requirements of the computation of the f field over a Cartesian grid. The `mdfterm` utility reads the files `newtetra.dat` (similar to `tetra.dat` but with the bubble rotated and translated by user specified amounts), `grid.dat`, `gridvel.dat`, and outputs the `mdfterm.dat` file. The `mdfterm.dat` file is output by the instructions:

```
do k=2,nz-1
   zC=0.5*(zGrid(k)+zGrid(k+1))
   do j=2,ny-1
    yC=0.5*(yGrid(j)+yGrid(j+1))
    do i=2,nx-1
     xC=0.5*(xGrid(i)+xGrid(i+1))
     divDnorm=0.0
     f=part(i,j,k)
     do l=1,3
      divD(l)= &
       (D(i+1,j,k,l,1)-D(i-1,j,k,l,1))/(xGrid(i+1)-xGrid(i-1)) + &
       (D(i,j+1,k,l,2)-D(i,j-1,k,l,2))/(yGrid(j+1)-yGrid(j-1)) + &
       (D(i,j,k+1,l,3)-D(i,j,k-1,l,3))/(zGrid(k+1)-zGrid(k-1))
      divDnorm=divDnorm+divD(l)**2
     end do
     write(1,1005)xC,yC,zC,divDnorm,(divD(lD),lD=1,3), &
                 ((D(i,j,k,lD,mD),lD=1,3),mD=1,3)
1005 format(16(E14.7,2x))
    end do
   end do
  end do
```

Each line of the file contains

$$x, y, z, \|\nabla\cdot\mathbf{D}\|, (\nabla\cdot\mathbf{D})_x, (\nabla\cdot\mathbf{D})_y, (\nabla\cdot\mathbf{D})_y, \tag{B.1}$$

$$\mathbf{D}_{xx}, \mathbf{D}_{yx}, \mathbf{D}_{zx}, \mathbf{D}_{xy}, \mathbf{D}_{yy}, \mathbf{D}_{zy}, \mathbf{D}_{xz}, \mathbf{D}_{yz}, \mathbf{D}_{zz} \tag{B.2}$$

that is the cell center coordinates, norm of the divergence of the MDF term, the divergence of the MDF term and the MDF term itself (a tensor with 9 components)

B.2.6 Flowchart

The computation of a bubble involves the following steps:

1. A call to the subroutine `Init` in `AxiBubbleEngine` to initialize all data;
2. A call to the subroutine `Secant` in order to carry out one or steps of the secant procedure used in solving $F(X) = 0$;

3. Further calls to the subroutines that carry out postprocessing including:
    (a) `GenTriangles` to output a triangular discretization of the bubble surface;
    (b) `GenTetrahedra` to output a tetrahedral discretization of the bubble volume;
    (c) `PoissonPhi` to compute the potential and velocities on Cartesian grid surrounding the bubble using the fast Poisson solver technique.

B.3 Program installation

The AxiBubble program is distributed as a standard Windows installation package (available in the `Package`) subdirectory. The package is generated semi-automatically by the deployment tool within Visual Basic. Some required files are not recognized by the deployment tools and must be manually included in the distribution. These are:

- `MSSTDFMT.DLL` - a standard Windows file;
- `DFORRT.DLL` - Digital Visual Fortran Library;
- `MDFTerm.exe` - The MDFTerm post processing utility.

B.4 Ellipsoid of revolution test case

The practical order of convergence of the integral equation solver was determined by comparison to the known analytical solution for an ellipsoid of revolution (fig. 2.2). The parametric equations for an ellipsoid of revolution, expressed so that the radius of curvature at $\eta = 0$ is equal to 1, are

$$z = \alpha^2(1 - \cos\eta), \quad r = \alpha \sin\eta \tag{B.3}$$

with α the aspect ratio of the ellipsoid. The semi-axes are $(a, b) = (\alpha^2, \alpha)$ along (z, r). The analytic expression for the potential of the uniform motion with velocity U of the ellipsoid through a fluid is [31]

$$\phi = \frac{\alpha_0}{2 - \alpha_0} U z \tag{B.4}$$

with

$$\alpha_0 = ab^2 \int_0^\infty \frac{d\lambda}{(b^2 + \lambda)(a^2 + \lambda)^{3/2}} = \frac{2ab^2}{3} R_D(b^2, b^2, a^2) = \frac{2\alpha^4}{3} R_D(\alpha^2, \alpha^2, \alpha^4) \tag{B.5}$$

where R_D is Carlson's elliptic integral of the second kind

$$R_D(x, y, z) = \frac{3}{2} \int_0^\infty \frac{dt}{\sqrt{(t + x)(t + y)(t + z)^3}}, \tag{B.6}$$

a standard function of special mathematics libraries (e.g. IMSL).

Appendix C

Essential features of **OCTLES** data structures and procedures

C.1 Ancestor, parent and child volumes

In order to provide maximum flexibility in the ability to describe complicated geometrical domains OCTLES uses tetrahedral grids exclusively. The principal benefits of tetrahedral coverings are:

- ability to easily describe sharp variations in geometric surfaces;
- an extensive body of formulas is available to describe geometric quantities through the mathematical theory of simplexes;
- the possibility to efficiently subdivide and reassemble computational cells;
- the possibility to formulate simple relationships between an initial computational cell and the elements of its subdivision.

The key to computational efficiency in OCTLES is the procedure by which a single tetrahedron is subdivided into smaller elements. Consider an initial tetrahedron named a *parent volume*. A standard numbering procedure (fig. C.1) is adopted for nodes, edges and faces. The parent tetrahedron may be subdivided into smaller *child tetrahedra* in many ways. One possibility which allows significant benefits is to divide the tetrahedron into eight child volumes using the edge midpoints as exemplified in fig. C.2. A solid with eight faces remains at the center of the parent volume. This is subdivided into four tetrahedra which have one of the diagonals as a common edge. Four of the resulting child tetrahedra are similar to the initial tetrahedron and therefore named *like children*. The other four, resulting from the division of the central volume *456789* are called *unlike children*.

It is apparent that many similarities exist between the parent volume and the child volumes. These similarities may be intensively exploited by only storing geometric quantities associated with the parent volume and regenerating as needed the child geometric quantities. There is an execution time penalty for this but it is negligible since all arithmetic operations that arise are multiplications by a power of two.

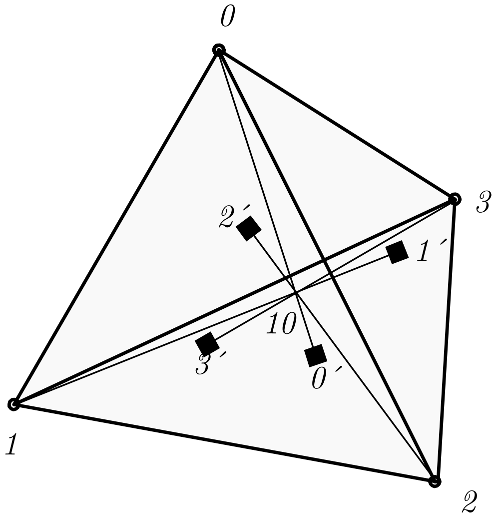

Figure C.1: Standard numbering conventions on a tetrahedron.

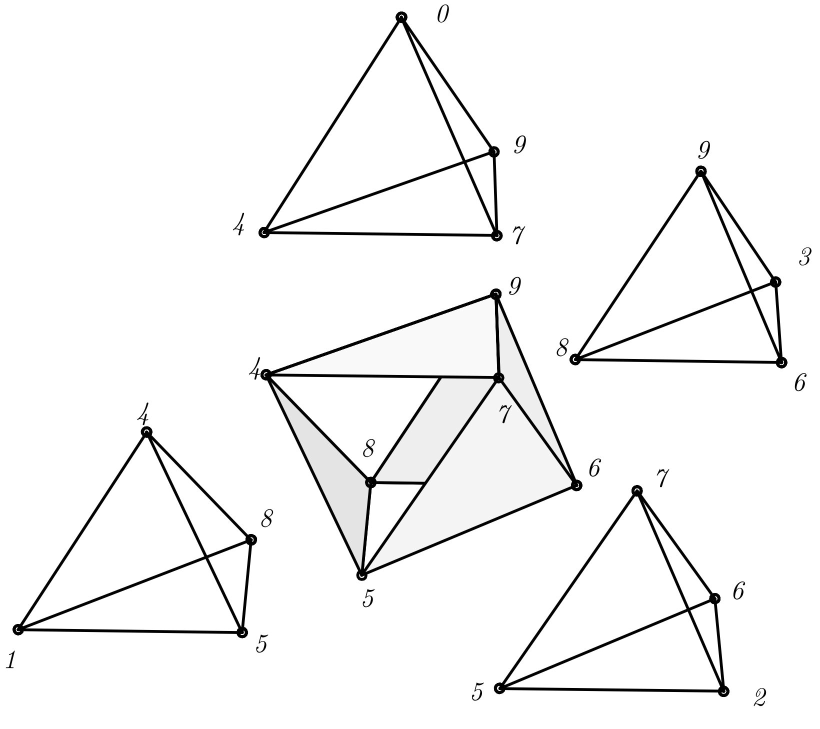

Figure C.2: Standard splitting of a parent tetrahedron into eight children.

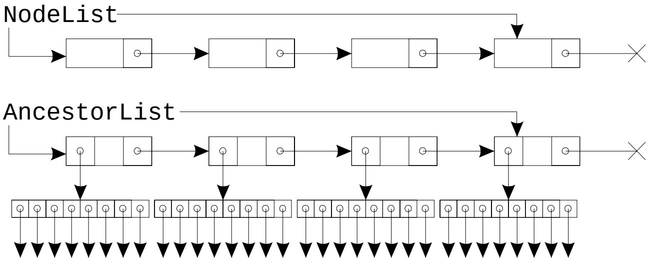

Figure C.3: The main data structures in OCTLES.

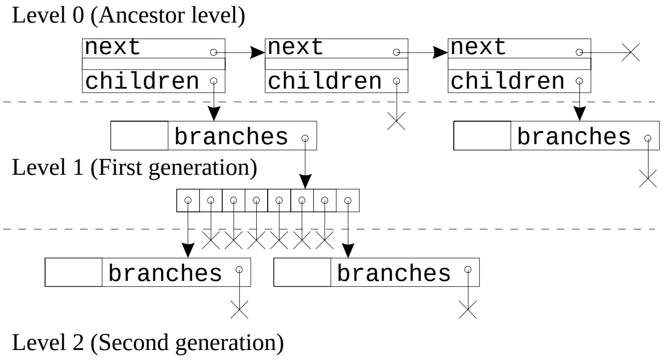

Figure C.4: Octal tree storage of parent and child tetrahedra.

Such operations may be implemented as bit shifts in the standard binary floating representations. The benefit obtained is enormous if the procedure is not applied only one time but repeatedly by subdividing the child volumes in the same manner until the required grid resolution is reached. This leads to the consideration of the initial volume as an *ancestor* for a tree of *descendents*. The initial discretization of the computational domain is kept intentionally coarse so as to have a small ($\sim 10^3$) number of ancestor volumes. The ancestor volumes and their nodes are stored in two global program lists (fig. C.3). Ancestor volumes are closely identifiable to subdomains upon which different simulation equations are solved.

C.2 Framework for actions upon the program data

The benefits of a the octal tree data structure are made available by a standard mechanism for applying transformations on the simulation data. It would of course be wasteful to include in the flux calculation procedures the details of obtaining geometric data from an ancestor volume or of maintaining adjacency relationships. All of these basic operations are taken care of by a general stack-based procedure. The desire is that at all times all data relating to the current computational cell are available on the top of the stack. A general procedure is available for reading

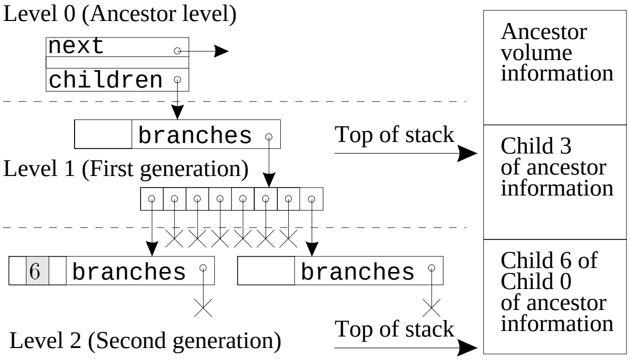

Figure C.5: State of the stack at a stage of the octal tree traversal procedure.

the top of stack data, called the *top stack frame* (fig. C.5). When adding a new flux calculation procedure to the program all data relating to a cell is ensured to be available to the procedure in a transparent manner. In writing a flux calculation procedure there is no need to be concerned about the mechanics of traversing the list of octal trees. A typical stack frame record is

```
 typedef struct {
  FieldVarPrec q[NrOfNodes][NrOfFieldVars];
  CoordPrec X[NrOfNodes][NrOfDims];
  AreaPrec S[NrOfFaces][NrOfDims];
  VolumePrec V;
  GenericNode* nodes[NrOfNodes];
  EdgeTypes edges;
  FaceParametrization* Face[NrOfFaces];
  GenericDescendents *parent;
  int branch;
} VolumeInformation;
```

This mechanism allows the independent addition of different flux calculation procedures. OCTLES acts on the program data through three basic mechanisms:

- `ApplyOnLeaves` - applies a user function on all nodes of the octal tree that have no further children, these are called *tree leaves*;
- `ApplyOnLevels` - applies a user function on all nodes of the octal tree that are at a certain distance from the top, root level or from the bottom, leaf level;
- `ApplyOnNodes` - applies a user function on all nodes of the octal tree;

All of these mechanisms traverse the tree and when the conditions for applying the user function are satisfied it is called. Data relating to computational cells is

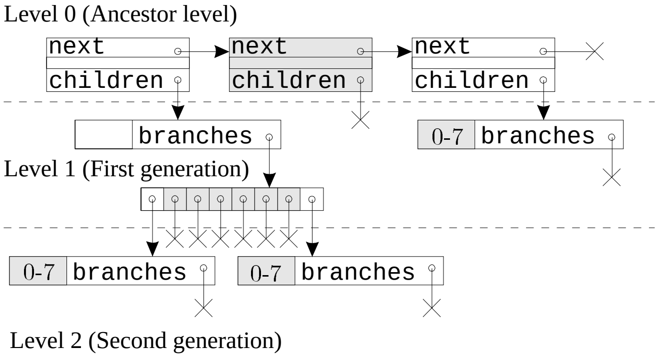

Figure C.6: Action of `ApplyOnLeaves`.

automatically updated on a stack associated with each octal tree. As the octal tree is traversed the conditions for invoking the user specified function are checked. When satisfied the function is invoked. The action of `ApplyOnLeaves` is exemplified in fig. C.6.

Bibliography

[1] N. Ashgriz and J. Poo. FLAIR: Flux line-segment model for advection and INterface reconstruction. *J. Comp. Phys.*, 93:449–468, 1991.

[2] C. Berbente, D. Cacuci, G. Grötzbach, S. Mitran, W. Sabisch, and M. Wörner. Contributions to a detailed local numerical simulation of turbulent bubbly flows. Technical Report FZKA 6356 (in preparation), IRS, Forschungszentrum Karlsruhe.

[3] C. Berbente and S. Mitran. unpublished report, 1997.

[4] M. Boivin, O. Simonin, and K. Squires. Direct numerical simulation of turbulence modulation by particles in isotropic turbulence. *J. Fluid Mech.*, 375:235–263, 1998.

[5] S. Chapman and T. Cowling. *The Mathematical Theory of Non-Uniform Gases.* Cambridge University Press, Cambridge, 1953.

[6] H. Deconinck, R. Struijs, H. Bourgois, H. Paillere, and P. Roe. Multidimensional upwind schemes for unstructured grids. In *Special Course on Unstructured Grid Methods for Advection Dominated Flows*, Neuilly sur Seine, France, 1992. AGARD R-787.

[7] R. Defay and I. Prigogine. *Surface Tension and Adsorption.* Longmans, London, 1966.

[8] P. Duineveld. The rise velocity and shape of bubbles in pure water at high reynolds number. *J. Fluid Mech.*, 292:325–332, 1995.

[9] P. Duineveld. Bouncing and coalescence of bubble pairs rising at high reynolds number in pure water or aqueous surfactant solutions. *Applied Scientific Research*, 58:409–439, 1998.

[10] A. Esmaeeli and G. Tryggvason. Direct numerical simulations of bubbly flows. part 1. low reynolds number arrays. *J. Fluid Mech.*, 377:313–345, 1998.

[11] M. Germano, U. Piomelli, P. Moin, and W. Cabot. A dynamic subgrid-scale eddy viscosity model. *Phys. Fluids*, A 3:1760, 1991.

[12] W. Hackbush. *Integral Equations – Theory and Numerical Treatment.* Birkhäuser, Basel, 1995.

[13] C. Hirsch. *Numerical Computation of Internal and External Flows.* John Wiley Sons, Chichester, 1990.

[14] C. W. Hirt and B. D. Nichols. Volume of fluid (VOF) method for the dynamics of free boundaries. *J. Comp. Phys.*, 39:201–255, 1981.

[15] T. Hughes, L. Franca, and G. Hulbert. A new finite element formulation for fluid dynamics: VIII. the galerkin/least-squares method for advective-diffusive equations. *Computer Methods in Applied Mechanics and Engineering*, 73:173–189, 1989.

[16] M. Ishii. *Thermo-Fluid Dynamics of Two-Phase Flow.* Eyrolles, Paris, 1975.

[17] J. Jimenez, A. Wray, P. Saffman, and R. Rogallo. The structure of intense vorticity in isotropic turbulence. *J. Fluid Mech.*, 255:65–90, 1993.

[18] O. Kellog. *Foundations of Potential Theory.* Springer-Verlag, Berlin, 1967.

[19] E. Kennard. *Kinetic Theory of Gases.* McGraw-Hill, New York, 1938.

[20] J. Kok. Dynamics of gas bubbles moving through liquid. part i. theory. *Eur. J. Mech. B Fluids*, 4:515, 1993.

[21] J. Kok. Dynamics of gas bubbles moving through liquid. part II. experiment. *Eur. J. Mech. B Fluids*, 12:541, 1993.

[22] H. Lamb. *Hydrodynamics.* Cambridge University Press, 1932.

[23] M. Lance and J. Bataille. Turbulence in the liquid phase of a uniform bubbly air-water flow. *J. Fluid Mech.*, 222:95–118, 1991.

[24] L. D. Landau and E. M. Lifschitz. *Statistical Physics.* Pergamon Press, Oxford, 1969.

[25] J. E. Lennard-Jones. *Proc. Roy. Soc.*, A106:441, 1924.

[26] A. Mayo. The fast solution of poisson's and the biharmonic equations on irregular regions. *SIAM J. Num Anal.*, 21:285–299, 1984.

[27] W. McComb. *The Physics of Fluid Turbulence.* Clarendon Press, Oxford, 1990.

[28] S. Mikhlin. *Linear Equations of Mathematical Physics.* Holt, Rinehart and Winston, Inc., New York, 1967.

[29] M. Miksis, J.-M. Vanden-Broeck, and J. Keller. Axisymmetric bubble or drop in an uniform flow. *J. Fluid Mech.*, 108:89–100, 1981.

[30] M. Miksis, J.-M. Vanden-Broeck, and J. Keller. Rising bubbles. *J. Fluid Mech.*, 123:31–41, 1982.

[31] L. Milne Thomson. *Theoretical Hydrodynamics.* McMillan, London, 1968.

[32] S. Mitran, D. Caraeni, and D. Livescu. Large eddy simulation of unsteady rotor-stator interaction in a centrifugal compressor. In *33rd AIAA/ASME/SAE/ASEE Joint Propulsion Conference and Exhibit*, New York, 1997. AIAA.

[33] D. Moore. The boundary layer on a spherical bubble. *J. Fluid Mech.*, 16:161–176, 1963.

[34] D. Moore. The velocity of rise of distorted gas bubbles in a liquid of small viscosity. *J. Fluid Mech.*, 23:749–766, 1965.

[35] Y. Nagano and Y. Itazu. Renormalization group theory for turbulence: Eddy-viscosity type model based on an iterative averagin method. *Phys. Fluids*, 9:143–153, 1997.

[36] J. Prausnitz. *Molecular Thermodynamics of Fluid-Phase Equilibria.* Prentice-Hall, Englewood Cliffs, 1969.

[37] R. Reid and T. Sherwood. *The Properties of Gases and Liquids.* McGraw-Hill, New York, 1958.

[38] P. L. Roe. Discrete models for the numerical analysis of time-dependent multidimensional gas dynamics. *J. Comp. Phys.*, 63:458–476, 1986.

[39] W. Sabisch. unpublished report, 1997.

[40] H. Schlichting. *Boundary-Layer Theory.* McGraw-Hill, New York, 1979.

[41] P. Smerka. On the motion of bubbles in a periodic box. *J. Fluid Mech.*, 254:79, 1993.

[42] B. Stewart and B. Wendroff. Two-phase flow: Models and methods. *J. Comp. Phys.*, 56:363–409, 1984.

[43] A. Van Bekkum. *Theoretical and Experimental Investigation of the Liquid Flow Around a Gas Bubble.* PhD thesis, Technische Hogeschool Delft, 1985.

[44] L. V. Wijngaarden. The mean rise velocity of pairwise-interacting bubbles in liquid. *J. Fluid Mech.*, 251:55–78, 1993.

[45] V. L. Wijngaarden. On pseudo turbulence. *Theoret. Comput. Fluid Dynamics*, 10:449–458, 1998.

[46] A. Wills. *Vector Analysis.* Prentice-Hall, New York, 1931.

[47] K. Wilson and J. Kogut. An early exposition of the renormalization group in quantitative form. *Phys. Rep.*, 12C:1, 1974.

[48] V. Yakot and S. Orszag. Renormalization group analysis of turbulence. i. basic theory. *J. Sci. Comput.*, 1:3, 1986.

[49] Y. Yurkovetsky and J. Brady. Statistical mechanics of bubbly liquids. *Phys. Fluids*, 8:881–895, 1996.

[50] Y. Zhou, W. McComd, and G. Vahala. Renormalization group in turbulence: Historical and comparative perspective. Technical Report TR-97-36, ICASE, 1997.